Fall 2012

2D IR done cheaper, easier, and faster: design and applications

William Thomas Rock
University of Iowa

Recommended Citation

Rock, William Thomas. "2D IR done cheaper, easier, and faster: design and applications." PhD (Doctor of Philosophy) thesis, University of Iowa, 2012.
http://ir.uiowa.edu/etd/3522.

2D IR DONE CHEAPER, EASIER, AND FASTER:

DESIGN AND APPLICATIONS

by

William Thomas Rock

An Abstract

Of a thesis submitted in partial fulfillment
of the requirements for the Doctor of
Philosophy degree in Chemistry
in the Graduate College of
The University of Iowa

December 2012

Thesis Supervisor: Associate Professor Christopher M. Cheatum

ABSTRACT

Two-Dimensional infrared (2D IR) spectroscopy measures correlations and couplings of vibrational transitions. All 2D IR spectrometers are home-built instruments that require extensive expertise to build and operate. Zanni and coworkers recently demonstrated that direct IR pulse shaping can simplify 2D IR data collection and analysis (S. H. Shim, R. Gupta, Y. L. Ling, D. B. Strasfeld, D. P. Raleigh and M. T. Zanni, Proc. Natl. Acad. Sci. U.S.A. **106** (16), 6614-6619 (2009)).

A pulse-shaping 2D IR spectrometer will produce less signal strength than a traditional four-wave mixing 2D IR spectrometer. Therefore, despite the advantages it offers, direct IR pulse shaping has not been widely adopted in the 2D IR community. This thesis outlines all the necessary steps to construct a pulse shaping 2D IR spectrometer. Then, it presents a novel detection scheme that utilizes a CMOS visible array. The CMOS array costs only 1500USD, while an MCT array, used in most 2D IR spectrometers, normally costs >50,000USD. After a thorough description of the apparatus, this thesis presents several 2D IR studies. The first study is a quantitative comparison of the signal strength of a pulse-shaping 2D IR spectrometer utilizing CMOS visible array detection to the signal strength of a traditional four-wave mixing 2D IR spectrometer. The second study measures 2D IR spectra of the azido stretch of ^{15}N-labeled 3-azidopyridine. The final study measures the cyanate (OCN^-) anion in several polar protic solvents.

The comparison shows that rapid averaging, made possible with direct IR pulse shaping, overcomes the loss of signal strength. It is also shown that upconversion and CMOS visible array detection does not cause a measurable loss in the signal to noise ratio (S/N). The study of ^{15}N-labeled 3-azidopyridine shows that the azido stretch is an effective indirect probe of the protonation state of the pyridine ring. The study of OCN^- reveals non-Gaussian spectral diffusion dynamics in methanol, presents a simple analysis of the non-Gaussian dynamics, and provides a physical justification of the observed dynamics.

Abstract Approved: ______________________________
Thesis Supervisor

____
Title and Department

____
Date

2D IR DONE CHEAPER, EASIER, AND FASTER:

DESIGN AND APPLICATIONS

by

William Thomas Rock

A thesis submitted in partial fulfillment
of the requirements for the Doctor of
Philosophy degree in Chemistry
in the Graduate College of
The University of Iowa

December 2012

Thesis Supervisor: Associate Professor Christopher M. Cheatum

Graduate College
The University of Iowa
Iowa City, Iowa

CERTIFICATE OF APPROVAL

PH.D. THESIS

This is to certify that the Ph. D. thesis of

William Thomas Rock

has been approved by the Examining Committee for the thesis requirement for the Doctor of Philosophy degree in Chemistry at the December 2012 graduation.

Thesis Committee: ___________________________
Christopher M. Cheatum, Thesis Supervisor

____
Claudio J. Margulis

____
Mark A. Arnold

____
Amanda J. Haes

____
Thomas F. Bogges

He who loves not wine, woman, and song, remains a fool his whole life long.

Martin Luther

TABLE OF CONTENTS

CHAPTER

APPENDIX

LIST OF TABLES

LIST OF FIGURES

CHAPTER 1

MOTIVATION AND OVERVIEW

Two-dimensional infrared (2D IR) spectroscopy provides a wealth of information on vibrational couplings,[1] spectral diffusion,[2] and chemical exchange.[3-5] 2D IR is often described as the optical analog of 2D NMR spectroscopy. 2D NMR measures the correlations and couplings of nuclear spins, while 2D IR measures the correlations and couplings of vibrational transitions. A distinct advantage of 2D IR over 2D NMR is that it can provide dynamical information on much faster timescales. 2D IR can probe molecular interactions on femtosecond (fs) to picosecond (ps) timescales. Many interesting chemical processes occur on these fast timescales, including solvent rearrangement, hydrogen-bond making and breaking, and fast chemical exchange. Unlike 2D NMR, though, 2D IR remains a very specialized technique. 2D IR spectrometers are not commercially available; they must be built and maintained by an optics professional. The requisite instrumentation is also exceedingly expensive. Therefore, reduction of the practical barriers to 2D IR data collection will expand the availability of this powerful technique to a greater portion of the scientific community.

Direct IR pulse shaping, first demonstrated by Zanni and coworkers,[6] greatly simplifies 2D IR data collection and analysis. Although it is difficult to assemble, a pulse shaping 2D IR spectrometer offers several distinct advantages after it is constructed. A traditional 2D IR spectrometer can take anywhere from minutes to hours to collect a 2D IR spectrum, while a pulse shaper takes less than a second. A pulse shaper automatically collects perfectly phased absorptive spectra, while traditional data collection methods require phase manipulation by hand. The perfectly phased spectra can also be automatically averaged.

Despite the copious benefits offered by pulse shaping, it has still not been widely adopted in the 2D IR community. Pulse shaping will result in a loss of signal strength, and many 2D IR spectroscopists are afraid this loss will render some experiments impossible. Here, we outline all the necessary steps to construct a pulse shaping 2D IR spectrometer, and present a quantitative comparison of its signal strength to a traditional four-wave mixing 2D IR spectrometer. Then, we present a novel detection scheme that utilizes a CMOS visible array. The CMOS array costs only 1500USD, while an MCT array, used in most 2D IR spectrometers, normally costs >50,000USD.

Finally, we use the pulse shaping 2D IR spectrometer with CMOS array detection to investigate several interesting chemical systems. The data in chapter 5 provides a promising foundation to the study of proton transfer kinetics in strongly hydrogen-bonded systems. Chapter 6 studies non-Gaussian dynamics observed in solutions of sodium cyanate in polar protic solvents; this demonstrates the ability of 2D IR to observe spectral diffusion, and distinguish Gaussian from non-Gaussian dynamics.

CHAPTER 2

EXPERIMENTAL METHODS AND THEORETICAL BACKGROUND

2.1 The Pump-Probe Analogy

A physical description of 2D IR greatly aids its interpretation. The common physical description of pump-probe spectra offers excellent insight; 2D IR is essentially pump-probe spectroscopy with frequency resolution of the excitation.[7] This section provides a physical description of the signals produced by a pump-probe spectrometer, and the following sections outline several experimental strategies to frequency resolve the excitation.

Pump-probe spectroscopy measures changes in the absorption of a probe beam induced by a pump beam, by measuring the probe beam absorption with and without excitation from a pump beam. Normally, a mechanical chopper blocks the pump beam on every other laser shot to measure spectra with and without the presence of the pump beam. Figure 2.1 illustrates the absorption changes induced by the pump beam.

Pump beam excitation causes three different types of signal. The first two signal types cause a decrease in the absorption of the probe beam, and result in a negative signal. These two signals appear at the energy difference between the ground vibrational state and the first excited state, or the ν=0 to 1 transition. The first type of signal is called ground-state bleach. The promotion of vibrations to the first excited state depopulates the ground state, so there are fewer molecules that absorb the probe beam, resulting in less absorption and a negative signal.

Figure 2.1: Pump-Probe Analogy

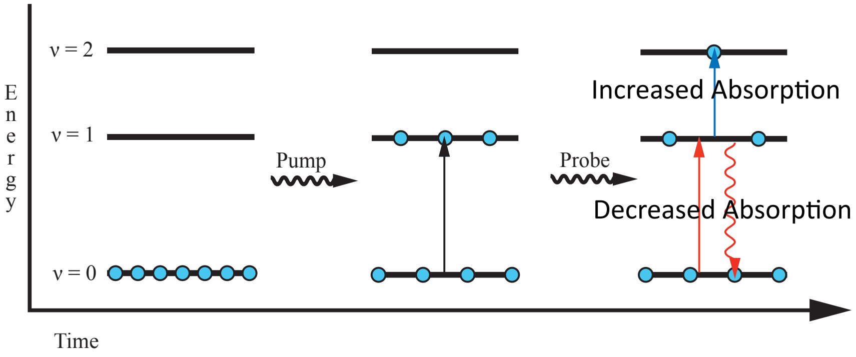

This is an illustration of the source of the signals observed in a pump-probe spectrum. The blue dots represent the vibrational state of the sample molecules. The pump interacts with the sample first and promotes some of the molecules to the first excited state. This causes a change in absorbance of the probe beam. The two red arrows represent ground-state bleach and stimulated emission signals. The blue arrow represents an excited state absorption.

The second type of signal is stimulated emission. The probe beam will cause some molecules, promoted to the first excited state by the pump beam, to radiatively decay back to the ground state. This also results in a decreased absorption and negative signal.

The final type of pump-probe signal is called excited-state absorption. Excited-state absorption appears at the energy difference between the first and second excited vibrational states, or the ν=1 to 2 transition. The pump beam populates the first excited state. Therefore, molecules in the first excited state can absorb, which causes the probe beam to experience an increased absorption at the energy difference between the ν=1 and 2 states.

The molecules excited by the pump beam relax as the time delay between the pump and probe beams increases. Scanning the pump-probe delay measures the rate that the molecules relax out of the first excited state, as seen by a decay in the ν=1 to 2 transition: if there are no molecules in the first excited state, there will be no excited state absorption. Molecules do not necessarily return immediately to the ground state as they relax out of the first excited state. Therefore, the ground-state bleach signal often persists longer than the excited state absorption signal. A 2D IR spectrum is a snapshot of the pump and probe frequencies at a particular pump-probe delay. A series of 2D IR spectra at increasing pump-probe delays reveals a wealth of kinetic and dynamic information; extraction of this information will be addressed in a later section.

The pump-probe spectrum is the 2D IR spectrum integrated over ω_1. Figure 2.2(a) shows a slice of the 2D IR spectrum at a fixed value of ω_1. Although an ω_3 slice is not strictly a pump-probe spectrum, the signal trace looks exactly like pump-probe trace. Figure 2.2(b) shows a 2D IR spectrum. The x-axis, called ω_1, is the pump axis, and the y-axis, called ω_3, is the probe axis. The negative signal is due to ground state bleaching and stimulated emission (the red peak in the 2D IR spectrum), and the positive signal is due to excited state absorption (the blue peak in the 2D IR spectrum). Anharmonic scaling of the vibrational energy levels causes the ν=1 to 2 transition to appear at a lower energy than the ν=0 to 1 transition. A large anharmonicity results in a large spacing between the ν=0 to 1 and ν=1 to 2 vibrational transitions.

Figure 2.2: 2D IR Spectrum and ω_3 Slice

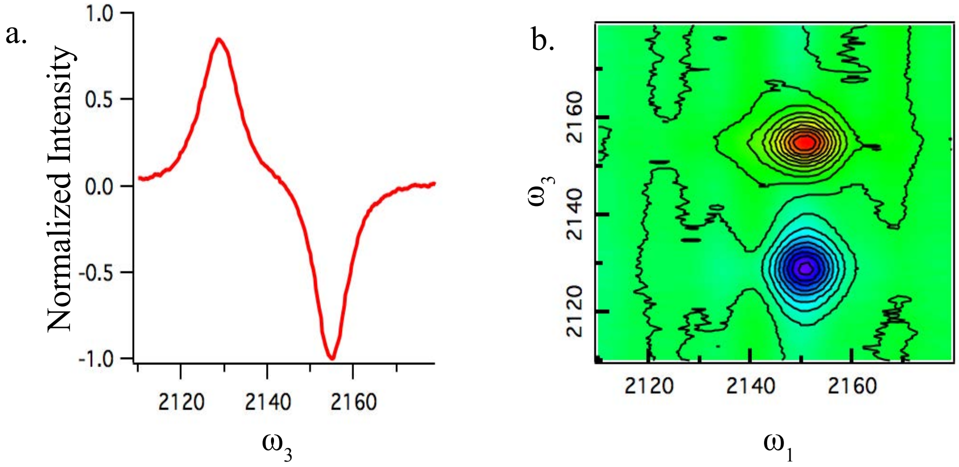

An ω_3 slice of the 2D IR spectrum (a) at ω_1=~2151 cm^{-1} closely resembles a pump-probe trace. A 2D IR spectrum is pictured in (b). The ω_1 axis is the absorption of the pump beam, and the ω_3 axis is the change in absorption of the probe beam. The red peak is the ν=0 to 1 transition, and the blue peak is the ν=1 to 2 transition.

2.2 The First 2D IR Spectrometer: The Hole Burning Apparatus

The first 2D IR spectrum was taken by a broadband pump-probe spectrometer with a Fabry-Perot etalon in the pump beam to select the pump wavelength.[8] A broadband pump-probe spectrometer uses IR laser pulses ~100 fs in duration with a spectral full width at half maximum (FWHM) bandwidth of ~150 cm^{-1}. The production of mid-IR radiation with those specifications is routine, and will be briefly described later. The etalon narrows the bandwidth of the pump beam, and tunes the center frequency of the narrow band pump.

The pump excites a narrow band of frequencies, then the probe beam passes through the sample, and a spectrometer measures the change in absorbance for the entire probe spectrum. When the pump frequency is resonant with the $\nu=0$ to 1 transition, stimulated emission, ground state bleach, and excited state absorption signals will appear in the probe beam. Therefore, signals will appear at the $\nu=0$ to 1 transition on the pump axis, and both the $\nu=0$ to 1 and $\nu=1$ to 2 transitions in the probe axis. This narrow band pump, broadband probe 2D IR technique is commonly called hole-burning 2D IR spectroscopy. Figure 2.3 shows a cartoon of the optical layout of a hole-burning 2D IR spectrometer, and highlights the narrow frequency regions excited by the pump. The blue arrow in figure 2.3 points to the narrow band pump frequency that will excite the $\nu=0$ to 1 transition.

Hole-burning 2D IR spectroscopy is experimentally simple, but it has several important drawbacks. The Fourier-transform relationship between time and frequency dictates that a narrow frequency bandwidth results in a long pulse in the time domain. The time-bandwidth product defines the shortest pulse that can be achieved with a given spectral bandwidth. Although it is usually reported as a unitless product, it is helpful to know that a 150 cm^{-1} bandwidth corresponds to a minimum pulse duration of 100 fs given a Gaussian lineshape:

$$\Delta\nu\Delta t \geq (150cm^{-1})(100fs)$$

A pulse is said to be transform limited when the above equation is an equality. Therefore, a 5 cm^{-1} Gaussian pump pulse will be 3000 fs long. An increase in frequency resolution results in a decrease in time resolution. An etalon makes this problem even worse, because it produces an exponential pulse shape that causes the pulses to overlap in time even longer than if they were Gaussian. Therefore, femtosecond dynamics cannot be measured with hole-burning 2D IR spectroscopy.

Figure 2.3: The Hole Burning Apparatus

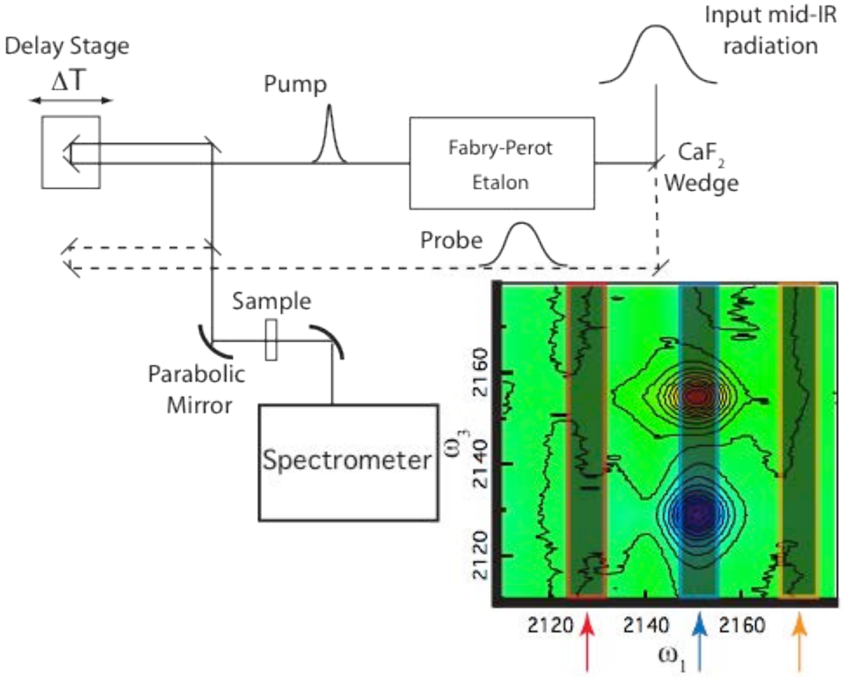

Optical layout of a hole-burning 2D IR spectrometer:
The highlighted areas in the spectrum represent the pump excitation frequencies. Hole-burning 2D IR spectroscopy maps out a 2D IR spectrum by collecting a broadband probe spectrum for each narrow band pump excitation. The pump beam bandwidth sets the ω_1 frequency resolution, and the maximum time resolution.

The etalon also throws away most of the pump bandwidth, so much of the pump pulse energy is lost, which weakens the observed signal. Shortly after the advent of hole-burning 2D IR spectroscopy, vibrational spectroscopists took advantage of Fourier-transform techniques to measure 2D IR spectra with molecule-limited time and frequency resolution. The next section is a brief summary of the Fourier-transform properties that were exploited in the experimental design of more complicated 2D IR spectrometers.

2.3 Fourier Space Exploitation

The relationship between time and frequency is mathematically expressed by a Fourier-transform. The Fourier transformation of a function in the time domain to the frequency domain is given by:

$$FT(f(t)) \equiv \frac{1}{\sqrt{2\pi}} \int_{-\infty}^{\infty} f(t) e^{i\omega t} dt = f(\omega)$$

The above equation converts a function in the time domain, $f(t)$, to a function in the frequency domain, $f(\omega)$. Both versions of the equation contain the same information, but viewing data in one domain or the other can make it easier to glean physical insight.

The cosine function is a simple starting place to describe the relationship between the time domain and the frequency domain. Consider a cosine function in the time domain, given by the equation $\cos(\omega_0 t)$. This function is a periodic oscillation that continues forever in time with a frequency of ω_0. The cosine wave oscillates at a single frequency, so logically the frequency domain representation is a singularly valued function. The function that describes this scenario is a delta function at ω_0, $\delta(\omega+\omega_0)$. However, it should be noted that a cosine function does not define the sign of the oscillation: $\cos(\omega_0 t)=\cos(-\omega_0 t)$. Consider a wheel spinning at a constant rate. A cosine function can aptly describe the rate the wheel is spinning, but not the direction. The same cosine wave describes a clockwise or a counterclockwise spin. Therefore, the Fourier transform of a cosine wave in the time domain is two delta functions, one at positive frequency, and one at negative frequency. The Fourier transform of a cosine wave with a high frequency is two pulses in the frequency domain that are far apart, and the Fourier transform of a cosine wave with a low frequency is two pulses that are close together, as shown below:

Figure 2.4: Time and Frequency Domain Sine Wave

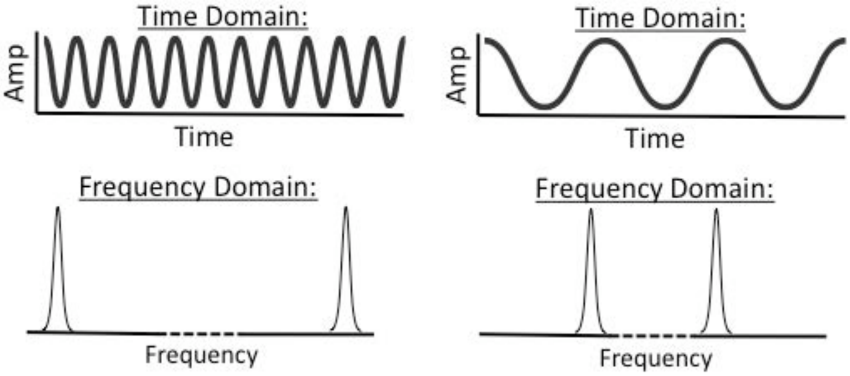

Cartoon of the Fourier transform of a low frequency and a high frequency cosine function.

Another important property of Fourier transforms is the inverse relationship between the time domain and the frequency domain. The Fourier transform of a cosine wave in the time domain is two pulses in the frequency domain; therefore, the Fourier transform of a cosine wave in the frequency domain is two pulses in the time domain, so the inverse of figure 2.4 is valid:

Figure 2.5: Frequency and Time Domain Sine Wave

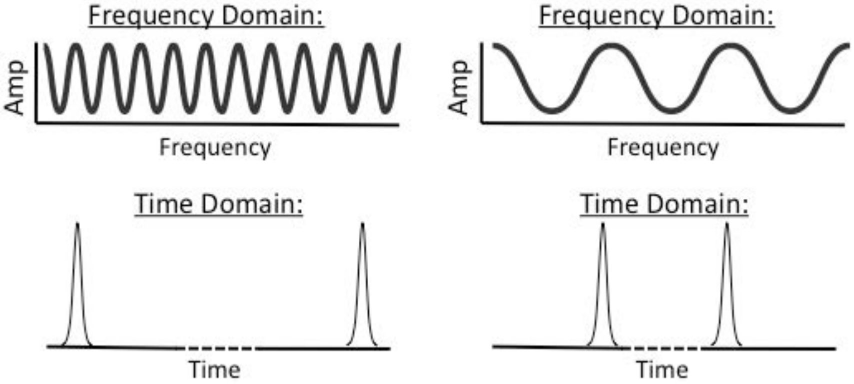

The Fourier transform of a cosine function in the time domain or the frequency domain is always two pulses. The separation of the two pulses is dictated by the period of the oscillation.

A Fourier-transform is a linear transformation, so the information content in the time or frequency domain is the same. The hole-burning experiment collects the pump axis by scanning the pump beam in the frequency domain. The etalon selects a narrow frequency band, and scans the central frequency of the narrow band across the entire range of interest. Scanning the delay between two pulses in the time domain will create an interferogram. The interferogram will oscillate in the time domain at the characteristic frequencies of the system. Fourier transformation will convert the time domain oscillations into the frequency spectrum of the system. Spectroscopists have long exploited this property of Fourier transforms in optical designs, and soon after the demonstration of the hole-burning experiment, Fourier transform techniques were applied to 2D IR spectroscopy.[9, 10]

Two different time domain 2D IR spectrometers have been constructed in our laboratory: A four-wave mixing (FWM) spectrometer, and a pulse-shaping spectrometer. The simplest way to scan two pulses in the time domain is to divide a pulse with beam splitters, and control the distance each beam travels with delay stages to create a time delay. This strategy is employed in the FWM apparatus, which has been the most popular time domain 2D IR data collection method for the last ten years. A pulse shaper can also scan the time delay between two pulses. Zanni and coworkers recently developed direct IR pulse shaping for 2D IR spectroscopy, a technological advancement that offers several important advantages that will be addressed in detail later[6, 11]. The next sections outline the experimental design of the FWM apparatus and the pulse shaping apparatus.

2.4 Time Domain 2D IR Data Collection in a Boxcar Geometry

Time domain 2D IR spectroscopy requires independent control of three excitation pulses. The first two pulses are the pump pulse, and scanning the time delay between them measures the pump axis of a 2D IR spectrum in the time domain, like scanning the etalon measures the pump axis in the frequency domain. However, independent control of the three excitation pulses offers the opportunity to employ several optical tricks to greatly increase the signal strength of a 2D IR spectrometer.

A major drawback of a pump-probe spectrometer is that it measures a small signal on a large background. As previously stated, a pump-probe spectrometer measures the change in intensity of the probe beam due to excitation from the pump beam. The three light-matter interactions in the sample cause a third-order polarization in the sample molecules. This third order polarization results in the emission of an electric field on top of the probe beam. The electric field constructively and destructively interferes with the probe beam, causing the observed intensity changes. The strength of the emitted electric field is proportional to the product of the three excitation fields. A detector measures the probe beam intensity, so the probe beam must not saturate the detector. Therefore, the probe beam cannot be as intense as the pump beams, which weakens the emitted signal.

The vectors of the three excitation pulses dictate the vector of the emitted electric field. Therefore, a clever beam geometry results in the isolation of the desired third-order signal in a unique direction. Separation of the signal from the excitation pulses allows the use of three equally intense excitation pulses. The so-called boxcar beam geometry is used in the four-wave mixing (FWM) apparatus. Figure 2.6 shows the excitation beam geometry and the direction of the emitted electric field in the pump-probe geometry, and the boxcar geometry.

Previous sections describe 2D IR with the pump-probe picture. A different physical picture often describes time-domain 2D IR data collection; note that both pictures describe the same phenomena. In the time domain picture, the first pulse coherently excites the ensemble of molecules to a coherent superposition state. All the excited molecules experience slightly different chemical environments; therefore, they will have slightly different excitation frequencies. By definition, a coherent superposition state is oscillatory, and all the molecules in superposition state will oscillate at the frequency corresponding to the energy difference between the states in the superposition. All the frequencies in the broadband laser pulse are in phase; therefore all the molecular vibrations excited by the laser pulse will initially be in phase. The distribution of frequencies will cause the molecules to dephase.

Figure 2.6: Pump-probe and Boxcar Beam Geometries

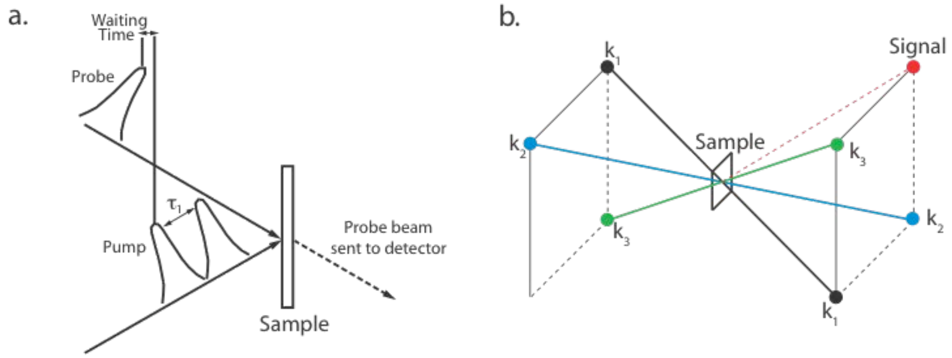

Pump-probe beam geometry (a), and boxcar beam geometry (b). The boxcar geometry collects the signal in the $-k_1+k_2+k_3$ phase matching direction.

The time delay between the first and second pulses is called τ_1, or the evolution time, because the oscillations evolve in this time period. The second pulse stops the coherence, and creates a population in the $\nu=1$ state. The time delay between the second and third pulses, T, is called the population time, because the molecules are in a population during this time. The final pulse creates another coherence. The oscillation of the second coherent superposition state causes emission of the third order signal. The time after the third pulse, τ_3, is called the detection time, because the signal is emitted. Figure 2.7 shows the pulse sequence and the three time periods of time-domain 2D IR.

Figure 2.7: 2D IR Pulse Sequence

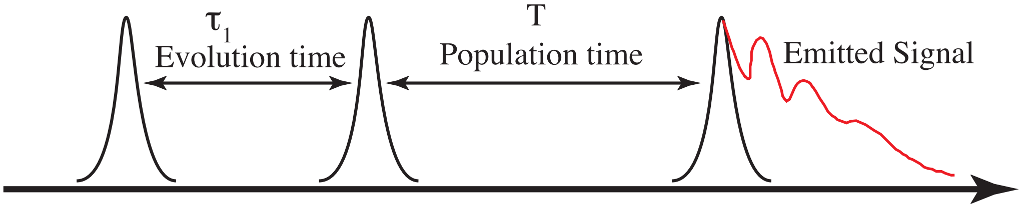

The three excitation pulses in a time-domain 2D IR experiment: The first two pulses are the pump pulses, and the third pulse is the probe pulse. The third order signal is emitted after the third pulse.

There are several other important differences between the boxcar geometry and the pump-probe geometry. In the boxcar geometry, the rephasing and nonrephasing signals are emitted in different directions. Rephasing signals arise from signal pathways with opposite phase during the two coherence times, and nonrephasing signals arise from signal pathways with the same phase during the two coherence times. The sum of the rephasing and nonrephasing signals produces the absorptive 2D IR spectrum. Rephasing signals emit in the $-k_1+k_2+k_3$ phase matching direction. Nonrephasing signals emit in the $+k_1-k_2+k_3$ phase matching direction. In the pump-probe geometry, k_1 and k_2 are the same vector, so rephasing and nonrephasing spectra emit collinearly. In the boxcar geometry, the time ordering of the first two pulses selects whether rephasing or nonrephasing signals emit in the fourth corner of the boxcar geometry. The emitted signal is called the vibrational echo response.

In the pump-probe geometry, the vibrational echo response emits on top of the probe beam, and the resultant interference is detected. A spectrometer converts the probe beam to the frequency domain for detection. Detection of the interference of the emitted field and another electric field is called heterodyne detection; detection of only the vibrational echo response is called homodyne detection. The field that overlaps the vibrational echo for heterodyne detection is called the local oscillator. The interference between the vibrational echo response and the local oscillator allows a square-law detector to measure both the amplitude and phase of a vibrational echo response; homodyne detection only measures the amplitude of the echo.

In the pump-probe geometry, the probe beam is the third excitation pulse and the local oscillator, so the pump-probe geometry is often called self-heterodyned. Excitation in a boxcar geometry emits the vibrational echo in a unique direction, so another IR pulse must overlap with the echo for heterodyne detection. In the FWM apparatus, a beamsplitter picks off a small portion of the third electric field to become the local oscillator. A fourth delay stage controls the time delay between the local oscillator and the vibrational echo.

Control of the delay between the local oscillator and the echo allows the FWM apparatus to collect the probe axis in the time domain. This is called time-time data collection. Collection of the pump axis in the time domain, and the probe axis in the frequency domain is called time-frequency data collection. In time-time data collection, delay stages scan the τ_1 time delay to measure the pump axis, and the delay between the echo and local oscillator to measure the probe axis. A Fourier-transform along each axis produces a 2D IR spectrum from the measured signal. The pump-probe geometry must collect data time-frequency, because it cannot scan the delay between the echo and local oscillator. Time-frequency data collection is normally employed in the FWM apparatus as well, because a multichannel array detector can collect the entire probe spectrum in the frequency domain in a single laser shot, and greatly reduce measurement time. Multichannel array detection is addressed further in another section.

2.5 Optical Design of Our Four-wave Mixing Apparatus

The FWM apparatus in our laboratory collects the heterodyned vibrational echo response as a function of one frequency and two time variables. Focusing three IR pulses in the sample produces the vibrational echo response. The vibrational echo response is overlapped with a fourth electric field, the local oscillator, for heterodyne detection.

A monochromator disperses the overlapped echo and local oscillator to measure the frequency variable, ω_3. The monochromator scans ω_3 while a delay stage steps τ at a fixed value of T. The interference between the echo and the local oscillator produces an interferogram for each frequency value in ω_3. A Fourier transform of the τ axis converts it to the frequency domain, and provides the second frequency axis in the 2D IR spectrum.

ZnSe beamsplitters divide the mid-IR radiation to create the three pulses that generate the echo response. Mechanical stages fitted with retroreflectors scan τ and T. A 3° CaF_2 wedge sends a small portion of the third beam to a fourth delay stage to become the local oscillator. Square gold-coated mirrors form the three pulses into a boxcar geometry after the delay stages. A 90° off-axis parabolic mirror (100 mm focal length) focuses the three beams in the sample, and a second parabolic mirror collimates the light after the sample. An iris isolates the third order response in the $-k_1+k_2+k_3$ phase matching direction after the second parabolic mirror. A 2 inch 3° CaF_2 wedge combines the signal and the local oscillator after the sample. A lens focuses the signal and local oscillator through the entrance slit on a commercial spectrometer. The monochromator steers the output through the exit slit to a single channel HgCdTe (MCT) detector. The τ axis is scanned with 19 fs steps from 0 to 3500 fs to collect the rephasing spectrum, and from -3500fs to 0 fs to collect the nonrephasing spectrum. The monochromator scans the ω_3 axis from 2180 cm^{-1} to 2100 cm^{-1} with 2 cm^{-1} steps. The sum of the rephasing and nonrephasing spectra produces an absorptive 2D IR spectrum. MCT array detectors are commonly used in FWM apparatuses to eliminate the need to step scan the monochromator, and increase the speed of data collection. Unfortunately, the high cost of an MCT array prevented its addition the FWM apparatus.

A mechanical chopper blocks every other laser shot in one of the input beams. A lock-in amplifier (Stanford Research Systems) locks into the 500 Hz chopper signal, and digitizes the detector output. The difference of chopped and unchopped signal eliminates signals that do not depend on all three electric fields. The lock-in time constant is set to 10 ms, so the signal is the average of ~5 laser shots, because the chopped shots do not produce signal. Figure 2.8 is a drawing of the optical layout of the FWM apparatus.

Figure 2.8: Four-wave Mixing Optical Setup

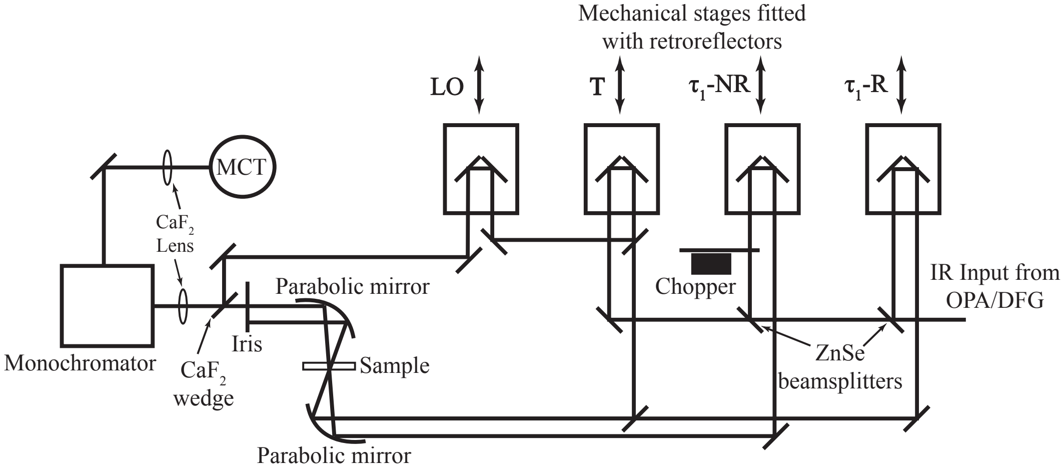

Optical layout of the four-wave mixing apparatus. 2D IR spectra are collected time-frequency. A monochromator scans the ω_3 axis. The monochromator output is measured with a single channel MCT detector.

2.6 Pulse-shaping Introduction

Time-domain 2D IR spectroscopy requires control of a sequence of mid-IR laser pulses. The four-wave mixing apparatus uses beamsplitters and delay stages to create and control mid-IR pulse sequences. Optical pulse shaping can also produce the necessary pulse sequences. Pulse shaping devices offer sophisticated control of the amplitude and phase of the input laser pulse, which has been demonstrated extensively in visible spectroscopy.[12-16] Warren and coworkers first demonstrated optical pulse shaping with an acoustic optic modulator (AOM) for visible spectroscopy.[16] Zanni and coworkers extended the techniques developed by Warren to the IR for 2D IR spectroscopy.[6, 17, 18] The pulse-shaping apparatus is a recent development in our laboratory, and the following sections outline the theoretical and practical aspects of direct IR pulse shaping.

Most optical pulse shaping devices apply a linear filter to the input laser pulse that produces the desired pulse shape. Linear filtering is commonly used in electrical engineering to produce arbitrary electronic waveforms, and can be described in the time or frequency domain. However, most optical pulse shapers modulate the input pulse in the frequency domain.

The output of a linear frequency filter, $E_{out}(\omega)$, is the product of the input electric field $E_{in}(\omega)$ and the frequency mask applied by the filter $M(\omega)$.

$$E_{out}(\omega) = E_{in}(\omega)M(\omega)$$

The mask can modulate the phase and amplitude of the input electric field, so it is common to report the mask in the following functional form:

$$M(\omega) = A(\omega)e^{i\phi(\omega)}$$

where $A(\omega)$ is the spectral amplitude, and $\phi(\omega)$ is the spectral phase.

2.7 Two Pulse Generation Via Frequency Domain Pulse Shaping

Recall that the Fourier transform of a cosine wave is two pulses, and the frequency of the cosine wave dictates the separation of the two pulses. This Fourier-transform relationship implies that scanning slices in the frequency domain or delays in the time domain can collect the same information. The four-wave mixing apparatus uses beam splitters to shape the IR laser pulse in the time domain. The Fourier transform of the pulse pair created by the beam splitters is a cosine wave in the frequency domain. Therefore, shaping the IR pulse spectrum into a cosine wave will create two pulses in the time domain.

A cosine wave frequency mask can be written in terms of complex exponentials, where the frequency of the cosine wave is given by τ, and the phase is given by ϕ.

$$M(\omega) = \cos\left(\tau\omega + \phi\right) = \frac{1}{2}\left(e^{i(\omega\tau+\phi)} + e^{-i(\omega\tau+\phi)}\right)$$

Recall the Fourier transform of a cosine wave is symmetric about zero. Therefore, it is clear to see the Fourier transform of the first exponential in the above equation is a delta function at $t=\tau$, and the Fourier transform of the second exponential is a delta function at $t=-\tau$. The desired mask produces pulses at $t=0$ and $t=\tau$, and offers independent control of the phase of both of the pulses. Therefore, the desired mask has the following functional form:

$$M(\omega) = \frac{1}{2}\left(e^{i\phi_1} + e^{i\tau\omega}e^{i\phi_2}\right)$$

where ϕ_1 is the phase of the pulse at $t=0$, and ϕ_2 is the phase of the pulse at $t=\tau$. The above equation can be rearranged in terms of an amplitude and phase mask.

$$M(\omega) = \cos\left(\frac{\omega\tau-\phi_1+\phi_2}{2}\right)e^{i\left(\frac{\omega\tau+\phi_1+\phi_2}{2}\right)}$$

Therefore, a frequency mask with amplitude

$$A(\omega) = \cos\left(\frac{\omega\tau-\phi_1+\phi_2}{2}\right)$$

and phase

$$\phi(\omega) = \frac{\omega\tau + \phi_1 + \phi_2}{2}$$

produces a pulse pair with one pulse at $t=0$ with phase ϕ_1, and a second pulse at $t=\tau$ with phase ϕ_2.[19]

2.8 Pulse Shaper Optical Design

Manipulation of the frequency spectrum can arbitrarily shape the time domain representation of a laser pulse; frequency domain pulse shaping requires control of the relative intensity of the frequencies in the pulse spectrum. A zero-dispersion stretcher provides a means of spatially separating the spectral components of a laser pulse, so a frequency mask can manipulate them.

A convex lens pair and a grating pair construct a simple zero-dispersion stretcher. The convex lenses have the same focal length (f), and are separated by a distance of $2f$. This arrangement is called a unit magnification telescope. The first lens focuses the input beam, and after the beam passes through a focus, the second lens collimates it; the net effect is an identical input and output. A grating is placed at the outer focal plane of each lens. The beam travels a total distance of $4f$ in the zero dispersion stretcher, so the arrangement is called a 4-f geometry.[12, 20] Figure 2.9 shows a cartoon of a zero dispersion stretcher.

A diffraction grating manipulates light much like a prism; it causes an angular dispersion in the frequencies of the pulse spectrum. The first lens has a dual effect. It collimates the angular dispersion caused by the grating, and focuses the individual spectral components. The focus of the first lens is called the Fourier plane; this point provides the maximum spatial resolution of the spectral components.

Figure 2.9: Zero Dispersion Stretcher

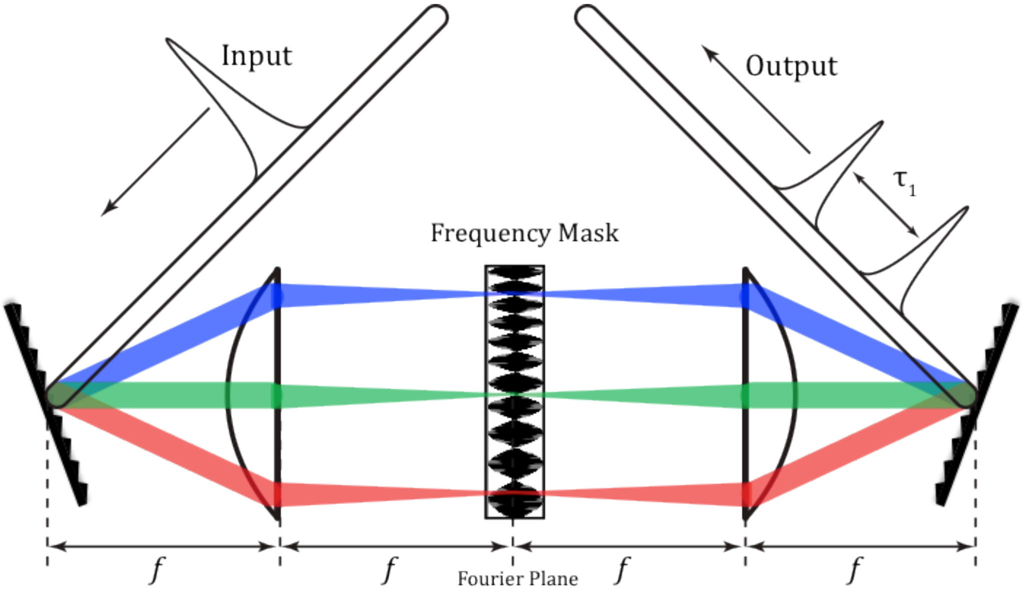

Optical layout of a zero dispersion stretcher. The first grating/lens pair spatially resolves the pulse spectrum at the Fourier plane. The frequency mask shapes the pulse spectrum at the Fourier plane. The second grating lens pair spatially recombines the shaped spectrum.

In effect, the first grating/lens pair performs a spatial Fourier transform on the input laser pulse. The second grating/lens pair is a mirror image of the first pair, and inverse Fourier transforms the input pulse. Without a frequency mask, the input and output of a zero dispersion stretcher are identical.

2.9 Frequency Mask Application: The Ge AOM

The zero dispersion stretcher spatially resolves the pulse spectrum, and a Ge acoustic optic modulator (AOM) provides a means to apply a frequency mask to the pulse spectrum. As mentioned previously, there are many other pulse shaping devices available for visible spectroscopy. However, to the best of our knowledge, the Ge AOM is the only device shown to effectively apply an amplitude and phase frequency mask directly to a mid-IR pulse spectrum.

The Ge AOM (Isomet – LS600-1109-W) is a programmable transmission grating.[16, 21] An arbitrary waveform generator (AWG) produces a 75 MHz radio frequency (RF) waveform with an arbitrary amplitude and phase. An RF splitter divides the output of the AWG (GaGe – CG4302). A two-sided radio frequency amplifier (RFA) amplifies the splitter output. The RFA (Isomet – 1160/4-ZP-PO) output drives a piezoelectric transducer attached to the Ge crystal in the AOM. The piezoelectric transducer transfers the RF waveform to the Ge crystal as an acoustic wave. The acoustic wave changes the index of refraction in the Ge crystal. The 75 MHz carrier frequency creates a periodic change in the refractive index of the Ge crystal. The periodic change in the refractive index creates a spatial transmission grating that scatters IR light in the same manner that an atomic lattice scatters x-rays in x-ray diffraction. An atomic lattice scatters x-ray radiation because the atomic spacing is on the order of the wavelength of light. This phenomenon is called Bragg scattering. The AOM scatters mid-IR radiation because the periodicity of the acoustic wave is on the order of the wavelength of mid-IR radiation. The Bragg scattering angle is given by:

$$n\lambda = 2d \sin\theta$$

where n is the diffracted order, λ is the wavelength of light, *d* is the groove spacing, and θ is the Bragg angle. The AOM uses the first order diffraction, so *n*=1. The acoustic velocity in Ge is 5.5 mm/μs, so the period of a 75 MHz acoustic wave in Ge is *d*= 73 μm. Therefore, the Bragg angle for 5 μm light is ~2°. Figure 2.10 is a cartoon of Bragg diffraction at an AOM.

Figure 2.10: Bragg Diffraction at AOM

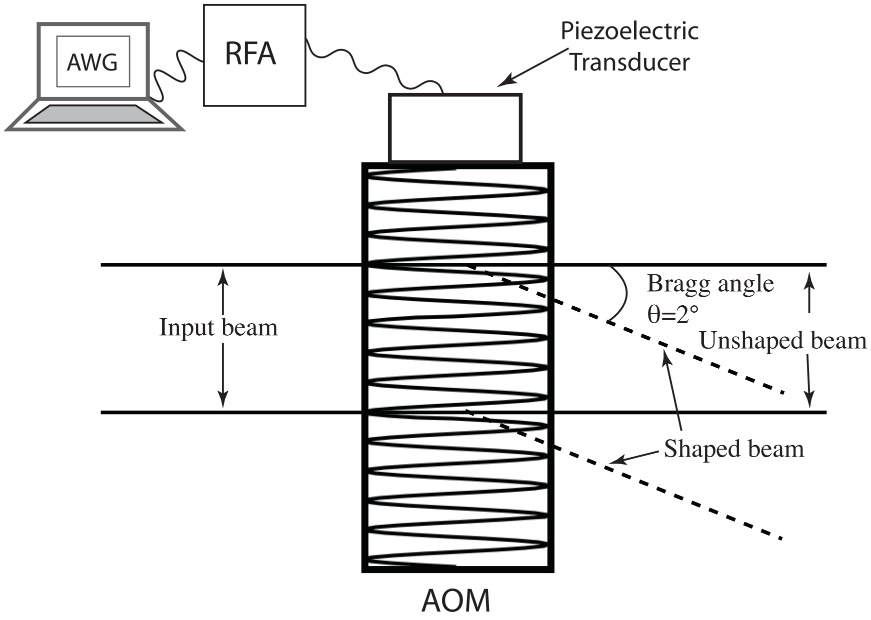

Diffraction at the Bragg angle separates the shaped and unshaped beams.

The amplitude and phase of the acoustic wave controls the amplitude and phase of the diffracted light. Therefore, a 75 MHz sine wave with the amplitude and phase of a double pulse spectrum creates the desired frequency mask.

$$M(\omega) = A(\omega)\sin\left(2\pi ft + \phi(\omega)\right)$$

where *f*=75 MHz is the carrier frequency, and *t*=3.3 ns is the time spacing of the carrier frequency.

The AWG uses a 300 MHz clock to digitize a 12 bit waveform; therefore, the AWG produces a waveform with 4096 discrete voltage levels. A value of 4095 corresponds to negative full scale, 2048 = 0 volts, and 0 corresponds to positive full scale. Therefore, the following function creates a pulse pair mask using the AWG

$$AWG = 2048(1 - A \times M(\omega))$$

where A is an amplitude factor that scales from 0 to 1 and controls the RF driving power.

It is important that the strength of the RF driving the piezoelectric transducer is appropriately scaled. The deflection efficiency goes through a maximum, then becomes nonlinear as the amplitude of the driving RF wave increases. The amplitude factor A adjusts the RF amplitude to ensure the deflection efficiency scales linearly with the RF amplitude.[19]

2.10 Zero Dispersion Stretcher Alignment

The zero dispersion stretcher diagramed previously provides a simple picture of a 4-*f* geometry, and has been employed in several pulse shaping spectrometers.[20, 22, 23] However, the use of lenses has several drawbacks. First, passing through a lens causes spectral dispersion; also, the effective focal length of a lens is frequency dependent. Replacing the lenses with cylindrical mirrors eliminates these effects. The optical setup employed in our lab is identical to the arrangement used by Zanni for 2D IR spectroscopy. Figure 2.11 is a diagram of the zero dispersion stretcher used in our laboratory.

Figure 2.11: Pulse Shaper Optical Setup

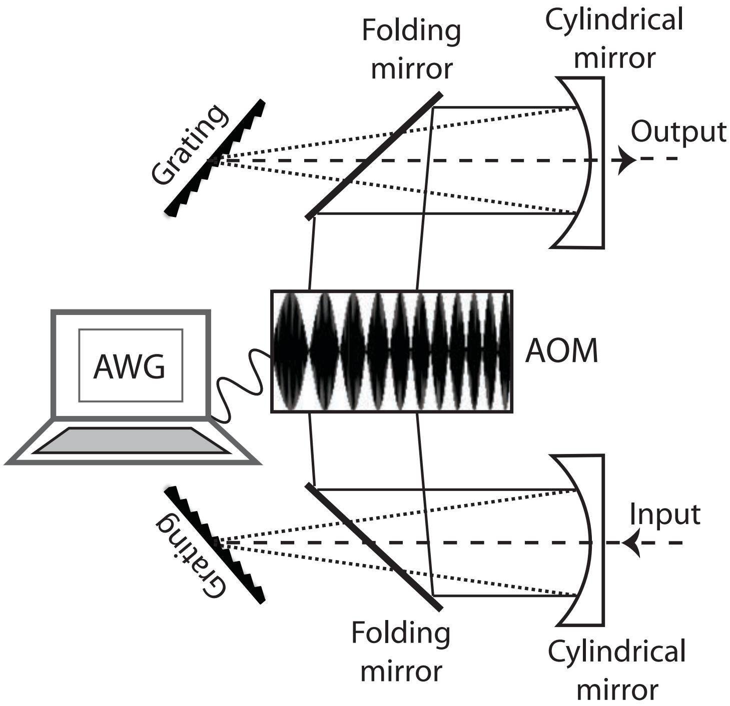

Pulse shaping apparatus. The distance between the gratings and the cylindrical mirrors is *f*, and the distance between the two cylindrical mirrors is 2*f*. The AOM is placed at the Fourier plane. This 4*f* geometry uses all reflective optics.

The zero dispersion stretcher in figure 2.11 uses all reflective optics. The optical setup has two reflectance gratings (Richardson Gratings, 300 g/mm, 26.7°

nominal blaze angle), two gold coated cylindrical mirrors (efl=125mm), and two gold coated folding mirrors. Both gratings are aligned in a quasi-Littrow configuration. The Littrow configuration is a grating angle for which the diffracted beam is reflected back on top of the incident beam. The Littrow angle is given by:

$$m\lambda = 2d\sin(\theta)$$

where m is the diffracted order, λ is the wavelength of light, d is the distance between grooves in the diffraction grating, and θ is the Littrow angle. The Littrow configuration usually gives the highest deflection efficiency; manufacturer provided efficiency curves are normally reported for the grating in the Littrow configuration. The gratings are in a quasi-Littrow configuration because the first order diffraction is vertically displaced from the incident beam.

The input light passes over the top of the cylindrical mirror and folding mirror and diffracts off the grating. The first order diffraction is sent back along the incident path with a downward vertical displacement. The cylindrical mirror reflects the diffracted light back toward the grating, below the incident beam. Then the folding mirror turns the diffracted light 90°. The second folding mirror, cylindrical mirror, and grating are a mirror image of the first. Both gratings and both cylindrical mirrors are mounted on translation stages so the distances in the 4-*f* geometry can be easily optimized. Without the AOM, the input and output beams are identical. The Fourier plane is found between the two folding mirrors; the Ge AOM is placed at the Fourier plane.

The initial alignment of the zero dispersion stretcher was done with a red diode laser. The 300 g/mm diffraction gratings are designed to disperse infrared light; the grating disperses the nearly monochromatic red light into a series of diffracted orders. The diffracted orders are the brightest when the grating is rotated to the blaze angle, 26.7°. The first step is to properly align the diffraction grating.

The diffraction grating is mounted on a translation stage. Several custom pieces assemble two mirror mounts and a rotation stage on top of the translation stage to properly align the grating. Drawings of these pieces can be found in the appendix. The face of the grating is centered on the axis of rotation of the rotation stage. One mirror mount holds the grating and adjusts the face angle. This mount is designed to hold a 1” optic. A 1” circular metal piece fits in the mount and attaches to another custom metal mount that holds the grating. This allows the face of the grating to be spun in the mount. The grooves are not always perfectly perpendicular to the bottom of the substrate, and a diffraction grating will disperse light perpendicular to the grooves. Therefore, the face of the grating is spun to ensure there is no tilt in the diffracted light relative to the other optics in the zero dispersion stretcher.

The other mirror mount holds the rotation stage; adjustment of this mirror tilts the axis of rotation. A vertical displacement separates the input and output beams in the zero dispersion stretcher. The mirror mount tilts the axis of rotation to provide this displacement. It is important to tilt the axis of rotation and not the face of the grating. If there is a vertical tilt in the face of the grating relative to the axis of rotation, the grating will exhibit conical diffraction. The grating is spun in its mount to eliminate angular tilt in the diffraction, and the vertical face angle is adjusted to eliminate conical diffraction. The grating is aligned by sending the diffraction of the red diode laser back on top of the incident beam, and observing the behavior of the diffracted orders as the diffraction angle is rotated. Figure 2.12 shows the effects of grating misalignment observed by the diode laser.

Figure 2.12: Grating Alignment

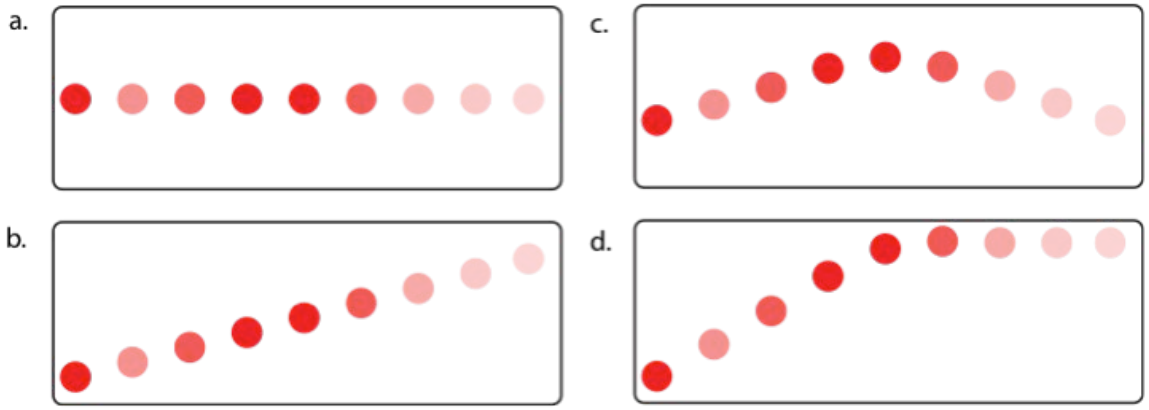

The observed red diode laser diffraction spots as the grating angle is rotated for: (a) proper grating alignment (b) grooves not parallel to the axis of rotation – fixed by spinning the face of the grating in the mount (c) vertical face angle of the grating is different than the axis of rotation – fixed by adjusting the vertical pointing on the grating mount (d) a combination of (b) and (c).

After both gratings are aligned, the other optics can be placed. The gratings are set at their blaze angle to make use of the brightest spots. The axis of rotation of the grating is tilted down. The first cylindrical mirror and folding mirror are crudely placed in approximate alignment, and the light reflected off the folding mirror is propagated down the table. The distance between the grating and the curved mirror is adjusted until the angular dispersion of the grating is collimated, then the vertical and horizontal alignment of the cylindrical mirror and folding mirror are carefully optimized. The grating angle is rotated to ensure there is flat spatial dispersion at the Fourier plane. Small adjustments of the horizontal tilt of the axis of rotation can fix a small tilt. A large tilt in the spatial dispersion requires realignment of the grating.

Next, the second folding mirror and cylindrical mirror are placed. The distance between the two curved mirrors is set so the diffracted spots are collimated. A temporary mirror placed just before the grating sends a bright order down the table to ensure it is collimated. Finally, the tilt and translation of the second grating is adjusted to provide a collimated output parallel to the table. Interference fringes appear when the second grating recombines two of the diffracted orders. The optimized alignment has the greatest fringe spacing.

After the zero dispersion stretcher is aligned with the red light, the gratings are rotated to the Littrow angle for the mid-IR. The output is sent to an interferometric autocorrelator (IAC) with a $AgGaS_2$ doubling crystal. The IAC measures the pulse duration of the output to ensure it is the same as the probe beam.

Finally, the AOM is placed at the Fourier plane. The horizontal angles of the folding mirrors and the angle of the AOM to maximize the light diffracted off the AOM. Maximum deflection occurs when the incident beam is at the Bragg angle. The AOM is electronically chopped during alignment to help distinguish the shaped beam from the unshaped beam. The chopped signal produced by the purely shaped and purely unshaped beams appear the same on the oscilloscope, except they are out of phase. Power cycling the RFA determines which phase is shaped, and which phase is unshaped.[19]

The pulse shaper alignment is very stable. After the initial alignment, only the grating angles need adjustment as the center frequency of the pulse spectrum changes. If you encounter an unexpected problem, DO NOT REALIGN THE ZERO DISPERSION STRETCHER!! It is never the problem. Something else is wrong. Trust me.

2.11 Phase Control

The phase of an oscillation refers to the fraction of the oscillation that has elapsed relative to an arbitrary reference point. Phase is most often reported in radians or degrees, and one complete oscillation is 2π radians, or 360°. Two identical oscillations with a π phase shift are said to be out of phase, or 180° out of phase. Figure 2.13 shows two oscillations with a π phase shift to illustrate the sign change. Phase manipulation is a powerful asset when measuring light waves.

The pulse shaper provides a means to arbitrarily shape the pump pulse phase. The frequency mask derived in section 2.7 creates a pulse pair separated in time by τ, with phases ϕ_1 and ϕ_2, respectively. The phase of the signal depends of the phase of the excitation pulses, and any functional form can be given to ϕ_1 and ϕ_2. The advantages of phase control were first developed for NMR spectroscopy, where arbitrarily shaped RF waveforms have been available for years. These techniques have been extended to visible and IR spectroscopies through optical pulse shaping.[13, 24-27]

Figure 2.13: π Phase Shift

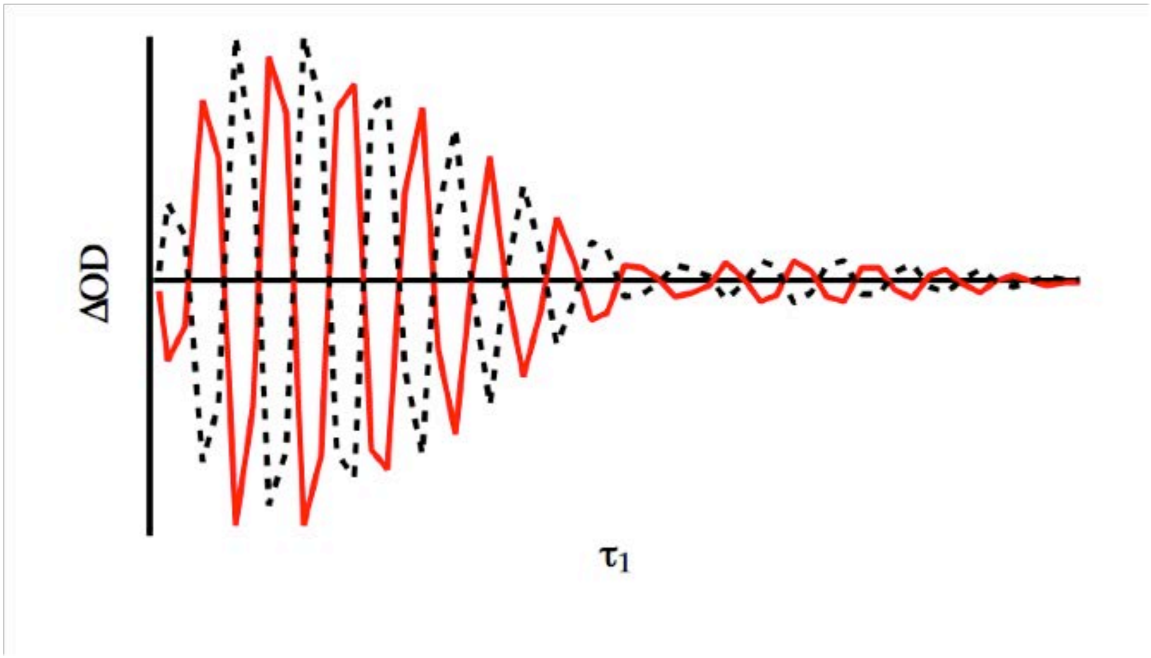

This is a slice along the pump axis of a 2D IR spectrum. The two traces are the same signal slice with a π phase shift.

It is fairly straightforward to demonstrate the phase dependence of the measured signal on the phases of the excitation pulses and local oscillator. Recall that 2D IR is a third-order nonlinear spectroscopy, and three light-matter interactions lead to the emission of 2D IR signal. The third order signal is given by:

$$E_{2DIR}^{(3)} \propto \int_0^\infty dt_3 \int_0^\infty dT \int_0^\infty d\tau E_3(t-t_3)E_2(t-t_3-T)E_1(t-t_3-T-\tau)R^{(3)}(t_3,T,\tau)$$

where E_1, E_2, and E_3 are the electric fields of the three excitation pulses, τ is the evolution time, T is the waiting time, t_3 is the detection time, and $R^{(3)}$ is the molecular third order response function.

The electric field of the laser pulses is given by:

$$E(t) = E^{'}(t)e^{-i(\omega t+\phi+\vec{k}\cdot\vec{r})} + c.c.$$

The phase of the electric field is not time dependent, so the phase terms in the three electric field interactions can be moved outside the integral. The pump probe geometry defines the k vectors of the three electric fields; E_{2DIR} will emit in the $\pm k_1 \mp k_2 + k_3$ phase matching direction. Therefore, the phase dependence of the signal is given by:

$$E_{2DIR}^{(3)} \propto e^{i(\pm\phi_1 \mp\phi_2+\phi_3)}$$

Also recall that 2D IR is a heterodyne detected measurement, so the measured signal is the interference between the local oscillator and the third order signal emitted from the sample.

Therefore, the measured signal is given by:

$$S = \left| E_{LO} + E_{2DIR}^{(3)} \right|^2 .$$

Finally, the overall phase dependence of the measured signal is given by:

$$\phi_{sig} = \pm\phi_1 \mp \phi_2 + \phi_3 - \phi_{LO}.$$

The sign of the phase is different for rephasing and nonrephasing signal pathways. The rephasing and nonrephasing phases are given by:

$$\phi_{reph} = -\phi_1 + \phi_2 + \phi_3 \text{ and } \phi_{nonreph} = +\phi_1 - \phi_2 + \phi_3$$

The rephasing and nonrephasing spectra emit collinearly, and with opposite phase, which properly sums them to produce a purely absorptive 2D IR spectrum.

The pulse shaper affords control of the phase of the two pump pulses, but not the probe beam. Phase is always a relative measure, and the probe phase is always constant, so for simplicity it is defined as zero. A pump probe measurement is self-heterodyned, so the phase of the third excitation and the local oscillator are the same, therefore $\phi_3 = \phi_{LO} = 0$. Finally, it can be seen that the signal phase depends on the phase difference of the two pump interactions, so $\phi_{reph} = -\phi_1 + \phi_2$ and $\phi_{nonreph} = \phi_1 - \phi_2$. The rephasing and nonrephasing signals sum to produce the absorptive 2D IR signal. Therefore, the phase of the 2D IR signal depends on the phase difference of the pump pulses:

$$\phi_{2DIR} = \phi_1 - \phi_2 = \Delta\phi_{12}.$$

Therefore, changing the phase difference of the two pump pulses changes the sign of the measured 2D IR signal. The pulse shaper can change $\Delta\phi_{12}$ on every laser shot.

In a standard time domain pump probe experiment, a mechanical chopper blocks one of the pump pulses on every other laser shot, and a detector measures the probe beam with the pump and without the pump. Unfortunately, the desired 2D IR signal is only measured on half the laser shots; this can be avoided with phase cycling.

First, consider the simplest phase cycling technique. The first laser shot collects the probe spectrum with pump beam phases $\phi_1 = 0$ and $\phi_2 = 0$, so $\Delta\phi_{12} =$

0, and the second laser shot collects the probe spectrum with $\phi_1 = 0$ and $\phi_2 = \pi$, so $\Delta\phi_{12} = \pi$, which changes the sign of the 2D IR signal. The difference of the two spectra adds the desired 2D IR signal, and subtracts the background.

Consider the possible background signals. First, the phase of the probe spectrum is unaltered, so clearly it cancels. The other background signals that emit in the direction of the probe beam occur when either pump beam interacts twice with the sample; these are the so-called transient absorption signals. If one of the pump beams has zero phase shift, and interacts twice with the sample, the emitted signal will have zero phase shift. If one of the pump beams has a π phase shift, and interacts twice with the sample, the emitted signal will have a 2π phase shift. The two signals will be in phase; therefore, the transient absorption signals also do not depend on $\Delta\phi_{12}$, so they also cancel. This simple phase cycle collects signal on every laser shot, effectively doubling the 2D IR signal. Note, a chopper will only eliminate the transient absorption signal from the unchopped beam. The transient absorption signal that comes from the chopped beam will remain.

The pulse shaping scheme outlined above eliminates all phase matched third-order signals. However, light that scatters into the direction of the probe beam will also provide an unwanted background. Scatter suppression improves everyday data collection by reducing interference terms that arise because of a scratch or a fingerprint on a sample window. It also enables data collection on highly scattering samples where the scattering background can dwarf the signal, such as amyloid fibrils or mineral dust aerosols.

Recall, three electric field interactions generate 2D IR signal, which is overlapped with a local oscillator for heterodyne detection. In principle, a 2D IR experiment involves five electric fields: the three excitation fields E_1, E_2, and E_3, the local oscillator, E_{LO}, and the emitted 2D IR signal, E_{2DIR}. First, we will enumerate all the possible scattering pathways, and then focus on the pathways that cause distortion in our experimental setup. Given five electric fields, there will be ten possible interference pairs.

If light scatters into the sample direction from any one of the excitation pulses, it will interfere with the local oscillator at the detector. These three scattering pathways are defined as E_1E_{LO}, E_2E_{LO}, and E_3E_{LO}. One of the interferences from E_1E_{LO} and E_2E_{LO} will oscillate as τ is scanned, depending on which pulse is scanned and which pulse is stationary. After Fourier transformation along τ, signal from the oscillating scattering pathway will produce the pulse spectrum along the diagonal. Interference from E_3E_{LO} does not oscillate as τ is scanned; therefore, after Fourier transformation along τ, it will appear at zero frequency, and does not complicate the spectrum.

Scatter from pairs of excitation pulses can also interfere on the detector and produce unwanted background signal. These scattering pathways are defined as E_1E_2, E_1E_3, and E_2E_3. These pathways arise from two scattered beams; therefore, they will be much smaller than E_1E_{LO}, E_2E_{LO}, and E_3E_{LO}.

The desired signal is the interference between the emitted 2D IR signal and the local oscillator, $E_{2DIR}E_{LO}$. Scatter from the three excitation pulses can also interfere with E_{2DIR}. The signal and the local oscillator propagate in the same direction, and the local oscillator is much more intense than the signal, so again, these interferences will be much smaller than E_1E_{LO}, E_2E_{LO}, and E_3E_{LO}; nonetheless, they are present.

A four-wave mixing spectrometer collects 2D IR spectra in a boxcar geometry. In the boxcar geometry, the three excitation pulses interact with the sample with different *k*-vectors, and the 2D IR signal emits a unique direction. Therefore, all the interference terms can scatter into the direction of the signal, and must be accounted for. Hamm and coworkers present a discussion of scatter suppression in the boxcar geometry.[28] In the pump-probe geometry, the third excitation pulse is also the local oscillator, so $E_{probe}=E_3=E_{LO}$, and the first two excitation pulses come from the pump beam, and interact with the sample with the same *k*-vector. Therefore, in the pump-probe geometry, a discussion of the scattering pathways can be simplified to pump-pump scattering (the E_1E_2 interference term), pump-probe scattering (the $E_1E_3=E_1E_{LO}$, and $E_2E_3=E_2E_{LO}$ scattering terms), and pump-2DIR scattering (E_1E_{2DIR} and E_2E_{2DIR}). Recall that $E_{LO}E_{2DIR}$ is the desired signal, and in the pump-probe geometry $E_3E_{2DIR}=E_{LO}E_{2DIR}$, so it is not an unwanted scattering term. Also, since the third electric field and the local oscillator are the same beam, it is not relevant to discuss interference from the E_3E_{LO} term. Table 2.1 summarizes all the scattering pathways that are present in a time domain pump probe spectrometer. The remainder of this section will only discuss the presence of the five scattering pathways: E_1E_2, E_1E_3, E_2E_3, E_1E_{2DIR}, and E_2E_{2DIR}, and the signal pathway: $E_{LO}E_{2DIR}$, because all other terms are either irrelevant, or equivalent to one of the listed pathways.

In a standard time-domain 2D IR experiment in the pump-probe geometry, one of the pump beams is chopped. All pathways that are present after the difference are present in the measured spectrum. Note that the transient absorption pathway $E_2E_2E_3$ is also present. The signal collected with a chopper contains several scattering pathways, and a transient absorption signal.

The simple phase cycling scheme outlined above eliminates both transient absorption signals, more of the scattering pathways, and doubles the 2D IR signal compared a chopped signal. In this phase cycling scheme, all signals with $\Delta\phi = \pi$ in pulse two will add when the difference of the two pulses is taken.

Table 2.1: Relevant Scattering Pathways in Pump-probe Geometry

Pump-pump scattering pathways	E_1E_2
Pump-probe scattering pathways	$E_1E_3=E_1E_{LO}$, $E_2E_3=E_2E_{LO}$
Pump-2DIR scattering pathways	E_1E_{2DIR}, E_2E_{2DIR}
Irrelevant interference terms	$E_{LO}E_{2DIR}=E_3E_{2DIR}$=signal! E_3E_{LO}=The same beam

The ten possible scattering terms reduce to five relevant scattering pathways in the pump-probe geometry.

The two pulse phase cycle is an improvement over chopping, however, more of the scattering pathways can be eliminated using a four pulse phase cycle. Table 2.4 summarizes the four pulse phase cycle. The first two pulses are added, and the second two pulses are subtracted. Table 2.5 lists the sign of every signal pathway in the four pulse phase cycle, after accounting for the phase of the pathway, and whether it is added or subtracted during data analysis. Finally, the last column in table 2.5 give the result of the four pulse phase cycle.

Table 2.2: Interference Pathways with Chopper

	E_1	E_2	E_3	E_{2DIR}
Pulse 1: Chopper open	On	On	On	On
Pulse 2: Chopper closed	On	Off	On	Off
Signals Chopper open		$\mathbf{E_{LO}E_{2DIR}}$, E_1E_2, E_1E_3, E_2E_3, E_1E_{2DIR}, E_2E_{2DIR}		
Signals Chopper closed		E_1E_3		
Difference of Pulse 1 and Pulse 2		$\mathbf{E_{LO}E_{2DIR}}$, E_1E_2, E_2E_3, E_1E_{2DIR}, E_2E_{2DIR}		

The top two rows indicate what electric fields are present when the chopper is open and when the chopper is closed. The bottom three rows list the two pulse interference pathways present when the chopper is open, when the chopper is closed, and the difference between the two. The pathway $\mathbf{E_{LO}E_{2DIR}}$ is in bold because it is the desired signal.

Table 2.3: Two-Pulse Phase Cycle Interference Pathways

	ϕ_1	ϕ_2	ϕ_{2DIR}
Pulse 1	0	0	0
Pulse 2	0	π	π
Signals with $\Delta\phi = \pi$ in pulse 2	$\mathbf{E_{LO}E_{2DIR}}$, E_1E_2, E_2E_3, E_1E_{2DIR}		

The top two columns show the relative phase of the two pump pulses and the emitted 2D IR signal in a two pulse phase cycle. The third row lists all the pathways that add when the difference of the two pulses is taken.

As shown in table 2.5, the result of the four pulse phase cycle is $4E_{LO}E_{2DIR}$ + $4E_1E_2$. In a pump probe geometry, the probe beam is the third interaction and the local oscillator, so the relative phase of the third electric field and the local oscillator cannot be changed. Therefore, the remaining term will always have the same phase as the signal in this geometry, and cannot be eliminated by cycling the phase of the pump interactions. A combination of the four pulse phase cycle and chopping can eliminate the all scattering terms.[29]

Table 2.4: Four Pulse Phase Cycle Interference Pathways

	ϕ_1	ϕ_2	ϕ_{2DIR}	Sign	$\Delta\phi = 0$	$\Delta\phi = \pi$
Pulse 1	0	0	0	+	**$E_{LO}E_{2DIR}$**, E_1E_2, E_1E_3, E_2E_3, E_1E_{2DIR}, E_2E_{2DIR},	None
Pulse 2	π	π	0	+	**$E_{LO}E_{2DIR}$**, E_1E_2	E_1E_3, E_2E_3, E_1E_{2DIR}, E_2E_{2DIR}
Pulse 3	π	0	π	–	E_2E_{LO}, E_2E_3, E_1E_{2DIR}	**$E_{LO}E_{2DIR}$**, E_1E_2, E_1E_3, E_2E_{2DIR}
Pulse 4	0	π	π	–	E_1E_{LO}, E_1E_3, E_2E_{2DIR}	**$E_{LO}E_{2DIR}$**, E_1E_2, E_2E_3, E_1E_{2DIR}

The first three columns show the phase of the two pump pulses, and the resultant phase of the 2D IR signal in the four pulse phase cycle. The fourth column indicates if the measured signal is added or subtracted during data collection. The final two columns show the $\Delta\phi$ of all possible two pulse interferences.

Table 2.5: Sum of Interference Pathways in Four Pulse Phase Cycle

	Sign of all two pulse interferences
Pulse 1	**$E_{LO}E_{2DIR}$** $+ E_1E_2 + E_1E_3 + E_2E_3 + E_1E_{2DIR} + E_2E_{2DIR}$
Pulse 2	**$E_{LO}E_{2DIR}$** $+ E_1E_2 - E_1E_3 - E_2E_3 - E_1E_{2DIR} - E_2E_{2DIR}$
Pulse 3	**$E_{LO}E_{2DIR}$** $+ E_1E_2 + E_1E_3 - E_2E_3 - E_1E_{2DIR} + E_2E_{2DIR}$
Pulse 4	**$E_{LO}E_{2DIR}$** $+ E_1E_2 - E_1E_3 + E_2E_3 + E_1E_{2DIR} - E_2E_{2DIR}$
Total	4 **$E_{LO}E_{2DIR}$** $+ 4\, E_1E_2$

This table lists the sign of all possible two pulse interferences in each of the four pulses of a four pulse phase cycle. The bottom row gives the sum of the measured signal.

In the final data collection scheme, every pulse in the four pulse phase cycle is sent to the AOM twice, and a chopper blocks the probe beam on every other laser shot. Therefore, each time step requires 8 laser shots. When the probe beam is blocked, the only term that remains is the E_1E_2 scattering term. The difference of the first two pulses produces signals identical to the first pulse in the four pulse phase cycle, minus the E_1E_2 scattering term. The difference of pulses 3 and 4 reproduces the second pulse in the four pulse phase cycle minus the E_1E_2 scattering term, and so on. This data collection scheme eliminates all scattering terms.

2.12 The Shift Frequency

In time domain 2D IR, discrete time steps sample the IR oscillation of interest. According to the sampling theorem, an oscillatory signal can be perfectly reconstructed if the sampling step size is less half the period of the oscillation; this is called the Nyquist sampling rate. Therefore, fully sampling a 2000 cm^{-1} (16.67 fs period) oscillation requires a step size smaller than 8.3 fs. Satisfying the Nyquist criterion often requires the measurement of many data points, and can lead to extremely long data collection times. If the sampling step size is larger than the Nyquist rate, the measured frequencies overlap, a process called aliasing. However, if the sampling rate is known, the overlapped frequencies can be unwrapped to recover the actual frequencies.

Sampling with a larger step size than half the oscillation period is called undersampling. Undersampling is often employed in time-domain 2D IR to reduce measurement times. The Nyquist sampling rate determines the maximum bandwidth that can be unwrapped. When the measured frequencies overlap, the Nyquist sampling rate determines the bandwidth of frequencies in each fold. For example, an 8.3 fs step size will unambiguously measure all frequencies from 0 to 2000 cm^{-1}, and frequencies greater than 2000 cm^{-1} will overlap and complicate the spectrum. The usable bandwidth of a 100 fs pulse is around 300 cm^{-1}, depending on the molar absorptivity of the sample. The period of a 300 cm^{-1} oscillation is 111.11 fs, so a 55.55 fs step size can sample a bandwidth window of 300 cm^{-1}.

Undersampling can greatly reduce the measurement time, but at the sacrifice of signal strength. The amplitude of undersampled signal is smaller than fully sampled signal, because a large step size misses the peaks of the oscillation. Phase control of the time steps that sample the signal can shift the observed frequency. Red-shifting the observed frequency allows a larger step size to fulfill the Nyquist sampling criterion.

Incrementing the phase of the pump pulses proportional to the time delay will shift the observed frequency. This technique is called time proportional phase increments (TPPI); it has long been a standard technique in NMR spectroscopy. Zanni and coworkers recently implemented TPPI in 2D IR.[19, 27] If the phase difference between the two excitation pulses, $\Delta\phi_{12}$, is zero, then the signal will oscillate along τ at the vibrational frequency of the sample, ω_o. Recall the two pulse phase mask:

$$M(\omega) = \frac{1}{2}\left(e^{i\phi_1} + e^{i\tau\omega}e^{i\phi_2}\right)$$

If the second pulse is convoluted with an additional phase term, $e^{-i\omega_s\tau}$, the phase of the second pulse will be $e^{i(\omega_o-\omega_s)\tau}$, and the signal will oscillate at $\omega_o - \omega_s$, where ω_s is the shift frequency. In practice, the shift frequency becomes DC after Fourier transformation, and the Nyquist rate still determines the maximum bandwidth that can be sampled. If a 2D IR spectrum is collected with an 1800 cm^{-1} shift frequency and a 55.55 fs step size, the Fourier transform axis will be measured from 1800-2100 cm^{-1}.

Shifting the observed frequency is still a form of undersampling, and it lowers the measured signal strength. TPPI, like undersampling, increases the rate of data collection. The phase stability provided by the pulse shaping apparatus enables averaging during data collection, so faster data collection means faster averaging. In our experience, if 2D IR spectra are averaged for the same amount of time while fully sampling and while implementing a shift frequency, the resultant signal to noise ratios will be almost identical. Increasing the averaging speed with a shift frequency makes up for the loss of signal strength.

2.13 Chirp Correction

The shortest possible laser pulse for a given bandwidth is said to be transform-limited. A transform-limited pulse has a frequency independent spectral phase. A pulse with a frequency dependence to its spectral phase is said to be chirped. In the time domain, chirp causes a separation in the high frequencies and the low frequencies of the pulse spectrum. When the high frequencies temporally lead the low frequencies, a pulse has a negative chirp; the opposite condition is a positive chirp. Femtosecond pulses acquire some chirp whenever they pass through a material; the magnitude and sign of the chirp depends on the material. A negative chirp is often corrected by passing a pulse through a material that causes a positive chirp, and vice-versa.

The pulse shaper offers complete control of the spectral phase, so adjustment of the phase parameter in the frequency mask can compensate for chirp on the pump pulse. The AOM is a thick piece of Ge that adds a significant amount of chirp to the pulse. It is important to compensate for any chirp caused by the AOM or any other material in the beam path to accurately shape the pump pulse.

The spectral phase can be expressed as a Taylor series expansion around some center frequency, ω_o.

$$\phi(\omega) = \phi_o + \phi_1(\omega - \omega_o) + \frac{1}{2}\phi_2(\omega - \omega_o)^2 + \frac{1}{6}\phi_3(\omega - \omega_o)^3$$

The chirp parameters are optimized by measuring the amount of doubled light produced in a $AgGaS_2$ crystal as the coefficients ϕ_2 and ϕ_3 are scanned by the pulse shaper. The doubling efficiency in a $AgGaS_2$ crystal is strongly dependent on the energy density in the crystal, therefore, the shortest pulse will produce the maximum doubled light. Translating the second grating in the zero-dispersion stretcher to maximize the doubled light can compensate for some of the linear chirp. The pulse shaper can compensate for the chirp without translating the second grating, however, this often requires large coefficients ϕ_2 and ϕ_3.[19] Translating the second grating usually ensures both coefficients are optimized between -1 and 1, and avoids scanning the coefficients over a much larger range. Chirp correction is automated in the LabView code; instructions can be found in Appendix B.

2.14 Pulse Shaper Calibration

Recall, the zero dispersion stretcher spatially resolves the pulse spectrum at the Fourier plane, and the AOM shapes the pulse spectrum with a 10 μs acoustic wave that propagates through the Ge. The AWG digitizes a 75 MHz RF waveform with a 300 MHz clock rate. Therefore, 3000 samples from the clock create the 10 μs waveform that completely fills the Ge crystal. Accurate pulse shaping requires a calibration of the spatial position on the AOM, or the sample index, with the spectral frequency.

The shaped spectrum is measured at the CMOS array for calibration. Calibration requires the measurement of spectra with two different frequency masks. The first mask deflects 30 samples every 100 samples, and creates a comb shaped spectrum. The second mask deflects 30 samples in the middle of the spectrum; it creates a hole spectrum that is one of the 30 comb peaks. The hole spectrum defines the sample index of one frequency. The hole then overlaps with the comb to define the sample index of one of the comb peaks. This defines the sample index of all the comb peaks, because they are all separated by 100 samples. A calibration curve of spectral frequency versus sample index is created from the comb spectrum.[19] AOM calibration is automated in the LabView code; instructions can be found in Appendix B.

Figure 2.14: AOM Calibration

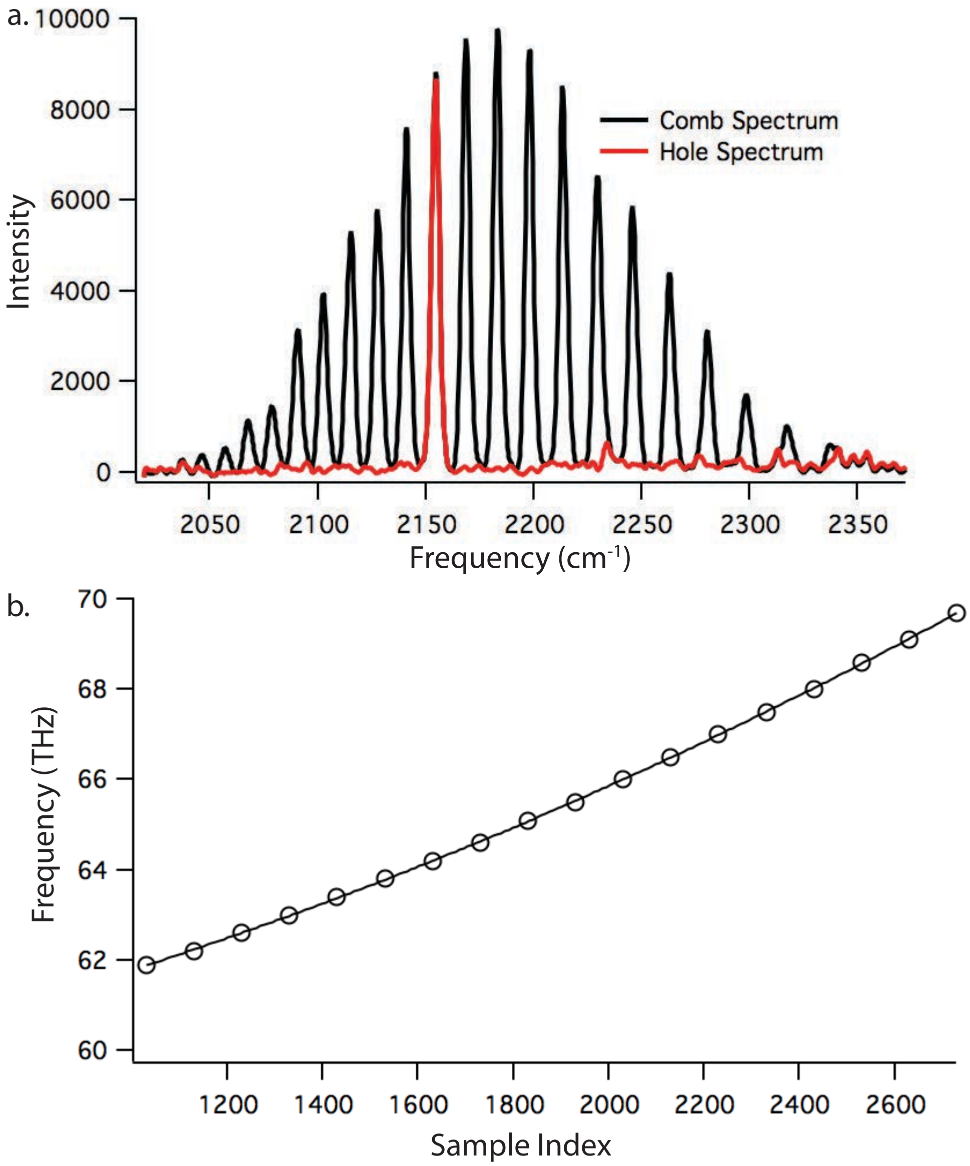

The comb (black) and hole (red) spectra collected for calibration (a), and the calibration curve calculated from the peak locations (b). The solid line in (b) is a 2nd order polynomial fit.

2.15 Triggering and Timing Electronics

The arbitrary waveform generator (AWG) creates the RF waveform that shapes the pump pulse spectrum. The RF waveform propagates through the AOM as an acoustic wave. The acoustic wave appears to be a standing wave on the timescale that the femtosecond IR pulse passes through the Ge, so the acoustic wave acts as a transmission grating that deflects the pulse spectrum. The amplitude and phase of the acoustic wave sets the amplitude and phase of the pump pulse spectrum. Therefore, accurate pulse shaping requires synchronization of the AWG to the phase and repetition rate of the laser.[19]

The commercial 800 nm oscillator (SpectraPhysics, Tsunami) produces an 80 MHz pulse train of femtosecond IR pulses. A photodiode in the oscillator measures the repetition rate of the laser, and creates an 80 MHz clock that is synchronous to the pulse train. The 80 MHz pulse train is sent to the commercial amplifier (SpectraPhysics, SpitfirePro); the amplifier produces amplified femtosecond pulses with a 1 kHz repetition rate. Commercial timing circuitry, called the timing delay generator (TDG) box, produces eight 1 kHz trigger outputs. The 1 kHz trigger lines are generated from the 80 MHz clock created by the photodiode in the oscillator, and are synchronous with the repetition rate of the oscillator.

The acoustic wave fills the Ge AOM in 10 μs, therefore the laser trigger must be delayed approximately 10 μs with respect to the AWG trigger, so the acoustic wave has time to fill the AOM. The synchronous 1 kHz trigger lines are generated by the laser circuitry, therefore it is much easier to put a long delay on the AWG trigger than a short delay on the laser trigger. A digital delay generator (Stanford Instruments – DG535) delays the AWG trigger ~990 μs with respect to the laser trigger. This creates the desired trigger pulse sequence; the AWG trigger leads the laser trigger by ~10 μs.

The pulse shapes output by the AWG must be synchronous with data collection at the CMOS array. Approximately 400 frequency masks are necessary to collect a 2D IR spectrum. The AWG loads the 400 frequency masks onto an onboard buffer; this allows the AWG to output the frequency masks at the 1 kHz repetition rate of the laser. The order of the shapes in the AWG buffer is defined when the shapes are loaded. After the buffer is loaded, the AWG remains idle until it receives a trigger. Each trigger releases 'the next' waveform in the buffer. The 401st trigger will output the first shape in the buffer; the AWG will continuously cycle through the buffer until a new set of waveforms is loaded.

The CMOS array accepts a line-rate trigger. This means each trigger will cause the camera to record the intensity measured at each pixel in the array. This measures the entire pulse spectrum. Each pulse spectrum is called a line of data. The camera digitizes the measured intensities with an onboard 14-bit A/D converter. The camera bundles lines of data into frames to facilitate data transfer. The number of lines in a frame must be defined before data collection, and is set equal to the number of shapes in the AWG buffer. After the camera receives the requisite number of triggers, it transfers the frame of data to the computer. Each frame contains all the data necessary to construct a 2D IR spectrum.

The camera, like the AWG, remains idle after it transfers a frame of data until it receives another burst of 400 triggers. However, unlike the AWG, the camera will timeout if it does not receive enough triggers to construct a frame. A custom circuit gates the triggers for the camera and the AWG. This ensures that the first line in every frame corresponds to the first frequency mask in the AWG buffer. A counter on a standard multifunction DAQ card (NI PCI-6036E) opens the gate on both triggers to ensure the camera and AWG each receive the same number of triggers and remain synchronous. The DDG sends a trigger synchronous with the laser and camera trigger to the counter. After the counter is enabled, it stays high until it counts 400 triggers. After the gate allows 400 triggers to pass to the camera and the AWG, it blocks the triggers during data transfer and processing, then opens to collect another 2D IR spectrum. The slowest step in the data analysis is Fourier transformation and image processing required to display a contour plot. Therefore, the data is averaged in the time domain, and the display of the averaged contour plot updates about every 50 scans. The number of averages per display can be changed during data collection.

A Firewire™ cable connects the camera to a computer, provides power to the camera, and transfers data from the A/D converter. The camera requires a differential line-rate trigger with TTL levels. A custom cable provided by the camera manufacturer transmits the trigger to the camera. The same home-built gate circuit converts the 1 kHz trigger synchronous with the amplifier output to a differential trigger required by the camera.

An enable pulse arms the RF amplifier. This is a safety feature that protects the electronic components of the amplifier. Overheating can cause severe damage to the amplifier. The amplifier will only operate when the enable pulse is high. The amplifier should be enabled at least 40 μs before the RF waveform arrives to ensure optimal amplification. A custom enable circuit outputs a 100 μs wide TTL pulse each time it is triggered. The DDG sends a 1 kHz trigger with a 910 μs delay to the enable circuit. The enable circuit arms the RF amplifier 80 μs before the RF waveform from the AWG arrives, and keeps it armed 10 μs after the RF waveform is gone. This ensures that the enable pulse does not cut off any of the RF waveform.

The AWG has four output channels that connect to a 4-way RF switch. The output of the RF switch is sent to the RF amplifier. A USB controller programmatically selects which channel is sent to the RF amplifier. The RF switch enables fast and easy switching between the four outputs of the AWG. Each output channel has a 4Msample buffer. Therefore, if one mask is 3000 samples, each channel can hold 1333 frequency masks. This translates to 333 time steps while using a 4 pulse phase cycle. This is more than enough time steps to collect most 2D IR spectra. However, it is possible to imagine an experiment that requires more frequency masks, such as a single beam experiment. A 2D electronic spectrum has been collected with a single beam, using a 16 pulse phase cycle. It has also been shown, in principle, that a 10 pulse phase cycle could collect a 2D spectrum with a single beam. A 10 or 16 pulse phase cycle reduces the number of time steps per channel to 133 or 83, respectively. The RF switch provides a means to quadruple the available buffer size. A fourth of the total masks could be loaded to each channel, and the RF switch could cycle between the channels during data collection.

The second channel on the AWG provides active feedback that buffer is ordered properly. The second channel is also filled with 400 shapes. The first shape is full-scale high voltage, and all the other shapes are 0V. Therefore, channel 2 is high when the first shape in the buffer is output, and low for all the other shapes. The multifunction DAQ card detects the output of channel 2 when the AWG is triggered. The DAQ card reports which shape in the sequence of 400 shapes was high. If it was not the first pulse, then the buffer is reloaded.

Figure 2.15: Electrical Connectivity Diagram

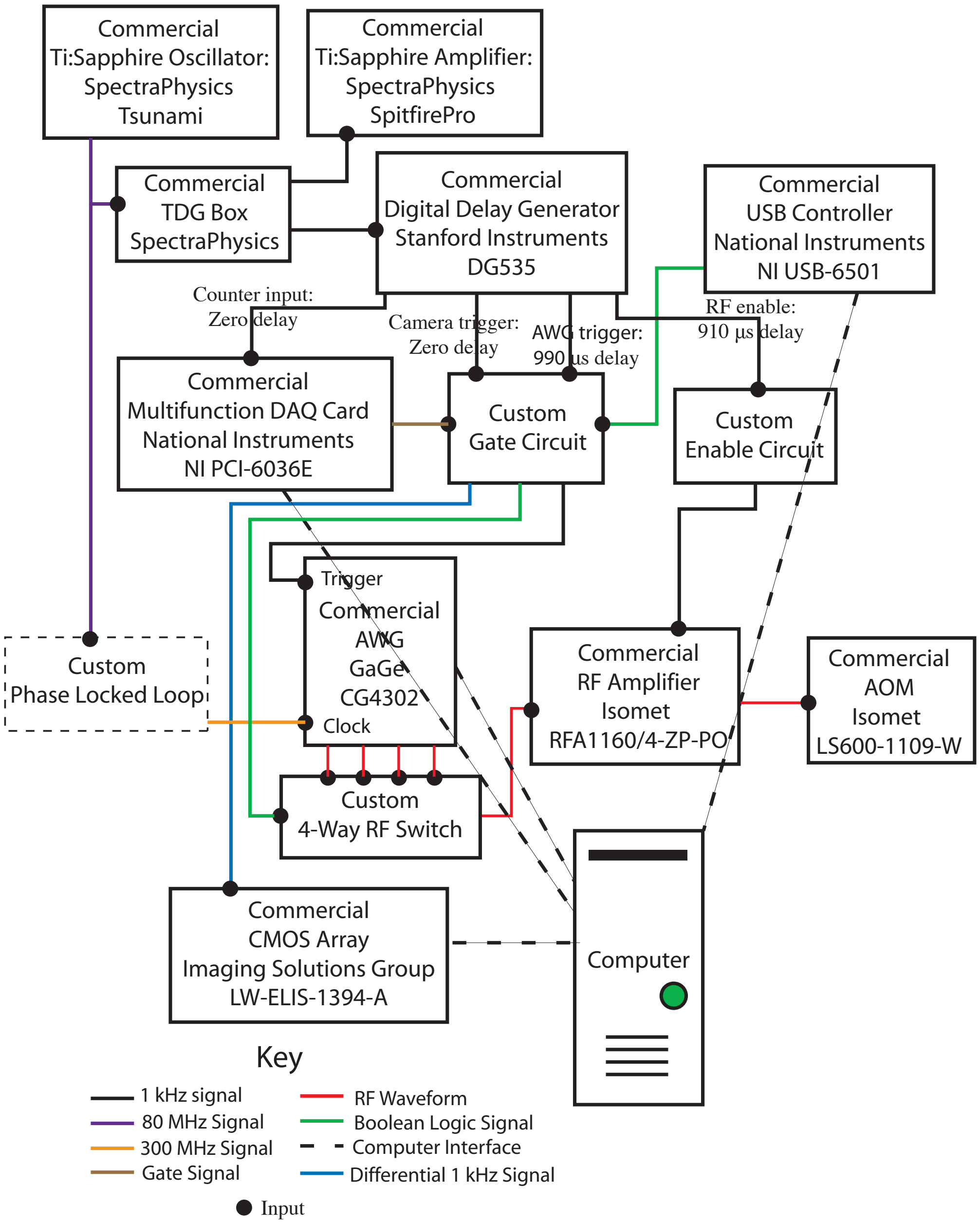

Figure 2.15 shows the electrical connectivity of all the components in the 2D IR apparatus. All triggers are derived from the 80 MHz oscillator signal. The DDG creates all the necessary delays. The custom gate ensures the camera and AWG remain synchronous, and creates the differential signal needed to trigger the camera. The DAQ card produces the wide enable signal that opens the gate. The custom enable circuit creates a wide 1 kHz pulse train that, when high, enables the RF amplifier. The 4-way RF switch programmatically selects the AWG channel that is sent to the RF amplifier. The phase-locked loop (PLL) provides the AWG a 300 MHz clock synchronous with the oscillator phase; the apparatus will function without the PLL, but with worse phase stability.

Figure 2.16: Timing Diagrams

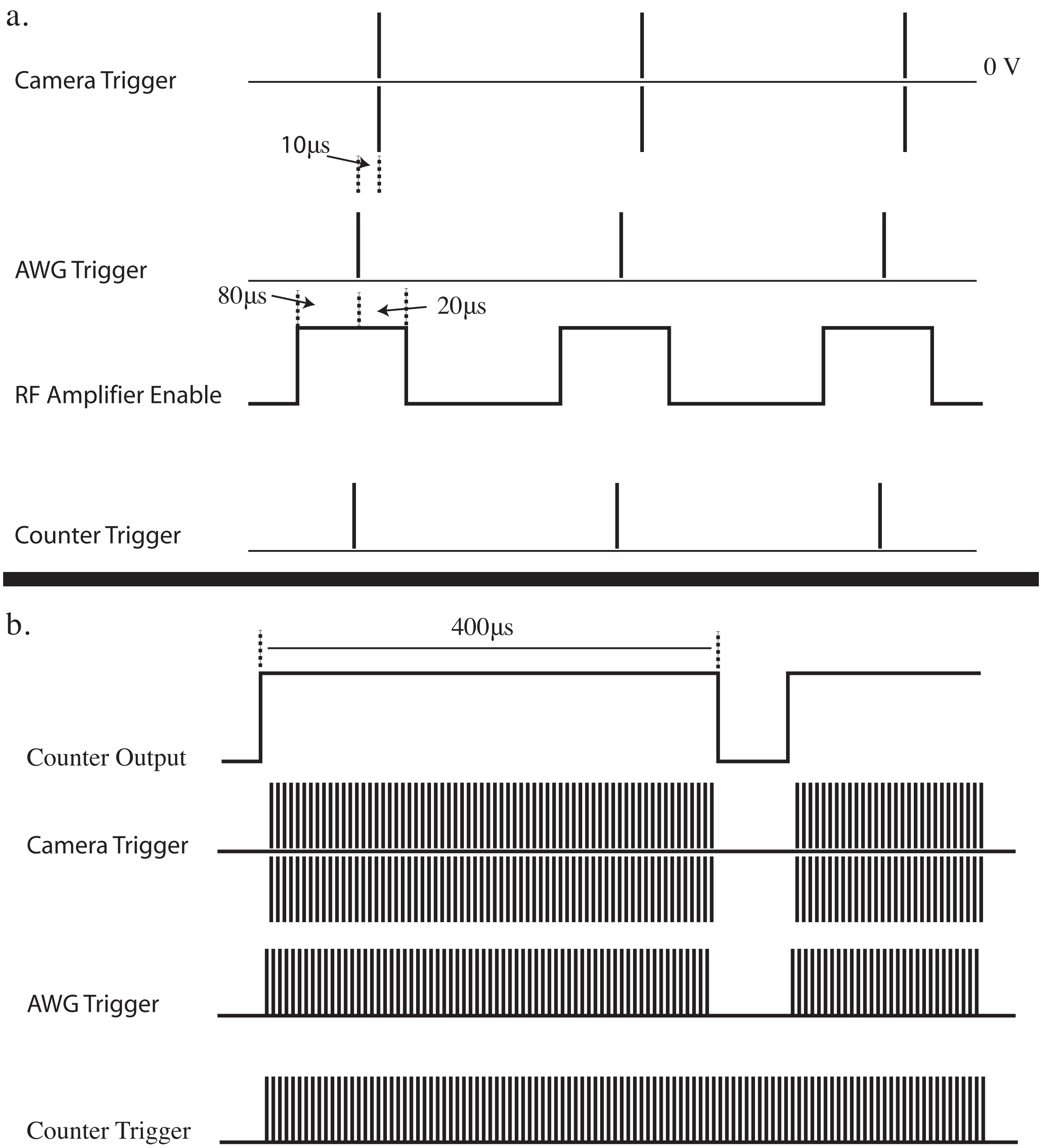

Timing diagram (a.) shows the relative time delays of the camera trigger, AWG trigger, RF amplifier enable, and counter trigger. All delays are generated with the DDG. The custom gate circuit converts the camera trigger to a differential trigger. The counter trigger and the AWG trigger are synchronous. Timing diagram (b.) shows the effect of the gate on the camera trigger and the AWG trigger. All other triggers are ungated, and continuously run; the counter trigger is an example of an ungated trigger.

2.16 CMOS Visible Detection Via Upconversion

The 2D IR spectrometer in our laboratory measures IR spectra with a visible CMOS array detector. IR detection with a CMOS array is a novel detection scheme, and it is discussed in detail in chapter 3. However, since most of the data presented in chapters 4,5, and 6 was acquired with a CMOS, it bears mentioning here.

The CMOS camera is a visible focal plane array. Upconversion of the probe beam enables visible detection. The 800 nm beam transmitted through the 50:50 beamsplitter is bandwidth narrowed in a three optic zero dispersion stretcher with a slit at the Fourier plane. The FWHM of the bandwidth-narrowed 800 nm beam is ~0.2 nm, resulting in an upconversion limited resolution of ~3 cm^{-1}. The mid-IR probe beam and narrow 800 nm beam mix in a $MgO{:}LiNbO_3$ crystal (θ=46.5°, type I), and produce a sum frequency centered at ~686nm.

2.17 Summary

The experimental design of 2D IR spectrometers has evolved greatly since the demonstration of the first hole-burning experiment. The four-wave mixing apparatus has greatly improved the time and frequency resolution of 2D IR spectroscopy. The pulse shaping apparatus offers the same time and frequency resolution as the traditional FWM apparatus, and collects a 2D IR spectrum in a fraction of a second, while the traditional FWM apparatus collects a spectrum in about an hour. The pulse shaper also offers perfect phase stability in the ω_1 and ω_3

axes, which eliminates the need to correct the phase during data analysis. Therefore, the pulse shaping apparatus has become the preferred data collection method in our laboratory. Figure 2.17 shows a schematic of the pulse shaping apparatus.

Figure 2.17: Pump-probe and Pulse Shaper Optical Setup

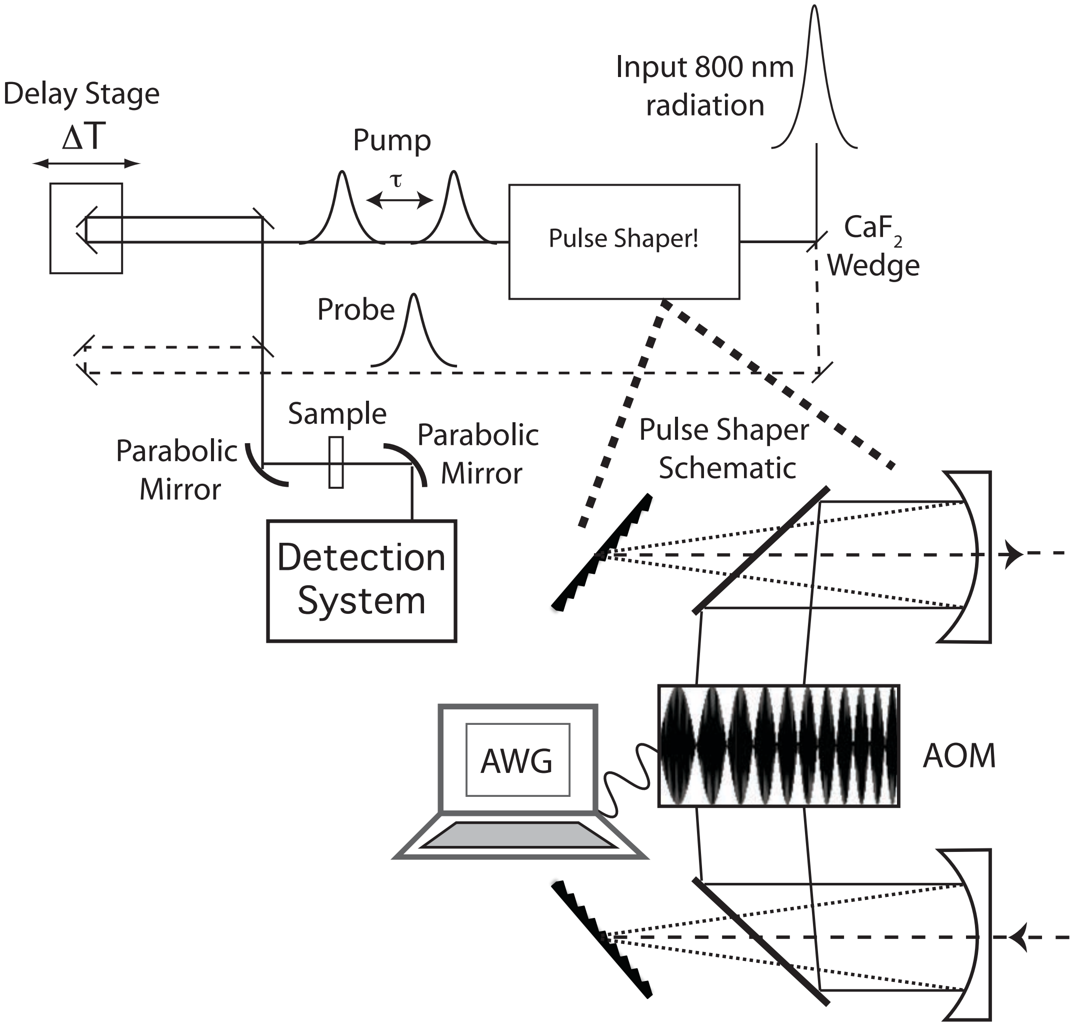

Figure 2.17 shows a simplified picture of the pulse shaping apparatus. A blowup of the pulse shaping optics is shown at the bottom of the figure. The design of the pulse shaping apparatus is identical to the design of the hole burning apparatus, except the etalon is replaced with a pulse shaper; it is a pump probe spectrometer that shapes the pump beam.

CHAPTER 3

THE CMOS ARRAY:

CHEAP INFRARED ARRAY DETECTION

3.1 Introduction and Motivation

Nonlinear vibrational spectroscopy has a myriad of applications in Physics, Chemistry, and Biology. Infrared (IR) radiation resonates with molecular vibrations, and is the source in most vibrational spectroscopy techniques. IR detection challenges must be overcome in these techniques. A Fourier-transform instrument normally collects linear IR spectra, however nonlinear spectroscopies require a more complicated data collection scheme. Multichannel arrays can acquire a linear spectrum in single laser shot, and greatly reduce measurement time of nonlinear spectra. Therefore, multichannel arrays are the preferred detectors for nonlinear vibrational spectroscopy. Unfortunately, IR arrays are extremely costly and lack the sensitivity and pixel density of cheaper visible arrays. Sum frequency generation (SFG) of the IR electric field in an appropriate nonlinear optical (NLO) crystal has been shown to be an effective strategy to gain the benefits of visible detection in the IR.[30-33] Traditional multichannel visible detectors are CCD arrays; high-speed CCD arrays that are able to acquire spectra at linerates ≥1kHz are quite costly.

Upconversion and visible detection has previously been applied to IR spectroscopy. The simplest upconversion setups use a narrow band visible source to upconvert the IR spectrum for visible detection. In this arrangement, the IR spectrum is the difference of the measured upconverted spectrum and the narrow band visible frequency. Upconversion has been used to gain the benefits of visible detection in the IR for many years. The Kubarych group routinely uses chirped pulse upconversion (CPU) to collect 2D IR spectra.[34, 35] In CPU, the zero order reflection from the compressor grating in a Ti:Sapphire amplifier is the narrow band visible source. This technique cleverly uses a source of visible light that is discarded in most optical setups. The uncompressed 800 nm light is strictly a broadband source, although only a small portion of the visible bandwidth temporally overlaps with the fs IR pulse in the NLO crystal. Careful calibration of the visible spectral profile and the time delay between the visible and IR pulses is required to deduce the visible frequency that temporally overlaps with the fs IR pulse in the NLO crystal.

3.2 IR Detection Via Upconversion

We use upconversion to measure IR spectra with a low-cost (<1500 USD) commercial CMOS array (Imaging Solutions Group LW-ELIS-1394A). The camera acquires a single spectrum at a maximum line rate of 10 kHz. The CMOS array lacks the sensitivity of a CCD array, however, heterodyne detected measurements do not require the single photon sensitivity available in a liquid nitrogen cooled CCD array. The CMOS array in our experimental apparatus is easily saturated with upconverted light.

The Ti:Sapphire amplified laser system in our laboratory (Spectra Physics, SpitfirePro) produces a surplus of 800 nm radiation. A portion of the excess 800 nm light is bandwidth narrowed and used to upconvert the IR spectrum. The commercial amplifier outputs a 1 kHz pulse train of 4 mJ pulses centered at 800 nm. A 50/50 beamsplitter divides the output. A home-built pulse shaper bandwidth narrows the transmitted 800 nm light. A diagram of the experimental setup and the bandwidth narrowing pulse shaper is shown in figure 3.1.

The pulse shaper is a three optic zero dispersion stretcher with a variable width slit (Newport SV-0.5) at the Fourier plane. The three optics are vertically displaced to conserve table space. An 1800 g/mm diffraction grating (Richardson Gratings) disperses the 800 nm light. A gold-coated spherical mirror (500 mm focal length) reflects the diffracted light to a square gold-coated mirror at the Fourier plane. The 800 nm light is sent back along the same path with a slight vertical displacement to isolate the output. A variable width slit, mounted on a mechanical stage in front of the Fourier plane mirror, narrows the output bandwidth. The slit width and position along the Fourier plane are varied to control the bandwidth and center frequency of the output, respectively.

The reflected 800 nm light seeds a home-built OPA/DFG that produces 5 μm light for 2D IR spectroscopy. The mid-IR light is sent to a pump-probe spectrometer. A direct IR pulse shaper frequency resolves the pump axis, as demonstrated previously by Zanni and coworkers. An 800 nm high reflector on CaF_2 combines the bandwidth narrowed 800 nm light and the IR probe light. Lenses, placed just before the beam combiner in each arm focus the light in a

Figure 3.1: Upconversion Optical Setup

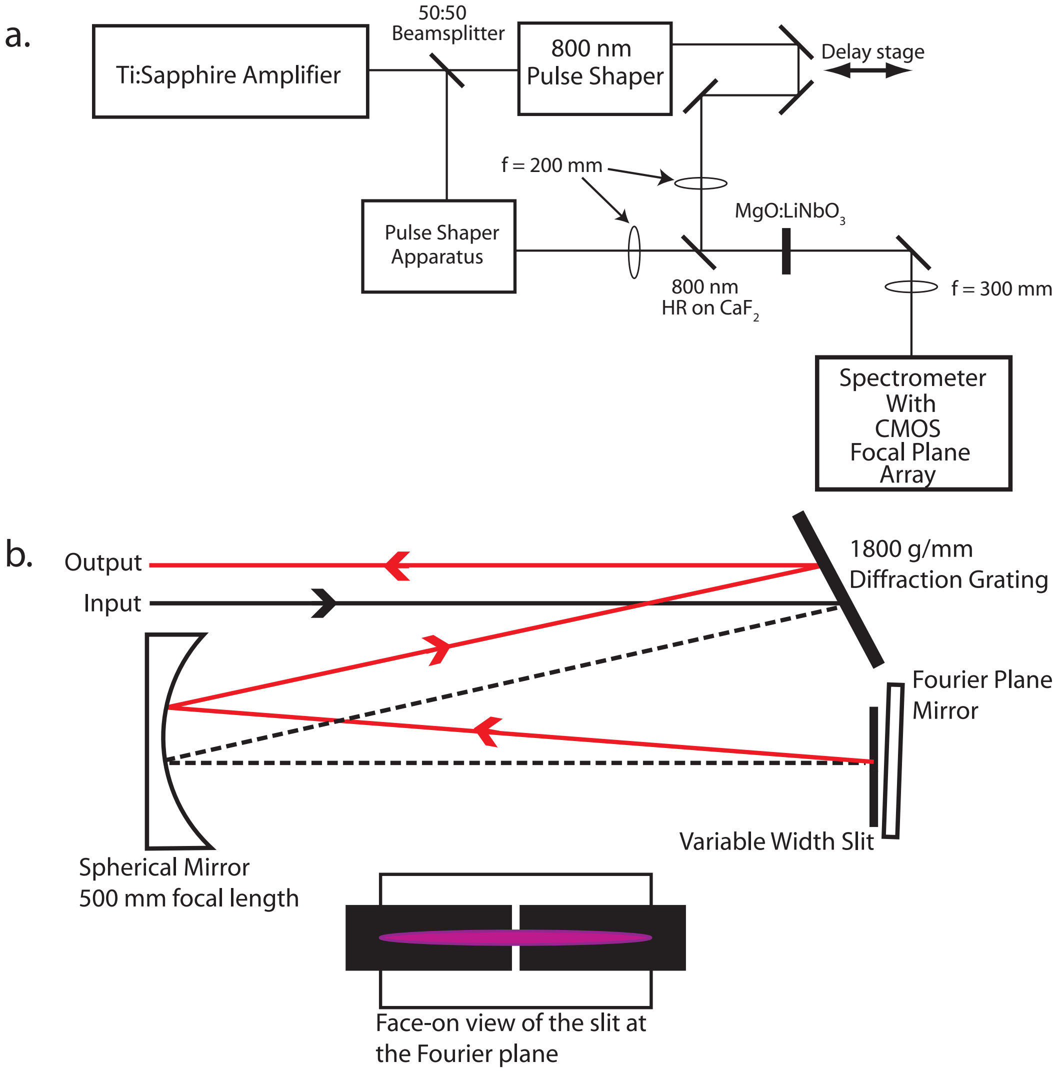

Optical layout of the entire experimental apparatus (a) and the bandwidth narrowing pulse shaper (b).

wedged 5x5x3 mm MgO:LiNbO$_3$ crystal (θ=46.5°, type I, Crylight Photonics). The two sources mix in the crystal in a χ^2 process to create a sum frequency. The sum frequency is visible to the naked eye. A lens focuses the sum frequency into a 300 mm commercial spectrometer (Princeton Instruments 2300i) that disperses the light to a focal plane array. The 1024 pixel single line CMOS array measures the upconverted probe spectrum on every laser shot.

The camera connects to a computer via a Firewire™ cable. The Firewire™ cable provides power to the camera, and transfers data from the onboard 14-bit A/D converter to the computer. The camera requires a differential line-rate trigger with TTL levels. A custom cable provided by the camera manufacturer transmits the trigger to the camera. A home-built circuit converts a 1 kHz trigger synchronous with the amplifier output to a differential trigger required by the camera. The camera must also be synchronous with the arbitrary waveform generator (AWG) used for pulse shaping. The same custom circuit gates the triggers for the camera and the AWG. A counter on a standard multifunction DAQ card (NI PCI-6036E) opens the gate on both triggers to ensure the camera and AWG each receive the same number of triggers and remain synchronous.

Figure 3.2a shows an overlay of the IR spectrum acquired via direct IR detection (red trace) and via upconversion and visible detection (black trace). A single channel HgCdTe (MCT) detector measures the IR intensity that passes through a 25 μm slit on the spectrometer as the grating is rotated. This confirms that CMOS detection via upconversion can reproduce the IR spectrum without distortions. Figure 3.2b shows a spectrum of the bandwidth narrowed 800 nm light. The absolute resolution of the spectrometer is limited by the bandwidth of the 800 nm radiation.

The pixel pitch of the CMOS detector is 7.8 μm. This corresponds to a detector limited resolution and bandwidth of ~0.4 cm^{-1} and ~400 cm^{-1}, respectively,

Figure 3.2: IR Pulse Spectrum and Narrow 800 nm Spectrum

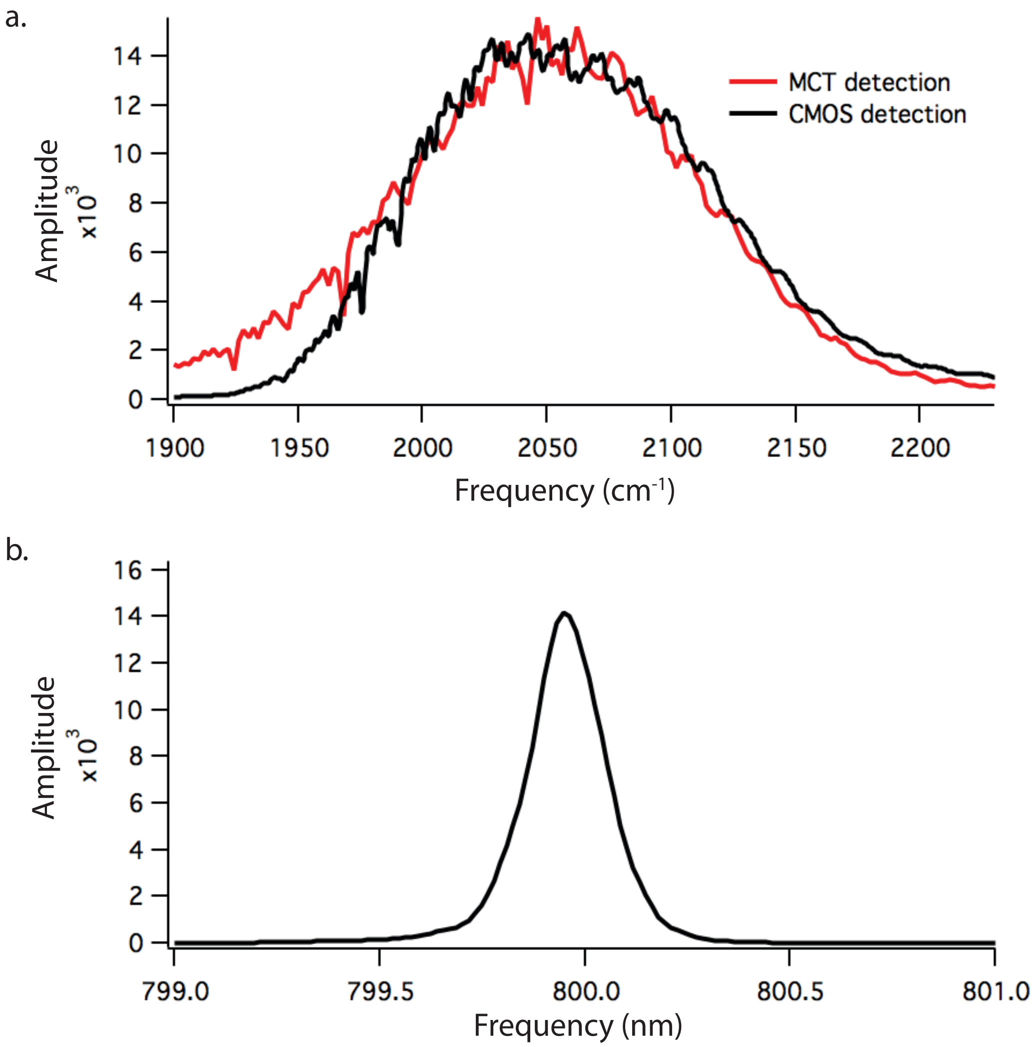

(a) IR spectrum collected directly with a single channel MCT detector (red trace) and with the CMOS array via upconversion (black trace). (b) Spectrum of the bandwidth narrowed 800 nm radiation used for upconversion. The FWHM is ~0.2 nm, corresponding to an upconversion limited resolution of ~4 cm^{-1} in our current experimental configuration.

while using a 1200 g/mm grating in a 300 mm spectrometer. The FWHM of the 800 nm light is ~0.2 nm, which corresponds to ~3 cm^{-1} resolution in our spectrometer. The resolution can be improved by narrowing the slit width in the 800 nm pulse shaper. The detector limited bandwidth and resolution can be easily adjusted by using a diffraction grating with a different groove density.

3.3 Converting a Barcode Reader Into a Focal Plane Array

The CMOS camera is not sold as a focal plane array. Therefore, some customization is required to adapt it for IR spectroscopy. The camera must mate to a spectrometer. A custom flange connects to the mounting holes on the front of the camera body, and mates to the spectrometer. The simple mounting flange is the only alteration to the camera body required to place the array at the focal plane; the mounting plate on the spectrometer allows adjustment along the focal axis.

The front face of the camera has a circular opening with a 1” diameter that allows light to hit the array. Four tapped M3 mounting holes in a rectangular pattern surround the opening. A custom flange connects to the four mounting holes on the camera, and then fastens to the spectrometer. The mounting flange on the spectrometer has three #10-32 tapped holes on a 3.60” bolt circle. The custom mating flange is pictured below in figure 3.3. The spectrometer flange allows translation along the focal axis, and rotation of the face of the array.

Custom software is required to control the camera. The camera is compatible with NI-IMAQdx drivers, so adaptation of the camera for IR spectroscopy is straightforward with LabView IMAQdx software. All camera control software used in the present experiment was developed using LabView.

The brightness setting on the camera must be increased from the default to ensure the baseline is above zero in our spectrometer; all other settings remain at the factory default values (digital gain, autoexposure, integration time). The CMOS array has a small slope to the baseline. Background subtraction corrects the sloping baseline. Raw and corrected baseline images are pictured below.

Figure 3.3: Camera Mounting Plate

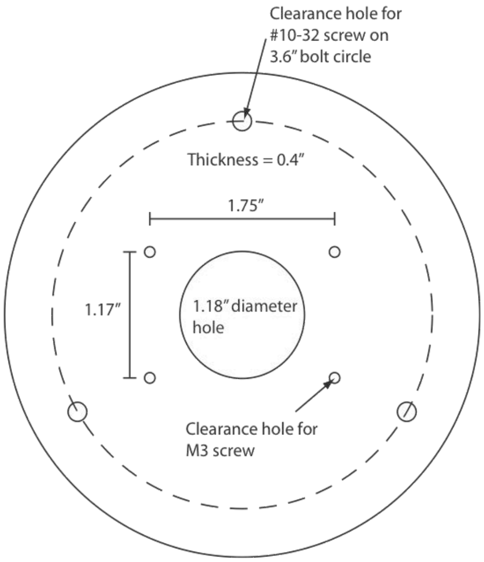

Custom mounting plate that attaches the CMOS camera to the standard spectrometer mounting flange. Adjustment of the spectrometer flange places the array at the focal plane of the spectrometer.

Custom calibration software was developed for the array. All calibrations fit the pixel positions of three known transitions to a 2nd order polynomial. A separate calibration is needed for each position of the diffraction grating. The CMOS array was calibrated at several grating angles around 800nm with Hg and Ne/Ar atomic lines. The atomic lines are not easily detected using the default integration time.

The camera clock rate dictates the maximum integration time. Therefore, the clock must be slowed to achieve a long enough integration time to observe the atomic lines. Unfortunately, the IMAQdx property node provided by NI does not offer access to the clock register, although, the register can still be addressed directly in LabView. The register location and acceptable values are given in the programmer's manual. Measurement of the bandwidth narrowed 800 nm radiation requires accurate calibration of the array at 800 nm.

Figure 3.4: Uncorrected and Corrected Array Baseline

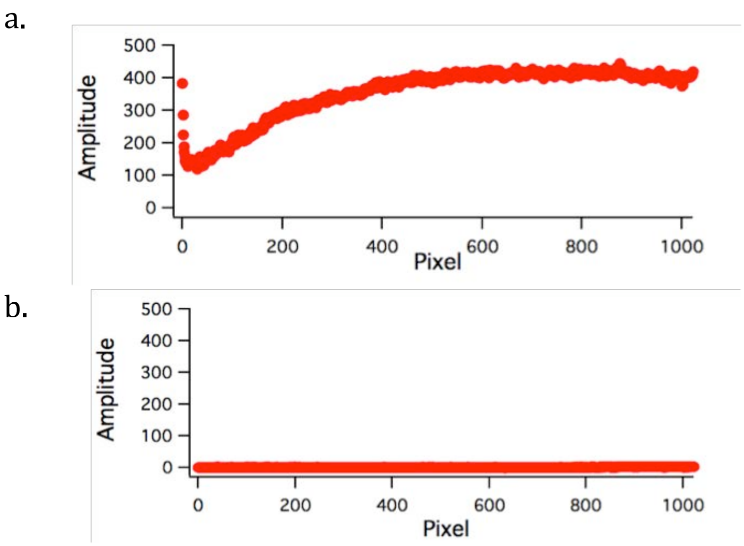

Uncorrected (a.) and corrected (b.) baseline spectra.

The sum frequency radiation is around 680 nm, and the atomic line lamp does not provide enough intense lines to calibrate the array at 680 nm. Therefore, IR transitions are the calibration reference at 680 nm. An FTIR measures the peak locations of the IR transitions. The known values of the IR transitions and the narrow 800 nm radiation determine the value of the peak locations of the sum frequency.

Figure 3.5: Live Pump-probe trace

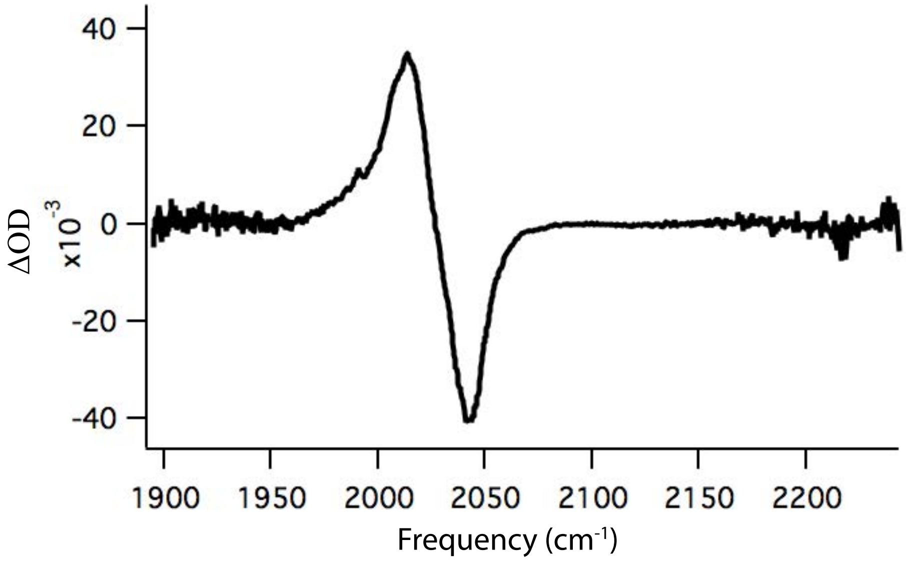

Pump-probe trace of 100 mM NaAzide in methanol. The trace is the average of 200 laser shots. The pump probe trace is used for real-time alignment of the 2D IR apparatus.

Figure 3.5 shows a pump probe trace of 100mM Sodium Azide in methanol at a pump-probe delay of 500 fs. The IR pulse shaper acts as an electronic chopper for the pump beam. The trace in figure 3.5 is the difference of 200 laser shots. The pump-probe trace acquired via upconversion and CMOS detection can easily be used for real time alignment of a 2D IR apparatus. Upconversion and CMOS detection offer a cheap alternative to traditional mid-IR array detectors. This provides vibrational spectroscopists the benefits of a multichannel array without substantial detector costs. The same spectrometer and array can also be used for visible spectroscopy. This intrinsic advantage of IR detection via upconversion greatly increases the versatility of the optical setup. These advantages make the detection of IR radiation with a CMOS array via upconversion an attractive option for vibrational spectroscopists.

CHAPTER 4

THE GREAT COMPARISON:
PULSE SHAPING VERSUS FOUR-WAVE MIXING

4.1 Introduction and Motivation

Two-dimensional infrared spectroscopy (2D IR) can reveal kinetic and dynamic information on a myriad of molecular systems. Despite the wealth of information that it can provide, relatively few research groups utilize 2D IR, because 2D IR spectrometers are expensive, and difficult to build and operate. Recently, direct infrared (IR) pulse shaping has been shown to simplify 2D IR data collection and analysis.[6, 11, 19, 27, 36-40] Chapter 3 demonstrates that a visible CMOS array coupled with upconversion offers an inexpensive detection alternative. These technological developments may allow more research groups to collect 2D IR spectra in the future.

Despite the advantages they offer, pulse shaping and upconversion detection have not been widely adopted in the 2D IR community. Many researchers fear that they could lower the signal to noise ratio (S/N) enough to make some experiments impossible. Both technologies should lower the S/N, however, the severity of the effect has not been quantified.

A traditional 2D IR spectrometer, the so-called four-wave mixing (FWM) apparatus, uses a boxcar geometry that focuses three independently controlled beams into the sample to produce a vibrational echo response. The vibrational echo is background free; therefore, all three excitation beams can be intense. After the sample, the vibrational echo overlaps with a local oscillator for heterodyned detection.

A pulse shaper transforms a pump-probe spectrometer into a 2D IR spectrometer. The pump-probe geometry produces less signal than the boxcar geometry because it is a self-heterodyned measurement, meaning the probe beam is the third electric field interaction and the local oscillator. Therefore, there is not independent control of the power of the third electric field and the local oscillator. The probe beam illuminates the detector in the pump-probe geometry, so the dynamic range of the detector limits the power of the third electric field and the local oscillator. The vibrational echo fluorescence overlapped with the local oscillator illuminates the detector in the boxcar geometry, so detector saturation only limits the local oscillator strength.

The pulse shaper produces spectra with a lower S/N, but also offers several advantages over the FWM apparatus. Optics overlap the signal and local oscillator in the FWM apparatus. A small alignment error in the overlap results in spectra with a phase error in ω_3. Visual adjustments of the frequency dependent phase during data analysis correct the phase error; therefore, a single scan must produce visible signal. Self-heterodyned detection eliminates the phase error between the signal and the local oscillator, so the pulse shaper can automatically average 2D IR spectra during data collection.

Active phase stabilization of the FWM apparatus can eliminate phase errors introduced by the delay stages.[28, 41, 42] To achieve active phase stabilization, a HeNe beam follows the same path as the IR, and is separated from the IR just before the sample. The HeNe light from pairs of beam paths overlap in a lens, and a detector counts the resultant interference fringes. Specialized optics then adjust the beam path according to the fringe count. Active phase stabilization is effective, but adds experimental complexity to the FWM apparatus, and is not commonplace.

The pulse shaper acquires data very rapidly. The shape of the pump beam scans the time delay, and changes on every laser shot. This eliminates the need to raster scan a mechanical translation stage, and matches the scan rate to the repetition rate of the laser. The pulse shaper can also control the phase of the two pump beams. NMR spectroscopists first realized the benefits of phase control, including phase cycling and phase incrementing. Phase incrementing shifts the observed frequency to a longer wavelength, which allows a larger fully sampled step size. Phase cycling enables difference detection without chopping the pump beam. In the traditional FWM apparatus, a mechanical chopper blocks one of the input beams on every other laser shot, and measures the difference of the response with and without the chopped beam. This subtracts all signals that do not include the chopped beam. Unfortunately, it blocks the signal on every other laser shot, so it only collects half the possible signal, and unwanted signal pathways that arise from light scattered from the chopped beam are not subtracted. The phase of the signal depends on the phase of the input beams, so shifting the phase difference of the pump beams by π inverts the sign of the signal. The difference of spectra with a π phase shift adds the phase sensitive response, and subtracts phase insensitive responses. Cycling the phase of the pump beams can subtract scattered light and all unwanted signal pathways without blocking the pump beam and giving up signal.

Recently, improvements to the traditional FWM apparatus have been shown to provide many of the benefits of pulse shaping without a pulse shaper.[28, 42] Continuous scanning enables rapid data collection with a mechanical stage.[43] Specialized optics can also create sub-cycle delays for a quasi phase cycling technique much like phase cycling with a pulse shaper. These improvements add experimental complexity to the FWM apparatus, and are not yet widespread. The traditional FWM apparatus raster scans the delay stage, and chops one of the input beams with a mechanical chopper. The traditional experimental design is clearly not optimized, but it is the most common 2D IR data collection method. It should also be noted that 2D IR spectra can be collected in the pump-probe geometry with mechanical stages. This technique gains the ω_3 phase stability of a self-heterodyned measurement, but loses the enhanced signal strength of the boxcar geometry.

Visible detection with a CMOS array will also lower the S/N of a 2D IR spectrometer. The IR probe beam must be upconverted to use a visible detector. Upconversion is an additional nonlinear optical process that will add noise to the measurement. The empirical effect of pulse shaping and visible detection is hard to predict.

This chapter compares the signal-to-noise ratio measured using a traditional FWM apparatus and a pulse shaping apparatus while keeping as many experimental variables constant as possible. It also compares the measured S/N of the pulse shaping apparatus with IR detection and with upconversion and CMOS detection. A dilute solution of methylthiocyanate (MeSCN) in dimethylformamide (DMF) provides the means for comparison. MeSCN absorbs at 2155 cm^{-1} in DMF, and is a weak chromophore ($\varepsilon \simeq 300 M^{-1} cm^{-1}$) by 2D IR standards. DMF is a background free solvent at 2155 cm^{-1}. A background free solvent was chosen to eliminate any errors in the measurement of the S/N that might occur because of a large solvent background. The goal of this chapter is to determine if pulse shaping significantly reduces the S/N that a traditional FWM apparatus easily achieves.

4.2 Experimental Details

Two different 2D IR experimental setups collected data in this chapter. Both systems have identical amplified Ti:Sapphire laser systems (SpitfirePro) that output 800 nm pulses at a 1 kHz repetition rate. The pulses are 90 fs in duration with about 4 mJ of pulse energy. A 5:3 reflective telescope reduces the beam diameter, and then a 50/50 beamsplitter divides the beam. The reflected light pumps a home-built two pass optical parametric amplifier (OPA) based on a β-barium borate (BBO) crystal (θ=27°, type II). The OPA produces two near-IR beams called the signal and idler. The energy difference between the signal and idler is tunable, and is adjusted to the desired mid-IR frequency. Difference frequency generation (DFG) of the signal and idler in a $AgGaS_2$ crystal (θ=50°, type II) produces the desired mid-IR radiation. Both systems produce 6 μJ mid-IR pulses 180 fs in duration centered at 2155 cm^{-1} with a full width half max (FWHM) of 115 cm^{-1}. The power, pulse duration, and focusing conditions of both systems were carefully kept as identical as possible. The optical setups of the 2D IR spectrometers differ greatly after the production of mid-IR radiation.

The FWM apparatus collects the heterodyned vibrational echo response as a function of one frequency and two time variables. Focusing three IR pulses in the sample produces the vibrational echo response. The two time variables are commonly known as the evolution time and the waiting time. The evolution time, τ, is the time delay between the first and second pulses, and the waiting time, T, is the time delay between the second and third pulses. The vibrational echo response is overlapped with a fourth electric field, the local oscillator, for heterodyne detection.

A monochromator disperses the overlapped echo and local oscillator to measure the frequency variable, ω_3. The monochromator scans ω_3 while a delay stage steps τ at a fixed value of T. The interference between the echo and the local oscillator produces an interferogram for each frequency value in ω_3. A Fourier transform of the τ axis converts it to the frequency domain, and provides the second frequency axis in the 2D IR spectrum.

ZnSe beamsplitters divide the mid-IR radiation to create the three pulses that generate the echo response. Mechanical stages fitted with retroreflectors scan τ and T. A 3° CaF_2 wedge sends a small portion of the third beam to a fourth delay stage to become the local oscillator. Square gold-coated mirrors form the three pulses into a boxcar geometry after the delay stages. A 90° off-axis parabolic mirror (100 mm focal length) focuses the three beams in the sample, and a second parabolic mirror collimates the light after the sample. An iris isolates the third order response in the $-k_1+k_2+k_3$ phase matching direction after the second parabolic mirror. A 2 inch 3°

CaF_2 wedge combines the signal and the local oscillator after the sample. A lens focuses the signal and local oscillator through the entrance slit on a commercial spectrometer. The monochromator output is sent through the exit slit to a single channel HgCdTe (MCT) detector. The τ axis is scanned with 11 fs steps from 0 to 3500 fs to collect the rephasing spectrum, and from -3500fs to 0 fs to collect the nonrephasing spectrum. The monochromator scans the ω_3 axis from 2180 cm^{-1} to 2100 cm^{-1} with 2 cm^{-1} steps. The sum of the rephasing and nonrephasing spectra produces an absorptive 2D IR spectrum. MCT array detectors are commonly used in FWM apparatuses to eliminate the need to step scan the monochromator, and increase the speed of data collection. Unfortunately, the high cost of an MCT array prevented its addition the FWM apparatus.

A mechanical chopper blocks every other laser shot in one of the input beams. A lock-in amplifier (Stanford Research Systems) locks into the 500 Hz chopper signal, and digitizes the detector output. The difference of chopped and unchopped signal eliminates signals that do not depend on all three electric fields. The lock-in time constant is set to 10 ms, so the signal is the average of ~5 laser shots, because the chopped shots do not produce signal. The optical layout of the FWM apparatus is pictured in figure 2.8.

The pulse shaper, modeled after the design of Shim et al,[6] is a zero-dispersion stretcher with a Ge based acousto-optic modulator (AOM) at the Fourier plane. An arbitrary waveform generator (AWG) sends a 75 MHz acoustic wave to the Ge. The acoustic wave creates a diffraction grating in the AOM. The phase and amplitude of the acoustic wave sets the phase and amplitude of the diffracted pump beam. The

AWG sends a different acoustic wave to the AOM on every laser shot, so the time delay and phase of the two pump pulses can be changed on every laser shot. Absorptive spectra are automatically collected in the pump-probe geometry because the rephasing and nonrephasing spectra are emitted in the same phase matching direction.

The pulse shaper apparatus produces a 2D IR spectrum using a pump probe geometry. The pump beam provides the first two electric field interactions, and the probe beam is the last electric field interaction and the local oscillator. The pulse shaping apparatus is discussed in more detail in chapter 2. Figure 2.6 illustrates the excitation of a sample with a pump-probe geometry, and with a boxcar geometry. An uncoated CaF_2 wedge reflects a small portion of the mid-IR radiation to become the probe beam. The remaining mid-IR light is the pump beam and is sent to the pulse shaper. Figure 2.17 shows the optical layout of the pulse shaping apparatus and the zero-dispersion stretcher. The pulse shaper employs frequency domain shaping to create two pulses in the pump beam, and scans the time delay between them, τ. The pulse shaper also controls the phase of the two pump pulses, which allows phase cycling. Phase cycling isolates the signal from the background, removes scatter, subtracts transient absorption signals, and shifts the signal to the rotating frame to allow a larger fully sampled step size. The pulse shaper red shifts the observed frequency 1800 cm^{-1}, and fully samples the observed ~355 cm^{-1} oscillation with 24 fs steps.

The time delay between the pump and probe beams is the waiting time, T. The shaped pump beam is sent to a mechanical delay stage fitted with a retroreflector to control T. A 90° off-axis parabolic mirror focuses the pump and probe beams in the sample. A second parabolic mirror collimates the probe beam after the sample. The probe beam is then sent to the detection system.

Two different detection systems collect pulse-shaper spectra. Both detection systems disperse the probe beam in a spectrometer. The first detection system scans the grating angle and collects the probe spectrum with a single channel MCT detector exactly like the four-wave mixing apparatus. The second detection system collects the entire spectrum of every laser shot with a CMOS array. Figure 4.1 is an illustration of the two different detection systems used by the pulse-shaping apparatus.

The CMOS array is a Si based visible detector, so the probe beam must be upconverted to the visible. A narrow band 800 nm beam mixes with the IR probe in a $MgO:LiNbO_3$ (θ=46.5°, type I) crystal, and the CMOS camera detects the resultant sum frequency signal. The 800 nm beam transmitted through the 50/50 beamsplitter at the beginning of the apparatus is bandwidth narrowed for upconversion. This beam is unused in the FWM apparatus. A three optic zero dispersion stretcher with a slit at the Fourier plane narrows the 800 nm beam to a FWHM of ~0.2 nm, corresponding to an upconversion limited resolution of ~3 cm^{-1}.

The concentration of MeSCN was adjusted to find the measurement threshold of the FWM apparatus. The lowest measurable concentration was ~120 mM with the current IR power, focusing conditions, and laser stability. The signal at long waiting times (> 5ps) could not be resolved with the four-wave mixing apparatus at the threshold concentration. A waiting time dependence of the signal was done with a 240 mM sample concentration. The sample is held between two CaF_2 windows separated by a 50 μm Teflon spacer. FTIR spectra confirm the absorbance of all samples is equal. The MeSCN was purchased from Acros Organics, and the DMF was purchased from Sigma-Aldrich. All chemicals were used as received.

Figure 4.1: Comparison Detection Schemes

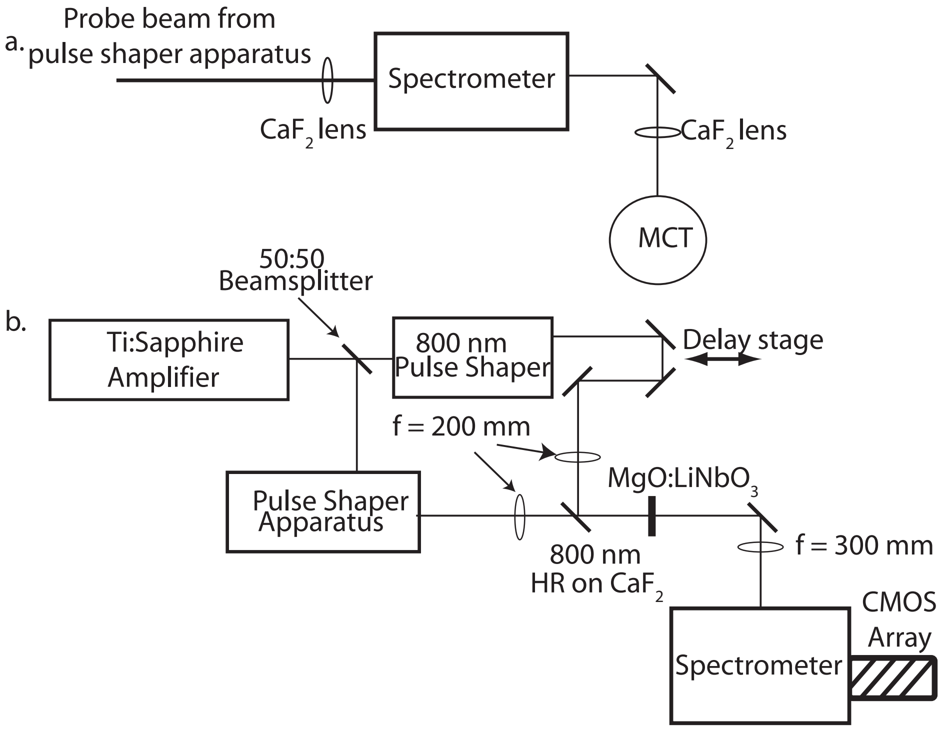

The single channel MCT detection scheme (a) collects the intensity of a single frequency on every laser pulse; the monochromater scans the grating angle to collect the entire pulse spectrum. The CMOS array detection scheme (b) collects the entire pulse spectrum on every laser pulse.

4.3 Results

The traditional FWM apparatus, with raster scanning and single channel detection, collects a 2D IR spectrum in about 1 hour. The pulse shaping apparatus, with single channel detection, collects and averages 115 spectra in an hour. Multichannel array detection greatly reduces the measurement time of both experimental setups, and continuous scanning enables rapid data collection with mechanical stages. This chapter, however, compares the S/N of a traditional FWM apparatus that raster scans a mechanical stage and a pulse shaping apparatus given the same data collection time.

Figure 4.2 shows 2D IR spectra of 240mM MeSCN at three different waiting times (T=250 fs, 20 ps, 30 ps) collected with the FWM apparatus (a), the pulse shaper with signal channel MCT detection (b), and the pulse shaper with upconversion and visible CMOS detection (c). All displayed spectra are normalized to the value of the 0 to 1 transition, and are plotted from -1 to 1 with 21 evenly spaced contours to allow visual comparison of signal to noise levels.

All four-wave mixing spectra are a single scan, and all pulse shaper spectra are the average of 115 scans. These two measurements use the same detection scheme, and require the same amount of measurement time.

The measurements provide a comparison of the S/N of the two optical setups while holding data collection time constant. The pulse shaping apparatus collects 115 spectra in about 1 minute via array detection. The MCT spectra and the CMOS array spectra compare the two data collection schemes while holding the number of averaged spectra constant.

Figure 4.2: Comparison 2D IR Spectra

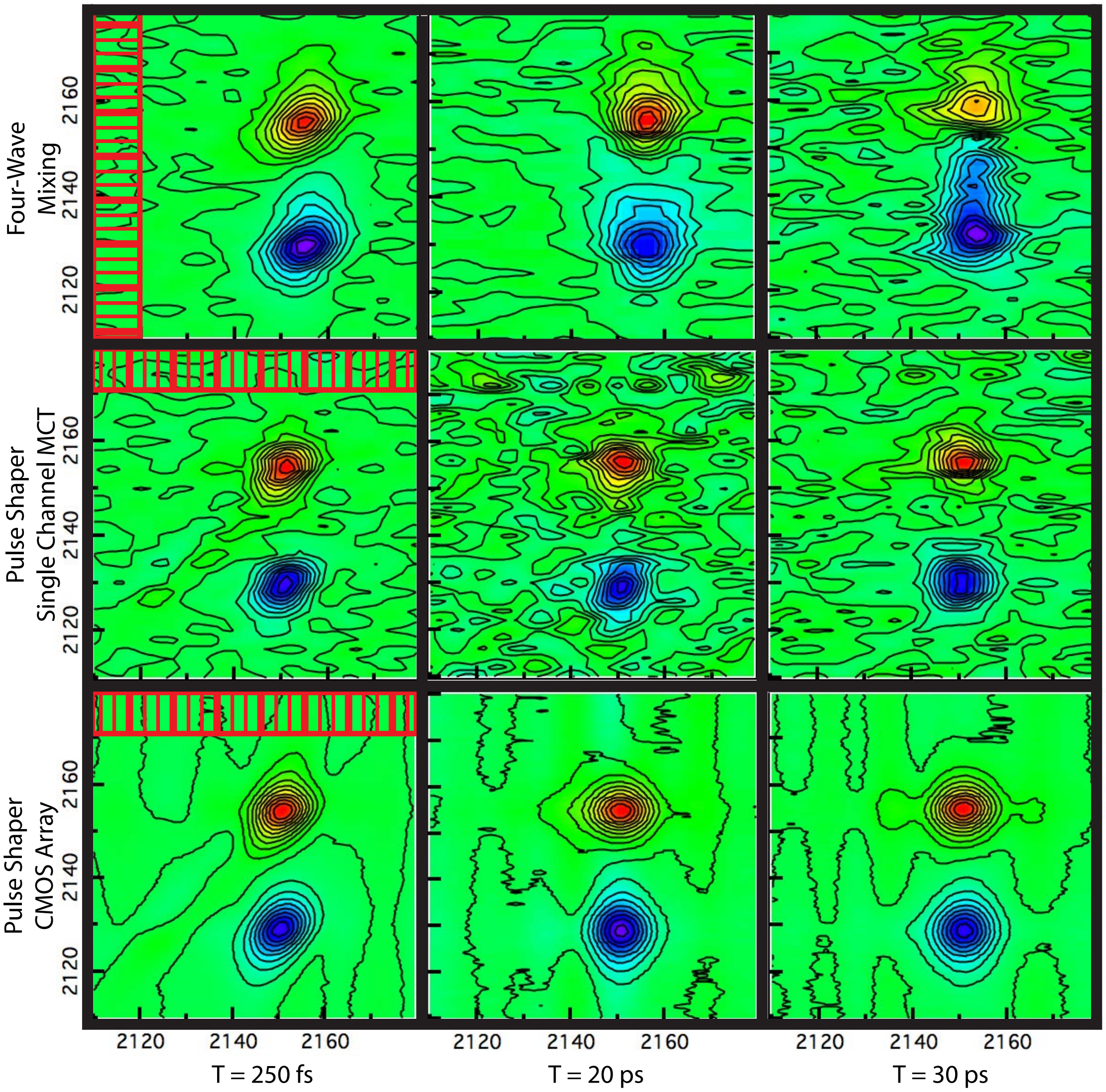

The rows are spectra collected with the three different data collection apparatuses compared in this chapter: FWM with single channel MCT detection, pulse-shaping with single channel MCT detection, and pulse shaping with upconversion and visible CMOS array detection. All spectra are 240 mM MeSCN in DMF. The columns are three different waiting time, T=250fs, 20ps, 30ps. The red boxes on the 240 mM spectra highlight the areas used in the RMS noise calculations.

The signal level is given by the difference of the maximum and minimum values of each spectrum. The noise of the pulse shaper spectra is the RMS noise of a spectral area from ω_3 = 2180 cm^{-1} to 2170 cm^{-1} and ω_1 = 2180 cm^{-1} to 2100 cm^{-1}. The noise collected by the array is correlated in ω_3, because the array collects the entire spectrum in a single shot, so the noise calculation is several uncorrelated slices. The noise of the four-wave mixing spectra is the RMS noise of the spectral area from ω_1=2110 cm^{-1} to 2120 cm^{-1} and ω_3 = 2100 cm^{-1} to 2180 cm^{-1}. Figure 4.2 highlights the areas used in the noise calculations for the pulse-shaper spectra (a), and the FWM spectra (b). A different spectral area is used for the noise calculation of the FWM data, because a small amount of signal is visible in the FWM data in the spectral range used for the pulse shaper noise calculation. The spectrometer used to collect the FWM data had a shorter focal length, so ω_3 resolution is not as fine. This causes small signals to appear at higher ω_3 frequencies in the four-wave mixing data. The noise calculations are done in areas where no signal appears.

The noise is essentially constant for each type of data collection regardless of the waiting time, as it should be. Therefore, the reported noise is the average noise of all spectra taken for each type of data collection: four-wave mixing, pulse shaping with single channel MCT detection, and pulse shaping with CMOS array detection. Table 4.2 shows the average noise found using each data collection apparatus. The average noise is used to calculate the S/N at each waiting time and concentration. Table 4.2 lists the signal and S/N of all the spectra taken. The pulse shaper apparatus collected three spectra at each waiting time for both data collection schemes. Therefore, the average noise reported for both data collection schemes is the average of 9 spectra, and the signal reported for each waiting time is the average of 3 spectra. The signal reported for each four-wave mixing spectrum is from a single scan. The reported FWM noise is the average RMS noise calculated in the three 240 mM spectra.

Table 4.1: Noise of the Compared Detection Schemes

Measurement Type	**Average Noise**
Single Channel (Pulse Shaper)	0.0037
Array (Pulse Shaper)	0.0024
Four-Wave Mixing	0.025

The RMS noise calculated from all spectra of each measurement type regardless of T delay.

Table 4.2: Signal and S/N of the Compared Detection Schemes

T (ps)	**Single Channel Signal**	**Single Channel S/N**	**Array Signal**	**Array S/N**	**Four Wave Mixing Signal**	**Four Wave Mixing S/N**
0.250	0.202	55	0.287	121	2.61	104
20	0.077	21	0.112	47	0.990	32
30	0.080	22	0.114	48	0.655	27

The signal and S/N measured by the three data collection methods at each T delay.

4.4 Discussion

The four-wave mixing apparatus, as expected, produces the greatest signal. The signal depends on the power of the three input beams and the local oscillator. The signal also greatly depends on the focal volume; a larger energy density produces a larger signal. The focal volume of the pulse shaping apparatus and the four-wave mixing apparatus were matched as closely as possible. The boxcar geometry is inherently more difficult to focus tightly, because three beams must spatially overlap in the focal volume instead of just the pump and probe beams. The IR power produced in the OPA/DFG was duplicated on both systems. The two systems have vastly different optical setups after the production of IR radiation, so the total throughput will be different. Matching the input IR includes the greater IR loss due to the pulse shaper in the comparison. The signal collected by the four-wave mixing apparatus can theoretically gain a factor of 2 with the addition of phase cycling, however, quasi-phase cycling via sub cycle delays was only recently demonstrated, and most labs still use a mechanical chopper. The signal collected by the FWM apparatus was approximately 10x greater than the signal collected with the pulse shaper.

The four-wave mixing spectra are single scans, while the pulse shaper spectra are the average of 115 scans, so the four-wave mixing spectra have greater noise. The greatest source of noise comes from the shot-to-shot stability of the laser. Laser shot-to-shot fluctuations are much greater than the dark noise of the MCT or CMOS detectors, so detector noise is expected to be negligible. Both laser systems are identical amplified systems, so the shot-to-shot fluctuations should be similar. If the noise scales ideally, and both systems produce the same noise, then the noise should scale as $\frac{1}{\sqrt{n}}$, where n is the number of shots averaged. A lock-in amplifier with a 10 ms time constant collects the FWM signal; therefore, each time step is the average of 10 laser shots. The pulse shaper uses a 4 pulse phase cycle, so each time step is the average of 4 laser shots. Therefore, each time point is the average of 460 laser shots after 115 spectra are averaged. The FWM noise, extrapolated to a single shot, is: $0.025 \times \sqrt{10} = 0.079$. The pulse shaper noise, extrapolated to a single shot, is: $0.0037 \times \sqrt{460} = 0.079$. The FWM apparatus and the pulse shaping apparatus have about the same noise per laser shot, which should be expected since the noise is limited by the laser shot stability. The exact details of the data collection can account for the small variation in the normalized noise, including the use of a lock-in amplifier in the four-wave mixing apparatus.

The noise on the upconverted signal should be greater because of the additional nonlinear process; however, it is found to have lower noise. This seems to indicate that the benefits of array detection outweigh the noise of the additional nonlinear process. The CMOS array collects 115 spectra in about 1 minute, while the single channel MCT detector collects 115 spectra in about an hour. The decreased data collection time eliminates noise due to long-term drift in the laser system. The array also collects the entire ω_3 spectrum of every laser shot, so there is not shot-to-shot noise across the ω_3 axis. The additional noise due to the sum frequency process must be less than the noise reduction benefits of array detection.

The collection of perfectly phased data offers several important benefits. Data analysis is greatly simplified. The phase of the 2D spectra does not need to be adjusted by hand; therefore, data analysis routines can be automated. The spectra can also be averaged during data collection, so the signal on a single scan does not need to be resolvable. Extended averaging allows the observation of signals that cannot be resolved with the traditional FWM apparatus. The lowest resolvable concentration of MeSCN in DMF taken with a traditional FWM apparatus with the previously specified IR power is 120 mM. Figure 4.3(a) shows the 2D IR spectra of 120 mM MeSCN taken with the three different data collection methods.

Figure 4.3: Comparison 2D IR Spectra: Low Concentration

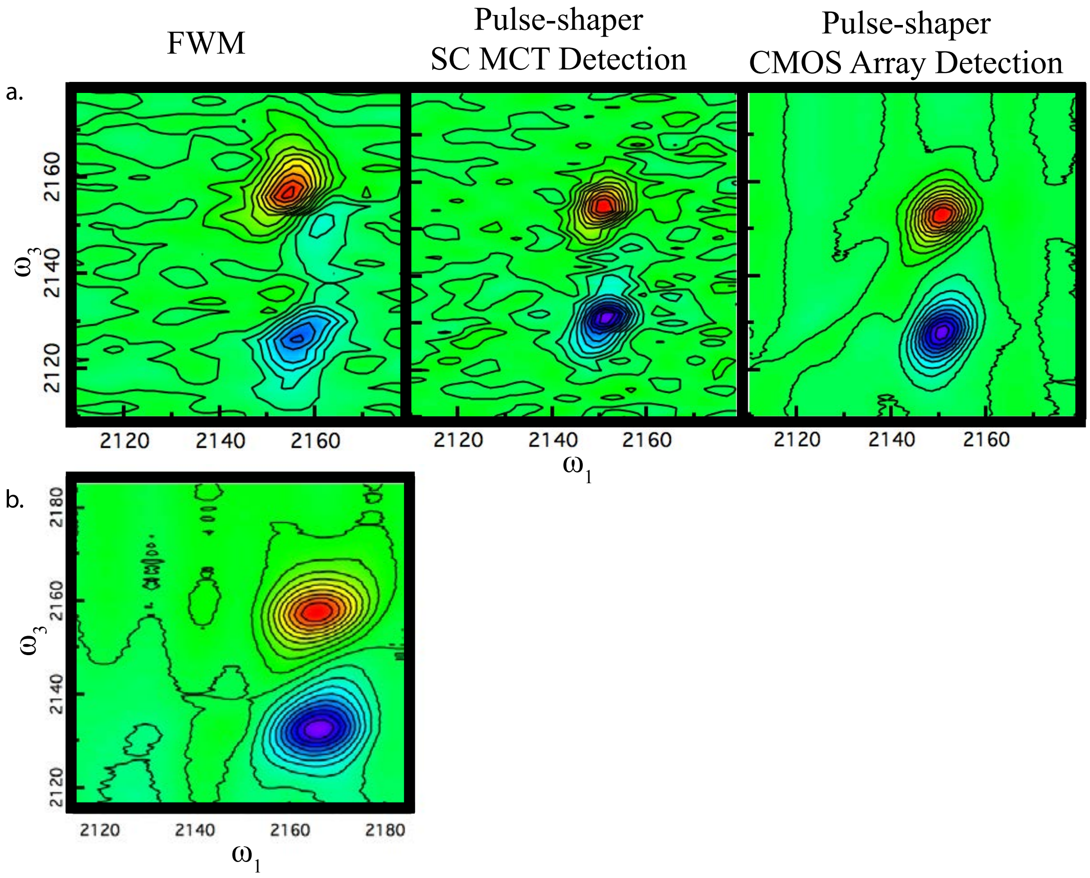

2D IR spectra of 120 mM MeSCN collected with the three different data collection apparatuses. All spectra were collected under the same conditions the 240 mM spectra was collected. The 2D IR spectrum of 30 mM MeSCN in water (b) appears at a different frequency because the solvent is different. The spectrum is the average of 10000 scans of the pulse-shaping apparatus with CMOS array detection.

An extra peak can be seen in the FWM spectrum, because the phase of the rephaing and nonprephasing spectra could not be adjusted to produce a perfectly absorptive spectrum. The nonrephasing signal is almost unidentifiable at this concentration. Figure 4.3(b) shows the 2D IR spectrum of 30 mM MeSCN in water taken with the pulse shaper and CMOS array detector after 10000 averages. The MeSCN signal is more difficult to resolve in water because water is not background free at 2155 cm^{-1}, and it absorbs some of the emitted signal. This demonstrates that signal averaging, made possible through phase stabilization, enables the observation of previously unobservable signals.

4.5 Conclusions

This chapter compares the S/N measured with a traditional FWM apparatus, and a pulse-shaping apparatus. The sample concentration chosen produced the smallest resolvable signal using the traditional FWM apparatus. Given the same data collection time, the pulse shaping apparatus produces a similar S/N. The pulse shaping apparatus can resolve smaller signals with greater averaging. A traditional four-wave mixing apparatus cannot average unresolved signals, because each spectrum requires visual adjustment of the frequency dependent phase. Active phase stabilization of the FWM spectrometer has been shown to eliminate this limitation. A fully optimized FWM spectrometer should produce greater signal, because it uses a boxcar geometry. However, the data in the chapter can only compare a pulse shaping apparatus to a traditional FWM apparatus. The data shows that there are no signals that cannot be resolved with a pulse shaper that can be resolved with a traditional FWM apparatus, and in fact signal averaging allows access to signals that would otherwise be impossibly difficult to observe. Furthermore, we demonstrate that upconversion does not add a measurable amount of noise, and that the benefits of array detection significantly outweigh the noise due to upconversion.

CHAPTER 5

^{15}N-LABELED 3-AZIDOPYRIDINE:
A PROMISING PROTON TRANSFER PROBE

5.1 Introduction and Motivation

Proton transfer reactions play an integral role in many chemical and biological processes including acid-base reactions, enzyme catalysis, and biological energy transduction.[44] A greater understanding of the chemical and energetic properties that control proton transfer reactions will provide valuable insight into these essential chemical processes. There are several competing theoretical models that describe ground state proton transfer kinetics. Although the predicted rate constants differ, most predict an equilibrium proton transfer rate between 10-100 picoseconds. These reaction rates are far too rapid to employ well-established NMR techniques to measure the reaction kinetics.

Time resolved measurements of excited state proton transfer reactions have previously been reported.[45-47] These measurements require disruption of the thermal equilibrium, and probe the reaction dynamics of an excited electronic state, providing a wealth of information on excited state proton transfer kinetics and dynamics. Theoretical modeling of excited state potentials is difficult and computationally expensive, and contains many energetic pathways that are not involved in the ground state reaction. Two-dimensional infrared (2D IR) spectroscopy can probe picosecond dynamics, and has been shown to observe chemical exchange processes in thermal equilibrium.[4, 48, 49] Therefore, 2D IR exchange spectroscopy provides a means to explore ground state proton transfer reactions.

Observation of hydrogen bond making and breaking has been the focus of several previous 2D IR exchange studies. In these experiments, the formation of a hydrogen bond causes a shift in the vibrational frequency of one of the hydrogen bonding partners. These systems involve weak hydrogen bonds; therefore, the complexes are constantly forming and dissociating in equilibrium. Two peaks are observed in the linear FTIR spectrum, one for the hydrogen-bonded complex, and one for the free molecule. The 2D IR spectrum shows two peaks along the diagonal that correspond to the two peaks observed in the linear IR spectrum. The growth of off-diagonal peaks in the 2D IR spectrum is a direct observation of chemical exchange, analogous to 2D NMR spectroscopy.

The chemical exchange measurements described above utilize a vibrational frequency shift in a bond directly involved in hydrogen bonding. The growth of cross peaks measures the formation and dissociation of a weakly hydrogen-bonding complex. A ground state proton transfer reaction in thermal equilibrium is most easily created with a strongly hydrogen bonded acid/base pair. Unfortunately, the A-H stretch potential in a strongly hydrogen-bonded complex, even if unreactive, is extremely anharmonic. The A-H stretch anharmonically couples with nearby overtones and combination bands, which results in an extremely broad and complex vibrational transition. The potential of a reactive system is even more complex because of the making and breaking of the A-H bond. Therefore, an acid/base complex with an indirect vibrational reporter of the protonation state of the complex is required.

Previously, we demonstrated that the azido stretch of 3-azidopyridine is a sensitive reporter of the protonation state of the pyridine ring.[50] This sensitivity suggests that the azido stretch may be used as a probe of a proton transfer system, or as a local pH reporter in larger biological molecules. Unfortunately, Fermi resonance couplings with nearby combination states complicate the azido stretching spectrum of 3-azidopyridine (3-AP). The 2D IR spectrum of coupled oscillators has cross peaks. The cross peaks due to couplings and the cross peaks due to chemical exchange are difficult to separate. A deperturbation calculation predicted an 8 cm^{-1} shift in the azido stretch upon protonation of the pyridine ring. However, the Fermi resonance couplings complicate the azido stretching spectrum, and we did not attempt to create an equilibrium to observe a ground state proton transfer.

Our collaborators showed that isotope labeling the azido group red shifts the vibrational frequency away from the dark states that split the azido stretch. FTIR spectroscopy of ^{15}N-labeled 3-azidopyridine (^{15}N-3-AP) shows that labeling the outer two nitrogen atoms shifts the azido stretch to 2044 cm^{-1}, and suppresses the Fermi resonance couplings.[51] This offers promise that ^{15}N-3-AP, complexed with an appropriate acid, can provide a probe of a ground state proton transfer reaction. Here, we present 2D IR spectra of ^{15}N-3-AP, and its complexes with formic acid (FA) and trifluoroacetic acid (TFA) in dichloromethane (CH_2Cl_2). Formic acid is not a strong enough acid to protonate ^{15}N-3-AP in CH_2Cl_2, and will form a neutral complex. Trifluoroacetic acid is much stronger, and it will form a charge separated complex with ^{15}N-3-AP in CH_2Cl_2. The elimination of the carbonyl stretch in the FTIR spectrum of trifluoroacetic acid confirms the formation of a charge-separated complex. Figure 5.1 shows the neutral and charge separated complexes. The absence of cross peaks in the 2D IR spectrum confirms that the Fermi resonance is sufficiently suppressed, and will not complicate chemical exchange measurements. The spectra of the complexes demonstrate that the azido stretch is sensitive to the protonation state of the pyridine ring, as predicted by the deperturbation calculation.

Figure 5.1: Neutral and Charge Separated Cartoon

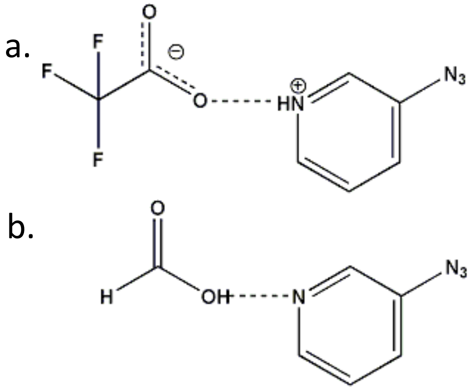

3-Azidopyridine and trifluoroacetic acid form a charge separated complex (a). 3-Azidopyridine and formic acid form a neutral complex (b).

5.2 Experimental

All 2D IR spectra was collected with the pulse shaping spectrometer and CMOS array detection scheme described earlier. Our collaborators at Franklin and

Marshall synthesized the ^{15}N-3-AzPyr.[51] All samples have a 50 mM ^{15}N-3-AzPyr concentration in CH_2Cl_2. The complex solutions contain an approximately equimolar ratio of acid and base. The sample is held between two CaF_2 windows separated by a 25 μm Teflon spacer. All solutions are in CH_2Cl_2 because it is polar enough to support a charge separated complex, and it will not be a competing hydrogen-bonding partner with the acid or base. The TFA was purchased from Acros, the FA was purchased from Sigma, and the CH_2Cl_2 was purchased from Fisher. All chemicals are commercially available, and were used as received.

5.3 Results

Figure 5.2 shows FTIR spectra of labeled and unlabeled 3-AP (a.), and FTIR spectra of ^{15}N-3AP, and complexes of ^{15}N-3AP with FA and TFA (b.). The FTIR spectra of the labeled and unlabeled 3-AP show the red shift due to isotope labeling. The spectra also confirm that the red shift moves the azido stretch away from the coupling dark states. The FTIR spectra in (b.) demonstrate that the ^{15}N azido stretch is sensitive to the protonation state of the pyridine ring. The uncomplexed azido stretch is centered at 2046 cm^{-1}. Complexation of ^{15}N-3AP with FA causes a modest 2 cm^{-1} shift of the azido stretching frequency to 2048 cm^{-1}. The azido stretch of the ^{15}N-3AP/TFA complex appears at 2054 cm^{-1}, an observed shift of 6 cm^{-1} between the neutral and charge separated complexes.

Figure 5.3 displays 2D IR spectra of uncomplexed ^{15}N-3AP, and of the neutral and charge separated complexes. Slices along the ω_1 and ω_3 axes at the frequency of the 0 to 1 transition are shown below each 2D IR spectrum. Contour plots often hide small signals; the slices enhance the appearance of small off-diagonal peaks that may arise from Fermi resonance couplings. Isotope labeling red-shifts the azido stretch, so Fermi resonance couplings that complicate unlabeled 3-AP should appear on the high frequency side of the spectrum. This chapter defines an ω_1 slice as a plot along the ω_1 axis for a set value of ω_3, and an ω_3 slice is a plot along the ω_3 axis for a set value of ω_1. A small peak appears in the ω_1 slices, however, no peaks appear in the ω_3 slices. Cross peaks due to couplings should appear along both the ω_1 and ω_3 axes. A Fourier transform is performed along the ω_1 axis to produce the 2D IR spectrum, therefore, small artifacts that appear in an ω_1 slice, but not in ω_3 can be attributed to the Fourier transform.

5.4 Discussion

The FTIR and 2D IR data of ^{15}N-3AP proves that isotope labeling the outer two nitrogen atoms in the azido group eliminates the Fermi resonance couplings found in the azido stretch of unlabeled 3-AP. Fermi resonance couplings complicate the spectroscopy of the azido stretch. Elimination of the Fermi resonance couplings through isotope labeling gives promise that the azido group is a viable probe for more complicated systems.

Isotope labeled 3-azidopyridine forms a neutral complex with FA, and a charge separated complex with TFA. This behavior was confirmed by the elimination of the TFA carbonyl stretch in the charge-separated complex. The FTIR spectra of the complexes clearly show that the azido stretch is sensitive to the protonation state of the pyridine ring. This sensitivity is expected, because the azido group is conjugated to the π system in the pyridine ring. A positive charge should cause a significant change to the electronic structure of the ring, and create a large enough perturbation to the π electronic structure to shift the azido stretch.

Figure 5.2: 3-Azidopyridine FTIR

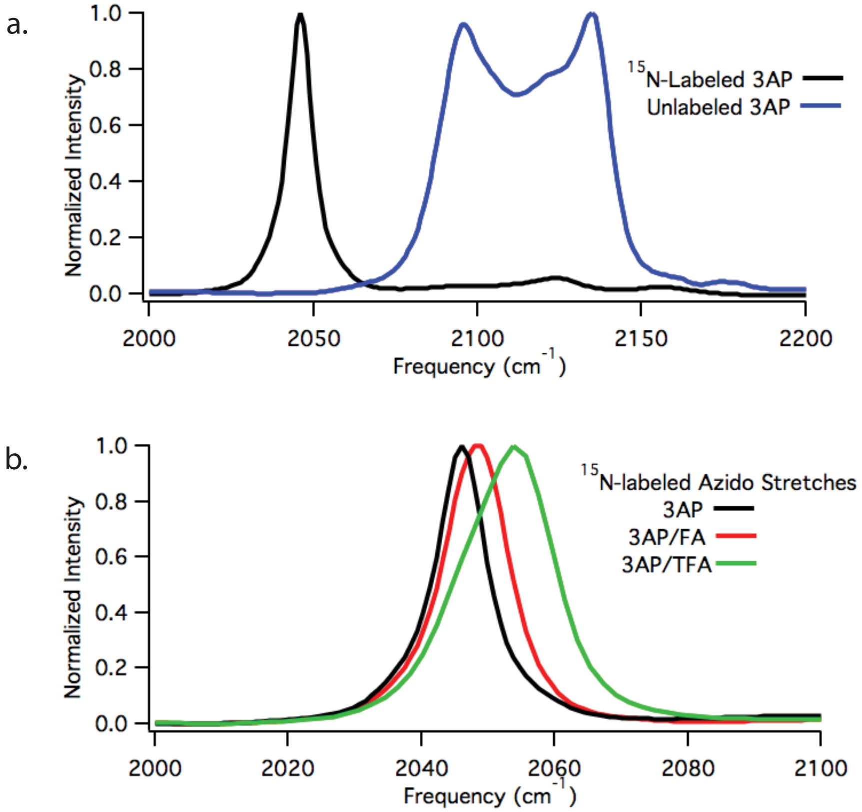

The FTIR spectra of labeled and unlabeled 3AP (a) shows that labeling the terminal two N atoms red-shifts the azido stretch and eliminates the Fermi resonance. The FTIR spectra of ^{15}N-labeled 3AP complexed with FA and TFA (b) shows that the azido stretch is a sensitive reporter of the protonation state.

In our previous paper we performed a deperturbation calculation on the azido stretch of unlabeled 3-AP in the same neutral and charge-separated complexes.[50] The calculation predicted an 8 cm^{-1} shift in the azido stretching frequency upon protonation of the pyridine ring. Here, protonation of the pyridine ring causes a 6 cm^{-1} shift in the azido stretch of ^{15}N-3AP, which is in close agreement with the deperturbation calculation.

Most theoretical models predict a ground state proton transfer rate between 10-100ps.[52-58] The lifetime of the azido stretch is approximately 4 ps. Traditionally, 2D IR spectra are observable up to 5 times the population lifetime. Rapid signal averaging, made possible here by the pulse shaping apparatus, allows smaller signals at longer waiting times to be resolved. However, even with signal averaging, the azido stretch will not be observable at T=100ps. Therefore, a protonation state reporter with a longer lifetime may still be required to observe a ground state proton transfer. The next step in this work is to find an acid that will complex with ^{15}N-3AP and create a proton transfer equilibrium in a non-hydrogen-bonding solvent.

Figure 5.3: ^{15}N-3AP 2D IR

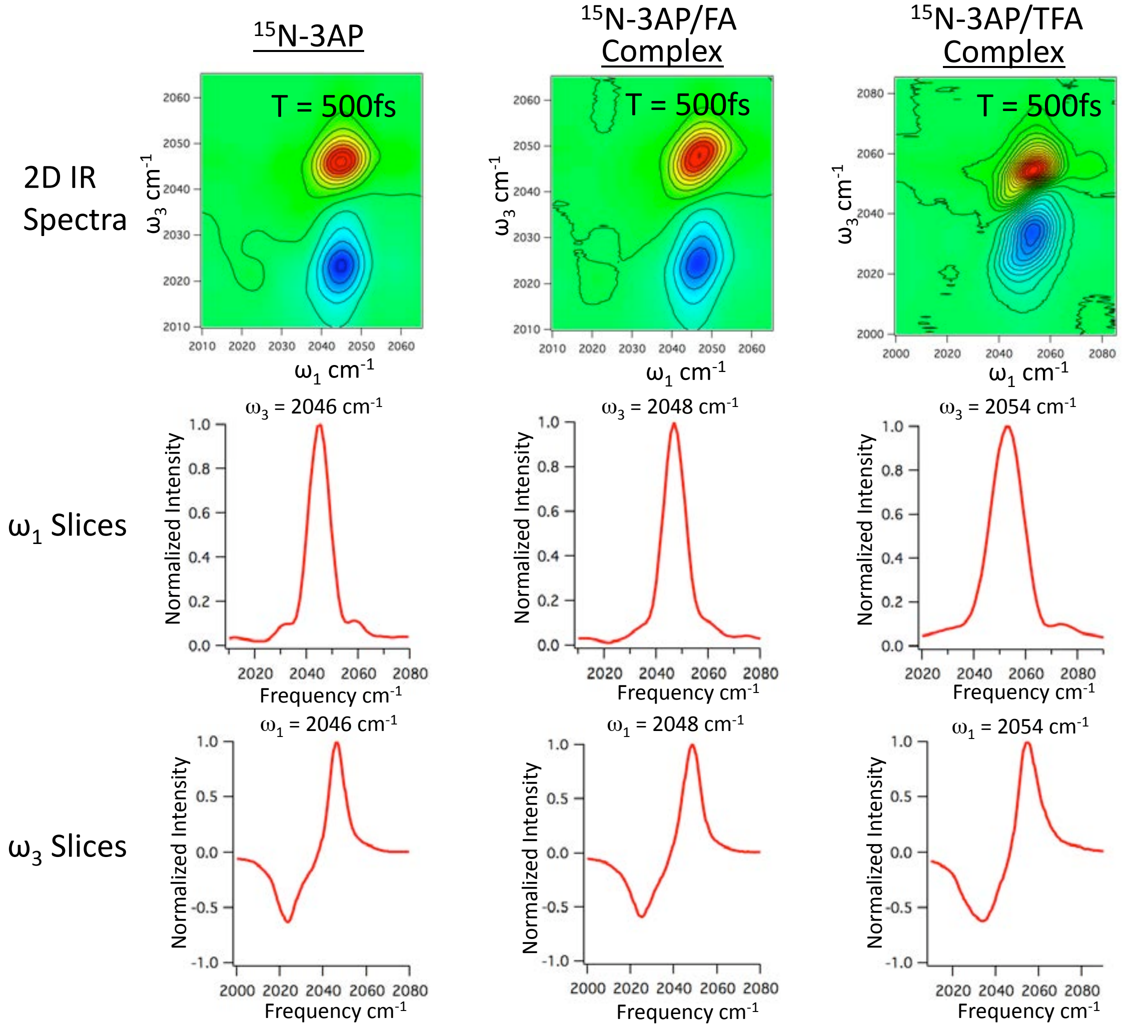

The top row shows 2D IR spectra of, from left to right, of ^{15}N-3AP, ^{15}N-3AP/FA complex, and ^{15}N-3AP/TFA complex. The middle row shows ω_1 slices of the 2D IR spectra, and the bottom row shows ω_3 slices of the 2D IR spectra.

5.5 Conclusions

The azido stretch of ^{15}N-3AP was shown to be sensitive to the protonation state of the pyridine ring. This sensitivity suggests that ^{15}N-3AP may be used in studies of hydrogen bonded complexes and ground state proton transfer reactions. This sensitivity was predicted in our previous study on unlabeled 3-AP. As was shown previously, Fermi resonance couplings complicate the spectra of unlabeled 3AP, making it an unsuitable probe of chemical exchange. Isotope labeling of the outer two nitrogen atoms eliminates the complicating Fermi resonance couplings, making chemical exchange experiments possible. The isotope labeled azido stretch may also be an effective local pH probe in large biological systems. Therefore, the ^{15}N labeled azido stretch has the potential to probe many interesting systems.

CHAPTER 6

GAUSSIAN AND NONGAUSSIAN DYNAMICS SEEN IN CYANATE: A SOLVENT STUDY

6.1 Introduction

Nonlinear vibrational spectroscopy can directly measure the spectral diffusion dynamics of solutions in thermal equilibrium. The ability to measure dynamical information is one of the main advantages of nonlinear spectroscopy over linear absorption spectroscopy. Three-pulse photon echoes first measured the spectral diffusion of vibrational frequencies.[59-63]

Spectral diffusion measurements were soon extended to 2D IR spectroscopy.[64-66] A 2D IR spectrum can be thought of as a correlation map between the pump and probe frequencies. Picture an ensemble of vibrationally active solutes in solution. The vibrational frequency of each solute molecule will depend on interactions with the solvent. When solvent molecules rearrange the vibrational frequency of the solute changes. In a 2D IR experiment, the first light/matter interaction labels the vibrational frequency of the solute molecule, and then the system is allowed to evolve during the waiting time, T. The last interaction probes the vibrational frequency after the system has evolved. A 2D IR spectrum is a plot of the frequency after the system has evolved (ω_3) versus the initial frequency (ω_1). If T is short compared to the time scale of solvent rearrangement, then the 2D IR spectrum appears elongated along the diagonal, and the spectrum is highly correlated; this is often called the static bath limit. If T is long compared to the timescale of solvent rearrangement, and the solute has time to sample all the solvent environments, the 2D IR spectrum will appear round, or uncorrelated; this is often called the motionally narrowed limit. Therefore, a measurement of the amount of elongation in a 2D IR spectrum will provide information rate of spectral diffusion in the solution.

A three-pulse photon echo measurement also labels the initial frequency with the first electric field interaction, allows the system to evolve during the waiting time, and probes the magnitude of the correlation to the initial frequency with the third electric field interaction. However, the three-pulse photon echo measurement is not spectrally resolved, so it measures the vibrational correlation integrated over the entire pulse spectrum. This integrated measurement can mask some important dynamical information, because the rate of spectral diffusion is not always constant across the entire bandwidth of a vibrational transition.

Frequency dependent spectral diffusion implies that the observed dynamics are non-Gaussian.[67] Analysis of spectral diffusion usually results in the extraction of the two-point frequency-frequency correlation function (FFCF); however, calculation of the FFCF assumes Gaussian dynamics, so it cannot uniquely describe non-Gaussian dynamics. Although the two-point FFCF cannot completely describe non-Gaussian dynamics, useful information can still be extracted from the same lineshape analysis used to extract the FFCF from Gaussian systems.[67]

Here, we present 2D IR spectra of cyanate in three different solvents: methanol (MeOH), D_2O, and N-methylformamide (NMF). The first two solvents display non-Gaussian dynamics, and NMF shows Gaussian dynamics. The centerline slope (CLS) decay extracts the spectral diffusion dynamics from the 2D IR spectrum. Analysis of 2D IR spectra with a CLS decay was first introduced by Fayer and coworkers,[68, 69] and it is commonly used to extract the FFCF from 2D IR spectra. Figure 6.1 shows the centerline in a 2D IR spectrum with Gaussian dynamics (a), and with non-Gaussian dynamics (b).

Figure 6.1: Gaussian and Non-Gaussian CLS

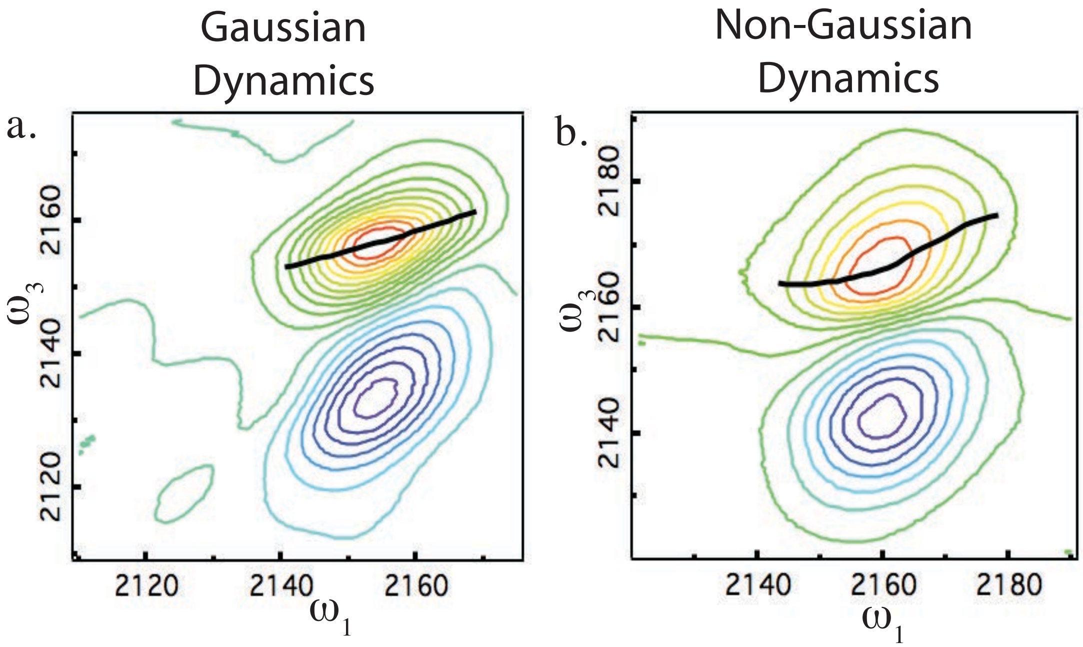

The center-line slop of a 2D IR spectrum with Gaussian dynamics (a), and non-Gaussian dynamics (b).

It is clear to see that, in the non-Gaussian spectrum, the CLS is frequency dependent. The dynamics of cyanate in methanol has previously been studied with a three-pulse photon echo,[60, 61] so the dynamics integrated over the entire spectral bandwidth can be compared with the spectrally resolved dynamics.

6.2 Experimental

A pump-probe spectrometer with a pulse shaper in the pump beam, as described in chapter 2, collected all the 2D IR spectra in this chapter. The 2D IR spectrometer utilized upconversion and visible detection with a CMOS array, as described in chapter 3. All chemicals are commercially available, and were used as received. The sodium cyanate, NMF, and D_2O were purchased from Aldrich. The MeOH was purchased from Sigma Aldrich. All samples were held between two CaF_2 windows separated by a 50 μm Teflon spacer.

6.3 Results

Table 6.2 lists the center frequency of the OCN^- vibration in each solvent, the frequency range fit on the red side, and the frequency range fit on the blue side of each data set. The frequency range used to fit the red side and blue side of the spectra is adjusted according the OCN^- bandwidth in each solvent. Figure 6.2 shows 2D IR spectra of OCN^- in each of the solvents at T=250fs. The black circles show the position of the centerline. The red and blue trace over the centerline highlights the frequency ranges used to fit the centerline. Non-Gaussian dynamics are clearly evident in the solutions of cyanate in MeOH and D_2O. Figure 6.3 shows the CLS decay of the red and blue frequency ranges in each solvent. All CLS decays were fit to a single exponential; the fits are shown as the black traces.

Table 6.1: Red and Blue Fit Regions

Solvent	Center Frequency (cm^{-1})	Red fit range (cm^{-1})	Blue fit range (cm^{-1})
NMF	2155	2143–2154	2158–2168
MeOH	2162	2146–2157	2165–2177
D_2O	2161	2142–2155	2161–2172

The solvent has a modest effect on the center frequency and FWHM of the OCN^- vibrational frequency. The fits in each solvent select spectral ranges over which the dynamics are frequency independent.

A system with frequency-independent spectral diffusion displays Gaussian dynamics. The CLS decays fit over the red and blue regions of the OCN^- in NMF transition are almost identical. Therefore, OCN^- in NMF diffuses with Gaussian dynamics, as is normally assumed when analyzing 2D IR spectra. The CLS decay of the red and blue regions in the other solvents shows dramatically different behavior, exhibiting non-Gaussian dynamics. Upon inspection, it is apparent that the red region always decays faster. The red region can also be fit to an exponential decay, as is normally done to analyze spectral diffusion data. The decay of the blue region is more complex. Following the analysis of Jensen and coworkers, we fit the blue region to an exponential function, even though an exponential function cannot accurately describe the decay of the blue region. Table 6.3 shows the time constants of the single exponential fits of the CLS decay for the red and blue region of each chemical system; it also lists the initial value of every measured CLS decay.

Figure 6.2: Cyanate in NMF, D_2O, and MeOH 2D IR

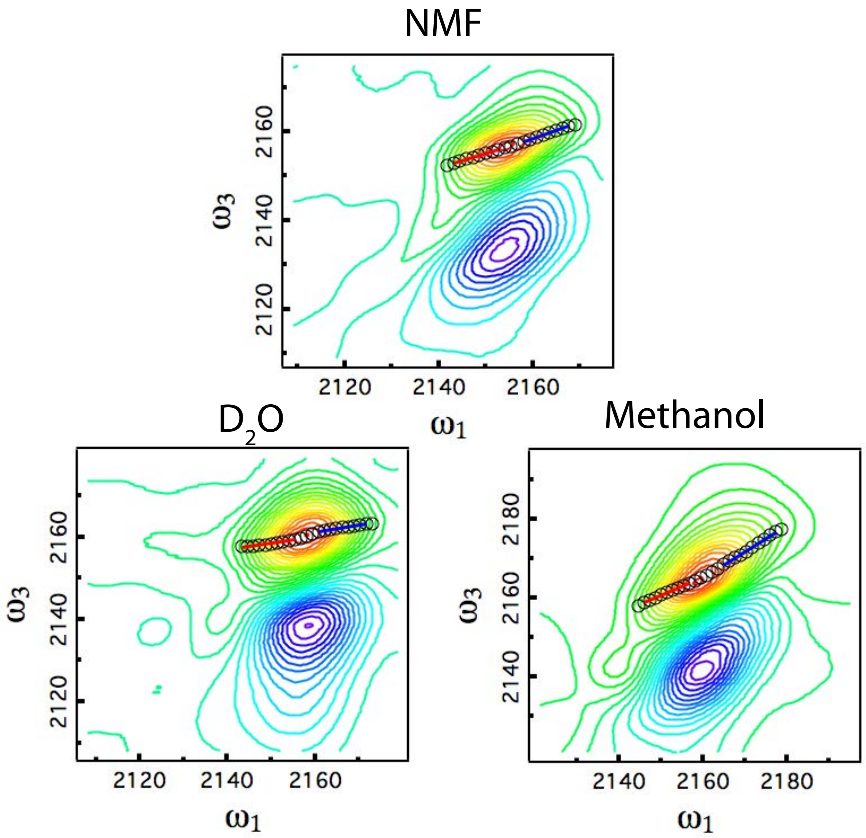

The center-line and red and blue fit regions for T=250fs spectra of $^-$OCN in each of the three solvents.

Table 6.2: Time Constants From Exponential Fits to CLS Decays

Solvent	τ (ps) - Red Region	τ (ps) - Blue Region	CLS at T=250fs – Red Region	CLS at T=250 fs – Blue Region
NMF	4.2	4.5	0.32	0.37
D_2O	0.66	3.0	0.2	0.19
MeOH	2.4	6.2	0.44	0.68

Time constants from the exponential fits to the CLS decays of the red and blue spectral regions, and the initial values of the CLS. The initial values give a measure of the amount of motional narrowing contribution to the CLS decay.

The initial value of the CLS decay provides a relative measure of the contribution of motional narrowing to the measured decay.

Figure 6.3: CLS Decays of Cyanate in NMF, D_2O, and MeOH

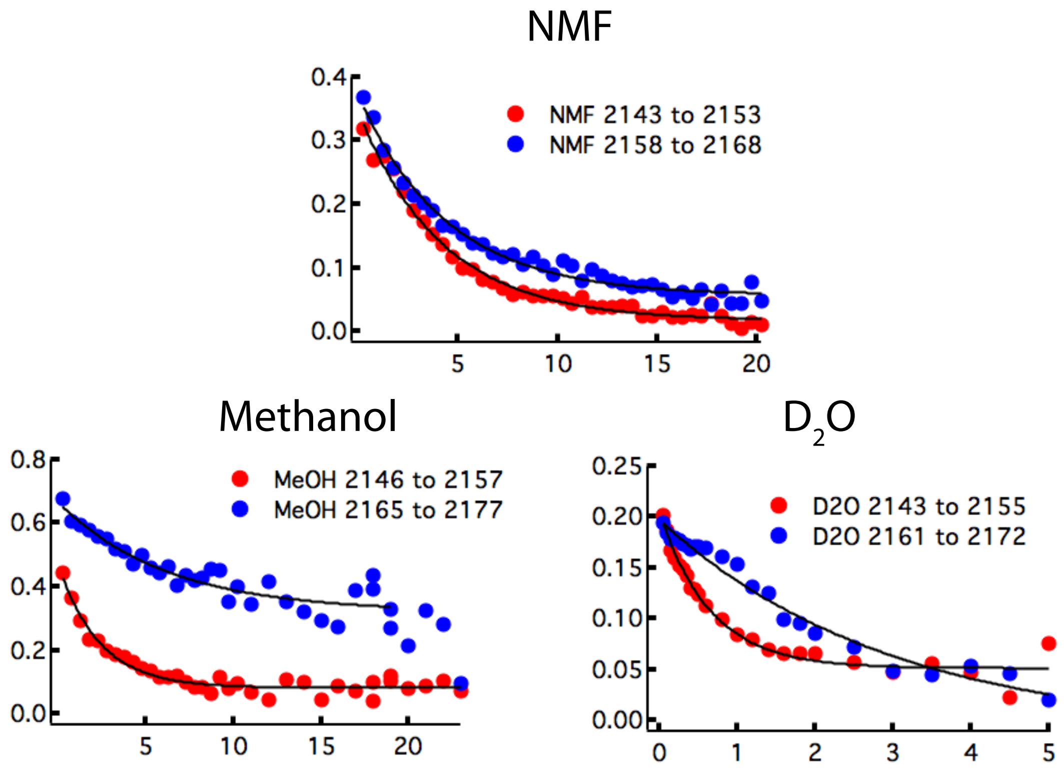

The CLS decays of $^{-}$OCN in all three solvents fit over the red and blue regions of the 2D IR spectrum. The single exponential fits are shown in black on top of each CLS decay.

6.4 Discussion

Spectral diffusion measurements extracted from nonlinear spectroscopies usually assume Gaussian dynamics; this is a often reasonable assumption. Non-Gaussian dynamics have been studied in chemical exchange systems.[70, 71] In these systems, non-Gaussian dynamics are modeled as the two Gaussian sub-ensembles that undergo exchange. This is a good model if the time scales for motion within each sub-ensemble are well separated from the time scales of exchange between the sub-ensembles. This assumption cannot always be made, as has been shown for water.[72] Three-dimensional infrared (3D IR) spectroscopy has been proposed as a means to measure non-Gaussian dynamics.[73, 74] 3D IR can directly measure the three-point correlation function, instead of the traditional two-point correlation function extracted from 2D IR and three-pulse photon echo spectra. However, it has recently been shown that useful information about non-Gaussian dynamics can be extracted from 2D IR spectra.[67]

We observe non-Gaussian dynamics in 2D IR spectra of OCN^- in MeOH and D_2O. The lineshape exhibits distinct dephasing dynamics on the red side and blue side of the spectra. This implies that molecules in a blue environment undergo spectral diffusion at a different rate than molecules in a red environment. The red and blue sub-ensembles cannot be cleanly separated and modeled as two Gaussian sub-ensembles undergoing exchange. However, the red and blue regions of the CLS decay can still be fit to provide a qualitative measure of the frequency dependent spectral diffusion.

The solvation of OCN^- in polar protic solvents has been addressed previously.[60, 75-77] Schultz et. al. made several assignments of the spectral features found in solutions of OCN^- in MeOH and NMF that offer some physical insight into the frequency dependent dynamics we observe. They deconvolute the OCN^- antisymmetric stretch in methanol into features from three distinct hydrogen-bonding environments, listed from red to blue: $OCN^{-}\cdots HOMe$, $OCN^{-}\cdots(HOMe)_2$, and $MeOH\cdots OCN^{-}\cdots HOMe$. They also deconvolute the OCN^{-} antisymmetric stretch in NMF into features from two distinct hydrogen-bonding environments: $OCN^{-}\cdots NMF$ and $OCN^{-}\cdots(NMF)_2$. According to this analysis, methanol hydrogen bonds with the nitrogen or the nitrogen and oxygen atoms in cyanate, while NMF only hydrogen bonds with the nitrogen atom in cyanate. Furthermore, the hydrogen-bonding environment involving both oxygen and nitrogen gives rise to the blue side of the cyanate transition in methanol. Therefore, the non-Gaussian dynamics observed in cyanate solutions in MeOH and D_2O can be assigned to slower spectral diffusion dynamics associated with hydrogen bonds to the oxygen atom in cyanate.

6.5 Conclusions

Non-Gaussian dynamics complicate the analysis of spectral diffusion in 2D IR spectra. Although analysis of 2D IR spectra has historically assumed Gaussian dynamics, meaningful interpretations of the 2D IR spectra can still be made. We apply simple exponential fits to the CLS decay of the blue and red spectral regions of a non-Gaussian 2D IR lineshape. This analysis provides a qualitative description of the spectral diffusion dynamics observed in the vibrational transition of the cyanate anion in several polar protic solvents.

CHAPTER 7

SUMMARY, IMPACT, AND CONCLUSIONS

We demonstrate that a pulse shaping 2D IR spectrometer collects 2D IR spectra with comparable S/N to spectra collected with a four-wave mixing spectrometer while holding data collection time constant. Extended averaging allows collection of spectra that were previously unobservable. We also demonstrate that a CMOS array detector offers a cheap detection alternative without giving up signal. Therefore, we conclude that pulse shaping with CMOS array detection is a cheaper, easier, and faster way to collect 2D IR spectra.

We show that ^{15}N-labeling 3-azidopyridine shifts the azido stretching frequency away from the complicating Fermi resonance couplings. The azido stretching frequency is sensitive to the protonation state of the pyridine ring. This implies that the azido stretching frequency could be used as a reporter of the local acidity in a large protein. We also hope to use the azido stretching frequency to directly measure ground-state proton-transfer kinetics.

Finally, we observe non-Gaussian dynamics in solutions of the cyanate anion in polar protic solvents. 2D IR spectroscopy provides a means to measure spectral diffusion, and distinguish Gaussian from non-Gaussian dynamics. Although the two-point FFCF cannot be extracted from a system that displays non-Gaussian dynamics, 2D IR spectra can still provide a wealth of insight into the underlying dynamics of these systems.

APPENDIX A: SCALE OPTICAL TABLE DRAWINGS

Appendix A includes scale drawings of all of the major components of the 2D IR spectrometer. The first 2D IR spectrometer built in our lab was a traditional four-wave mixing spectrometer. This instrument was destroyed in the flood of 2008. The pulse-shaping 2D IR spectrometer was designed and built after the flood. One of the mitigation requirements imposed by FEMA is that there must be a 48-hour evacuation plan for all vulnerable equipment. The post-flood design enables transportation of the entire apparatus without the need to dismantle the entire optical setup.

The optical setup was divided into five small pieces. Each piece was built on a research grade optical breadboard purchased from Newport. Protective boxes were built around each breadboard that shield the laser beams from air currents during data collection, and protect the optics if they need to be transported. The breadboards fasten to the main optical table via microlocks. The five boxes are given appropriate titles based on the optics they house: the OPA box, the DFG box, the pulse shaper box, the upconversion box, and the sample box.

Figure A1 is a scale drawing of the OPA box. It is built on a 3’x2’ breadboard. The input is the 800nm light from the laser. The OPA box houses all the optics in the two pass OPA, and the optics that separate and retime the signal and idler. The output of the OPA box is the signal and idler overlapped in time and space, and it is sent to the DFG box.

Figure A2 is a scale drawing of the DFG box. It is built on a 1.5’x2’ breadboard. The DFG box houses the $AgGaS_2$ crystal that difference frequency mixes the signal and idler to produce the desired mid-IR radiation. The box also houses the diode laser that overlaps visible red light with the mid-IR radiation to facilitate alignment, and a pyroelectric detector to provide a means to overlap the red light and IR light. The output of the diode laser is split. One red beam overlaps with the mid-IR in the DFG box, and the other red beam overlaps with the pulse shaper output. The mid-IR radiation passes through a Ge crystal in the AOM. The red tracer beam cannot pass through the Ge, therefore, the shaped beam must be re-overlapped with the red light after the AOM. The output of the DFG box is the mid-IR radiation overlapped with the red tracer beam.

Figure A3 is a scale drawing of the pulse shaper box. It is built on a 3’x2’ breadboard. The input is immediately divided into the pump and probe beams by a wedged CaF_2 substrate. The ~8% reflection is the probe beam, and the light that transmits through the substrate is the pump beam. The pulse shaper box, as its title infers, houses the direct IR pulse shaper. It contains a pyroelectric detector used for red light/IR light overlap. Finally, the pulse shaper box also houses an interferometric autocorrelator (IAC) that aids in the optimization of the OPA/DFG and the alignment and calibration of the pulse shaper.

A series of flipper mirror can direct either the probe or the pump beam into the pyroelectric detector. The red light/IR light overlap must be done with at least two mirrors and two detectors. Preferably, one of the detectors is close to the point of overlap, and one of the detectors is far away. The first overlap detector for the probe beam is found in the DFG box. The pyroelectric detector in the pulse shaper box is the second overlap detector for the probe beam, and the first overlap detector for the pump beam. A final pyroelectric detector is located in the sample box.

A flipper mirror can direct the probe beam into the IAC, and another flipper mirror and direct the pump beam there. The IAC has a $AgGaS_2$ doubling crystal and a liquid-nitrogen cooled MCT detector. The doubling efficiency of the probe beam is measured to optimize the alignment of the OPA/DFG. The MCT detector measures doubling efficiency of the pump beam as the pulse shaper scans the second and third order dispersion. The doubling efficiency increases as the chirp decreases, so the chirp parameters are set to the values that maximize the doubled light. The IAC can also measure the pulse duration of the probe and pump beams.

The pump and probe beams separately exit the pulse shaper box. The beams exit the pulse shaper box when all the flipper mirrors are turned down. Both beams output the sample box overlapped with the red tracer beam.

Figure A5 is a scale drawing of the sample box. It is built on two 4’x2’ breadboards. The sample box contains the final pyroelectric detector for red light/IR light overlap, the sample cell, and the spectrometer with the CMOS array detector. There are three sample box inputs: the probe beam, the pump beam, and the narrow 800 nm beam for upconversion.

A removable mirror on a post can direct either the pump or probe beams into the pyroelectric detector. The pump and probe beams are vertically displaced, so the post allows facile adjustment of the mirror height. The post holder does not block any beams, so it is permanently in place.

After the sample cell, a 2" gold mirror on a removable magnetic base can send the pump and probe beams to a liquid-nitrogen cooled MCT detector. This MCT detector measures the throughput through a pinhole at the sample position to optimize the spatial overlap of the pump and probe beams. It also measures the cross correlation signal produced by overlapping the pump and probe beams in a $AgGaS_2$ crystal. The maximum of the cross correlation signal is the point of temporal overlap of the pump and probe beams.

If the 2" gold mirror is removed, the pump and probe beams can be sent to the spectrometer. A $MgO:LiNbO_3$ crystal sum frequency mixes the mid-IR light and the narrow band 800 nm light to enable visible detection with the CMOS array. An 800 nm high reflector on a CaF_2 substrate overlaps the mid-IR radiation and the narrowband 800 nm radiation. A gold mirror on a removable magnetic base and a flipper mirror send the pump light into the spectrometer. If the magnetic base is removed, and the flipper mirror is turned down, then the probe light enters the spectrometer.

Figure A4 is a scale drawing of the upconversion box. It is built on a 3'x2' breadboard. The optics in the upconversion box bandwidth narrow the 800 nm output of the laser, and provide the necessary delay to temporally overlap the 800 nm light with the pump and probe beams. The input of the upconversion box is the light transmitted through the 50:50 beamsplitter at the beginning of the optical setup (not pictured). The output of the upconversion box is the bandwidth narrowed 800 nm radiation for upconversion; it is sent to the sample box.

Figure A1: OPA Box Scale Drawing

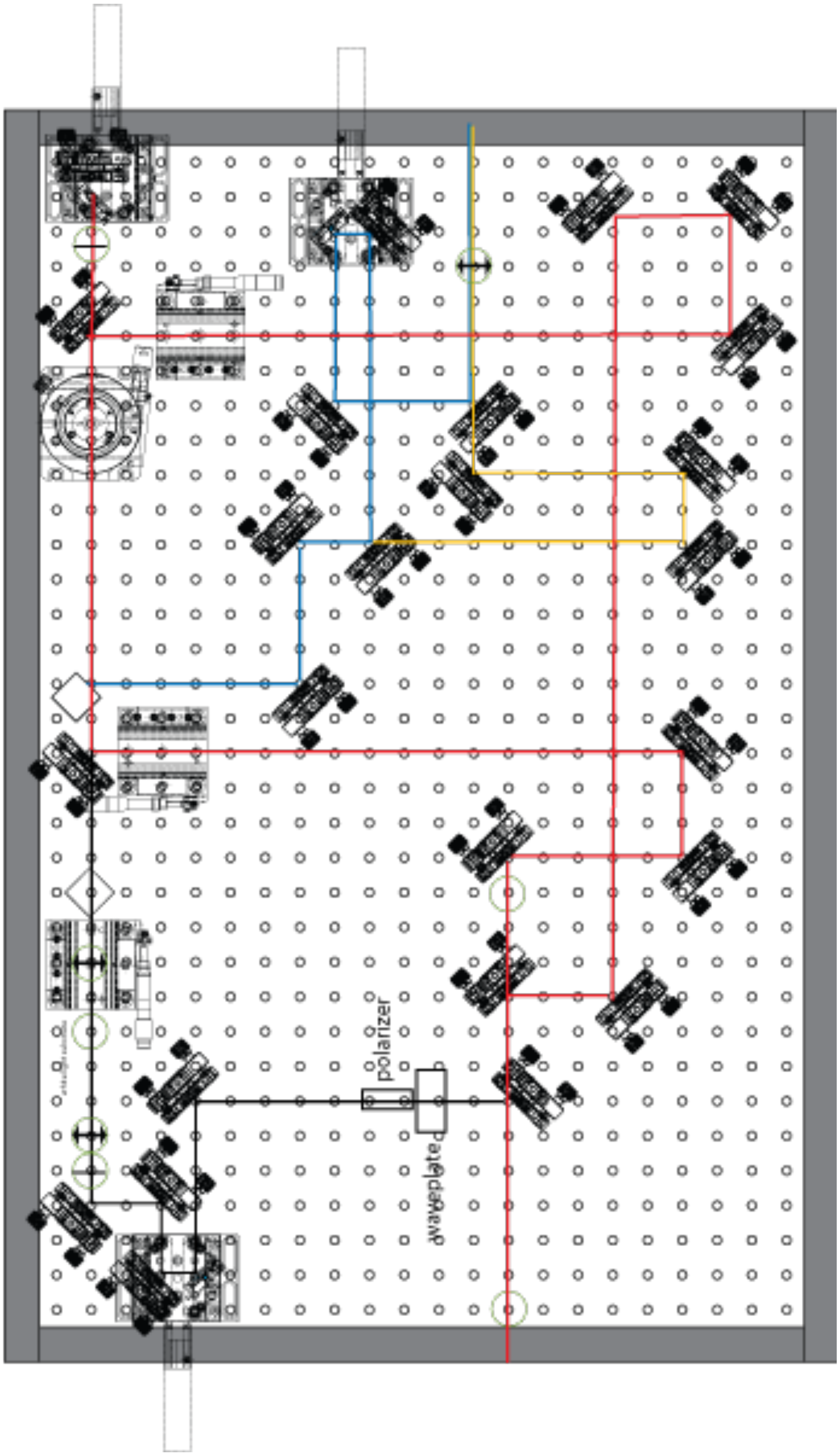

Figure A2: DFG Box Scale Drawing

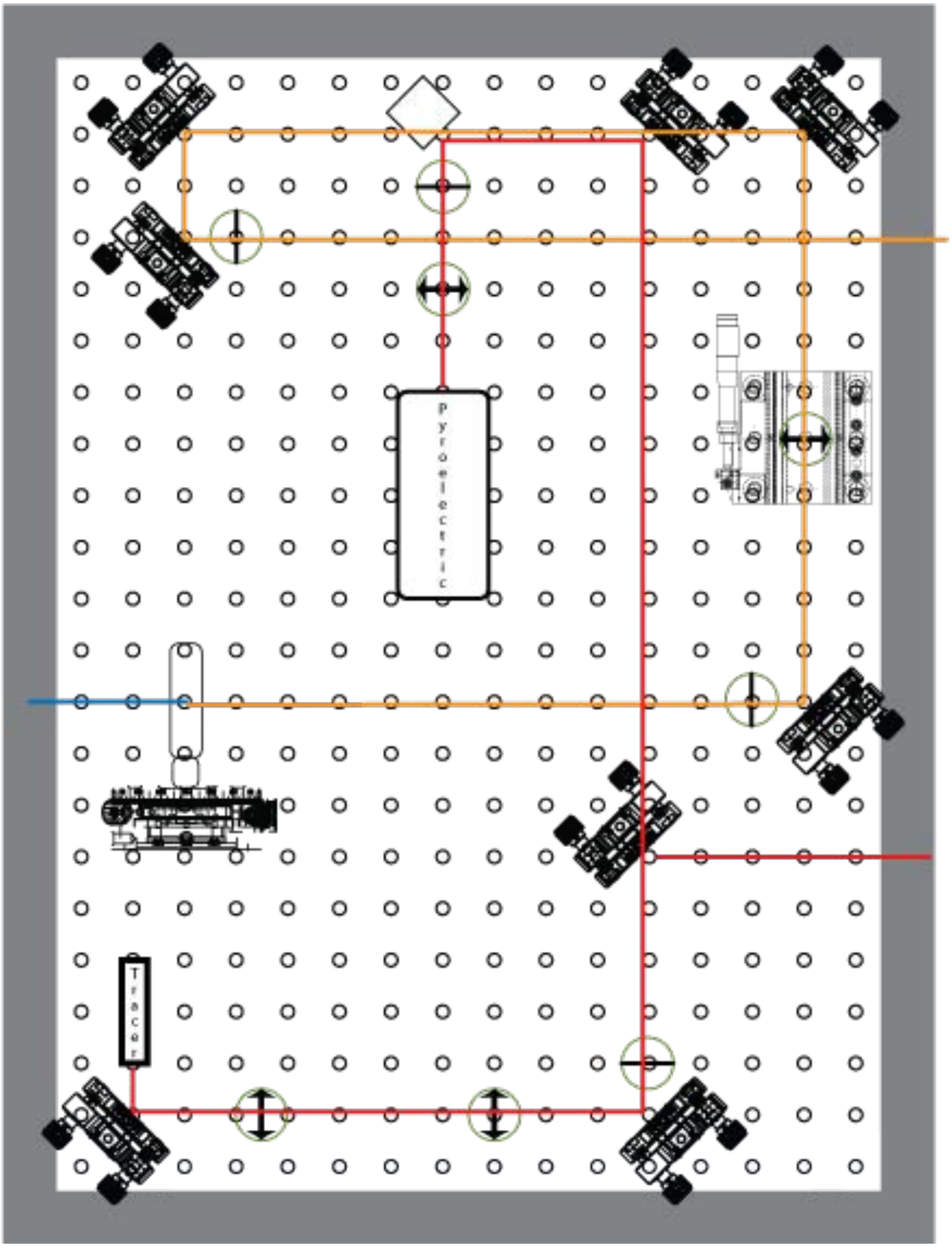

Figure A3: Pulse Shaper Box Scale Drawing

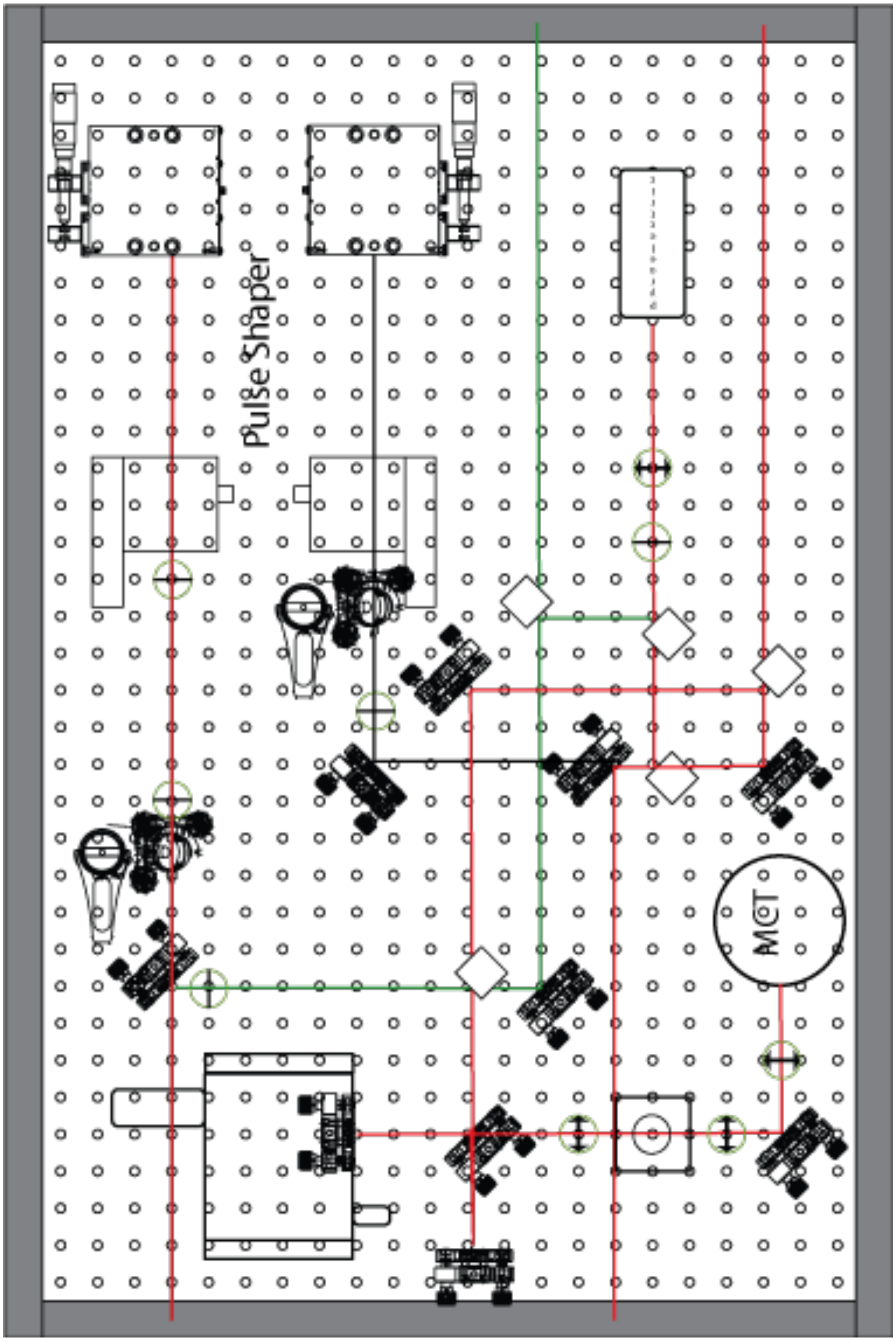

Figure A4: Upconversion Box Scale Drawing

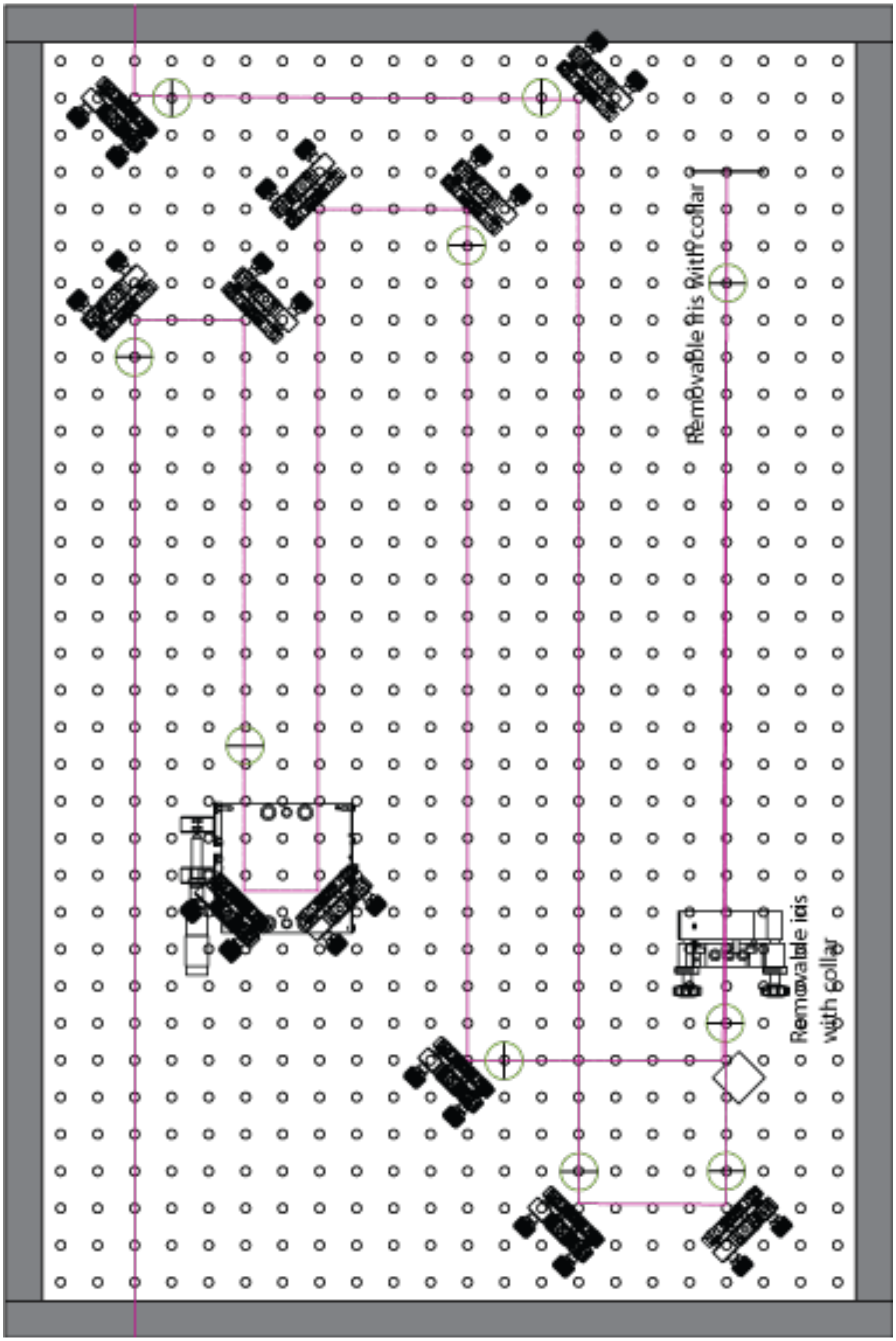

Figure A5: Sample Box Scale Drawing

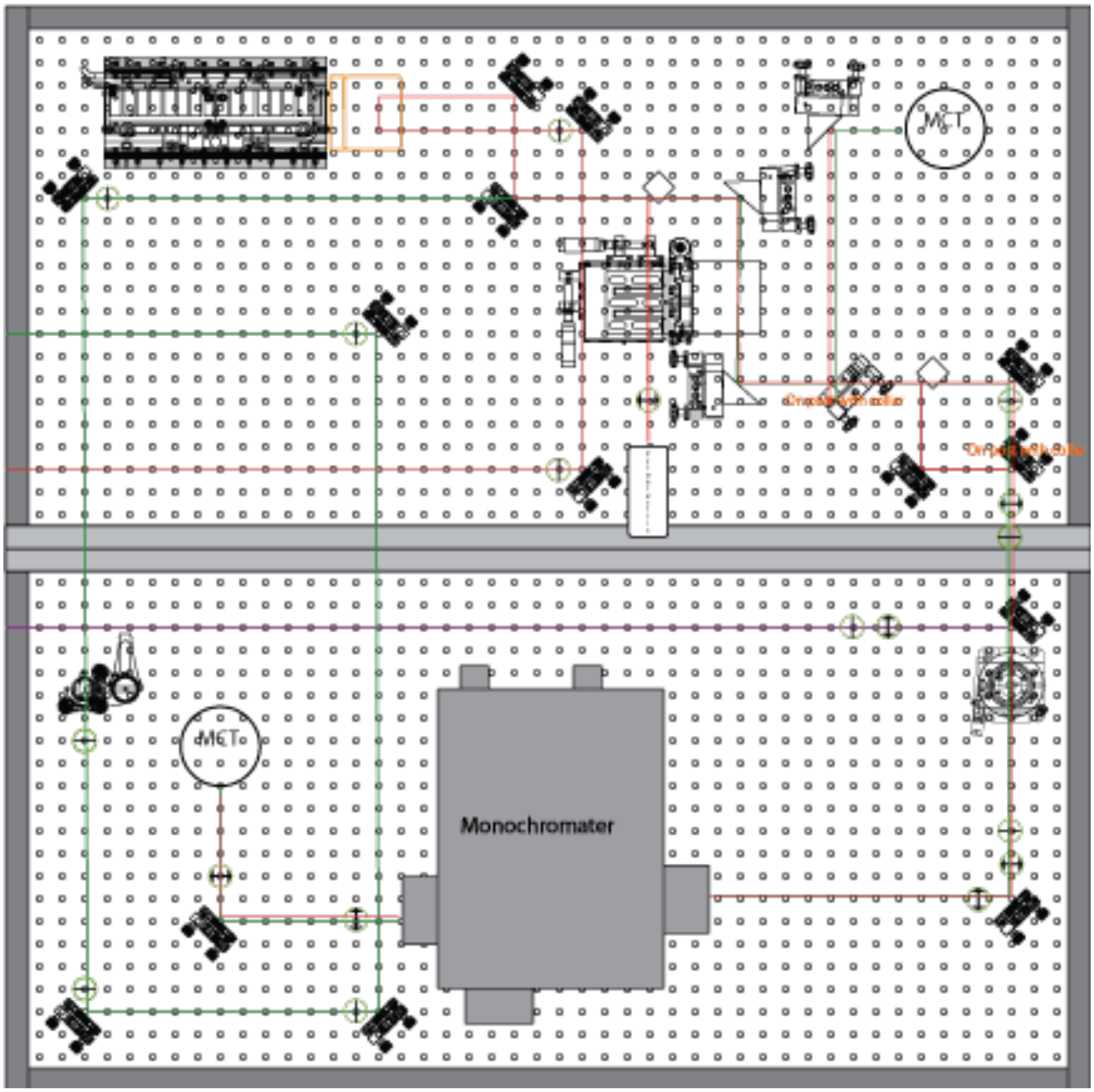

APPENDIX B: CUSTOM CODE OPERATION

Appendix B outlines operation of the custom computer code that controls the pulse shaping 2D IR spectrometer. All the hardware control necessary to align, calibrate, and collect data is integrated into one piece of code. This simplifies operation of the 2D IR spectrometer, and prevents the need to initialize and release hardware while switching between programs. All the custom code was developed using LabView. The code is written using the producer-consumer architecture provided by LabView; this architecture eliminates much of the overhead associated with event structures.

All the necessary functionality is impossible to fit onto one front panel. Therefore, 9 different popup front panels are accessible from the main front panel. Below are screen shots of the main front panel and all the available popups. A brief description its functionality is included with each popup.

Figure B1 shows the main front panel. There are large rectangular buttons on the far left of the front panel. All but three of these buttons access a popup. The three buttons that do not access a popup are: Generate Data Collection Masks, Load Data Collection Shapes, and Collect 2D Data.

The Generate Data Collection Masks button creates an array of pulse shapes with user-defined parameters. Start, End, Interval, Mask Length, Amplitude, and Shift Frequency are all adjustable controls on the front panel. Start, End, and Interval define the number of generated shapes, and Mask Length defines the length

Figure B1: The Main Front Panel

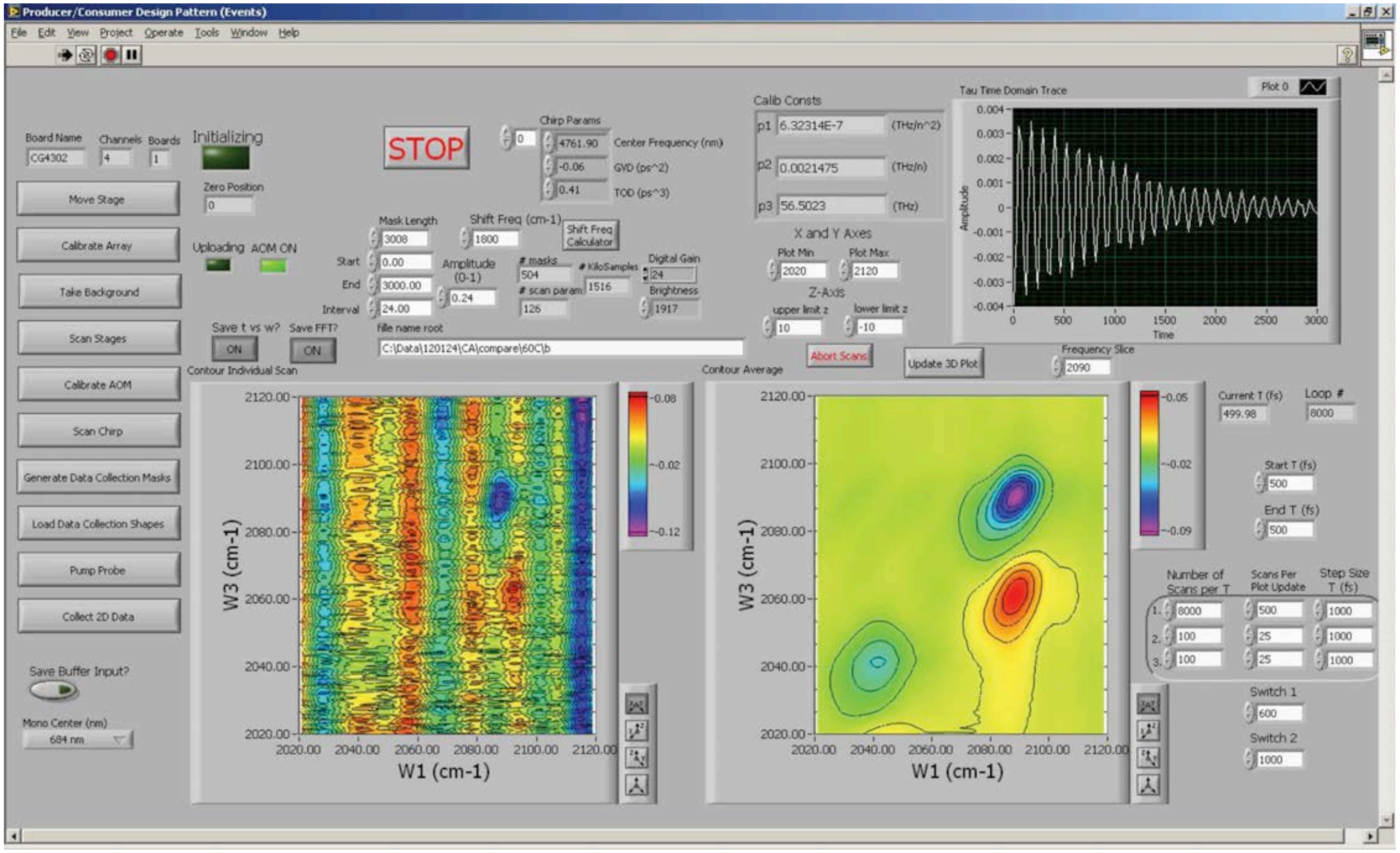

Board Name: CG4302
Channels: 4
Boards: 1
Zero Position: 0
Chirp Params: 0
Center Frequency (nm): 4761.90
GVD (ps^2): -0.06
TOD (ps^3): 0.41
Mask Length: 3008
Shift Freq (cm-1): 1800
Start: 0.00
End: 3000.00
Interval: 24.00
Amplitude (0-1): 0.24
masks: 504
scan param: 126
KiloSamples: 1516
Digital Gain: 24
Brightness: 1917
Save t vs w?: ON
Save FFT?: ON
file name root: C:\Data\120124\CA\compare\60C\b
p1: 6.32314E-7 (THz/n^2)
p2: 0.0021475 (THz/n)
p3: 56.5023 (THz)
Plot Min: 2020
Plot Max: 2120
upper limit z: 10
lower limit z: -10
Frequency Slice: 2090
Save Buffer Input?
Mono Center (nm): 684 nm
Current T (fs): 499.98
Loop #: 8000
Start T (fs): 500
End T (fs): 500

	Number of Scans per T	Scans Per Plot Update	Step Size T (fs)
1.	8000	500	1000
2.	100	25	1000
3.	100	25	1000

Switch 1: 600
Switch 2: 1000

of each pulse shape. A length of 3000 will fill the entire AOM. An error message will appear if the array size is too large for the AWG buffer. If this error occurs, decrease the number of shapes, or the length of each shape until the generated masks will fit in the buffer. The Generate Data Collection Masks button uses the latest calibration and chirp correction parameters. The current parameters appear in indicators on the front panel. The popups that control calibration and chirp correction are discussed later in this appendix.

The Load Data Collection Shapes button loads the generated masks into the AWG buffer. The green uploading indicator will illuminate while the shapes are loading. The uploading indicator will turn off and the AOM On indicator will illuminate when the shapes are loaded. Loading shapes requires a lot of computing power. Do not press other buttons on the front panel while shapes are loading; this can cause the code to freeze or crash.

The Collect 2D Data button begins 2D data collection. Several front panel controls select the data collection parameters, including the display parameters for the graphs on the front panel. There are three plots on the main front panel, two contour plots, and a xy graph. The left contour plot shows the 2D IR spectrum of a single scan, and the right plot shows the latest average. The display range for the contour plots is set with the plot min and plot max controls on the front panel. The xy graph displays a time domain slice of the τ_1 axis of the 2D data. The frequency slice control below the xy graph selects the ω_3 frequency slice displayed.

The controls to the right of the contour plots provide further control of the 2D data collection parameters. There are 13 controls and 2 indicators to the right of the contour plots. The indicators at the top display the current waiting time, and current number of averages collected. The top two controls set the start and end times for the waiting time (T). The 3x3 block of controls sets the T interval, the number of averages per 2D IR spectrum, and the number of averages per contour plot update. It is often useful increase the number of averages per 2D spectrum, and the T interval between 2D spectra at long waiting times. The signal decreases at long waiting times, so increased averaging can recover the S/N. The relevant chemical dynamics are often significantly slower at long waiting times, so the spacing between data points can be larger. The first column in the 3x3 control block sets the number of averages per spectrum, the second column sets the number of averages per contour plot update, and the third column sets the T interval between spectra. The first row sets the three parameters at the beginning of data collection, the second row sets the parameters between the first and second switch times, and the third row sets the parameters after the second switch time. The bottom two controls are the switch times. The switch times define the waiting time after which the data collection code uses the next set of parameters.

Generating contour plots requires a lot of computing time. Therefore, the contour plots do not update with every scan. The Scans Per Plot Update control sets the number of averages between contour plot updates. When saving is enabled, the code will save the current average at every plot update. This guards against losing all data if an unexpected error happens in the middle of a long scan (sample evaporation, laser error, code crash, etc.). Figure B2 shows an example of possible data collection parameters.

Figure B2: 2D Data Collection Parameters Example

Start T (fs)
0
End T (fs)
20000

	Number of Scans Per T	Number of Scans Per Plot Update	Step Size T (fs)
1.	100	50	50
2.	1000	500	500
3.	5000	2500	1000

Switch 1
5000
Switch 2
10000

An example of reasonable scan parameters that will collect a complete 2D IR data set. These parameters will collect 121 2D IR spectra. Between T=0 and T=5 ps, the code will collect a 2D IR spectrum every 50 fs (100 spectra). Between T=5000 and T=10000, the code will collect a 2D IR spectrum every 500 fs (10 spectra), and after 10 ps, the code will collect a 2D IR spectrum every 1ps (10 spectra).

The parameters shown in figure B2 will collect 121 2D IR spectra. The code will collect a 2D IR spectrum every 50 fs between T=0 ps and T=5 ps (101 spectra). Each of these spectra will be the average of 100 scans. The code will update the displayed contour and save the current average every 50 scans. The code will save 3 spectra at each T time, the spectrum after 1 average, the spectrum after 50 averages, and the spectrum after 100 averages. The code will collect a 2D IR spectrum every 500 fs between T=5 ps and T=10 ps (10 spectra). Each spectra will be the average of 1000 scans; the code will update the contour plots and save every 500 fs, and save 3 spectra per T. After T=10ps, the code will collect a 2D IR spectrum every 1000 fs (10 spectra). Each spectrum will be the average of 5000 scans, and the code will update and save every 2500 scans.

The top rectangular button on the front panel is the Move Stages button; it will cause the Move Stages popup to appear. Figure B3 shows the move stages popup. The Move Stages popup allows the user to move the translation stages to any position, and change the zero position of each stage. This popup is generally only used when the user knows the desired stage position. Pressing the red STOP button at the top will close the popup.

The next rectangular button, Calibrate Array, initiates the Array Calibration sequence. This sequence contains 3 popups. The first popup is the Baseline Correction popup. This popup collects a baseline to correct the sloping background the array produces. The next rectangular button, Take Background, calls the Baseline Correction popup without initiating the rest of the Array Calibration sequence. Figure B4 shows the baseline correction popup.

Figure B3: Move Stages Popup

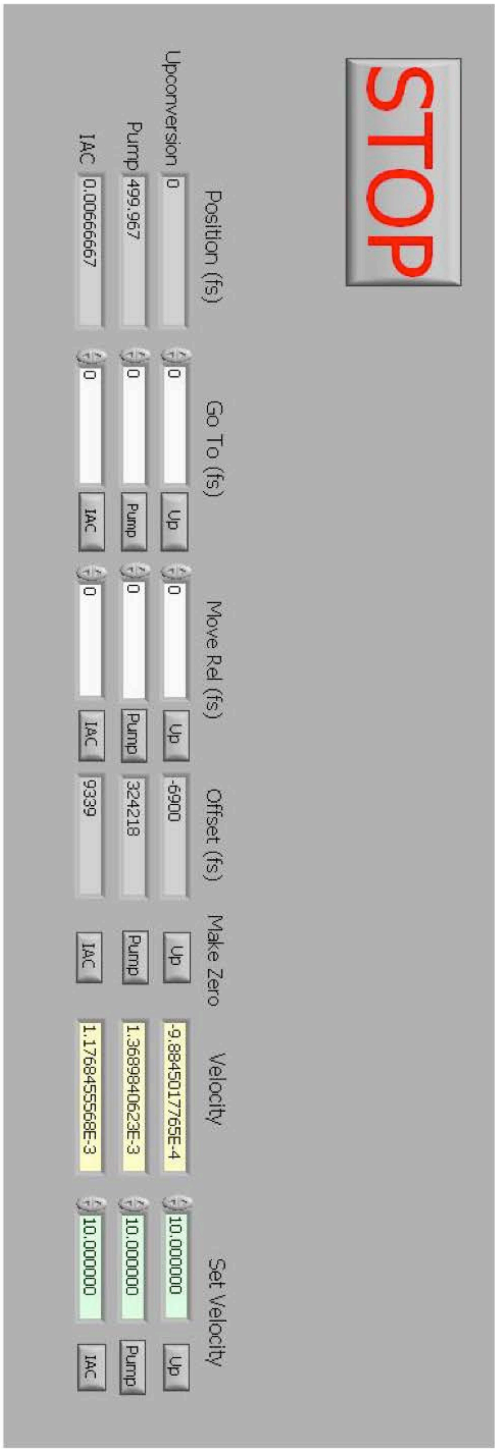

	Position (fs)	Go To (fs)	Move Rel (fs)	Offset (fs)	Make Zero	Velocity	Set Velocity
Upconversion	0	0	0	-6900		-9.8845017765E-4	10.000000
Pump	499.967	0	0	324218		1.3689840623E-3	10.000000
IAC	0.00666667	0	0	9339		1.1768455568E-3	10.000000

Figure B4: Baseline Correction Popup

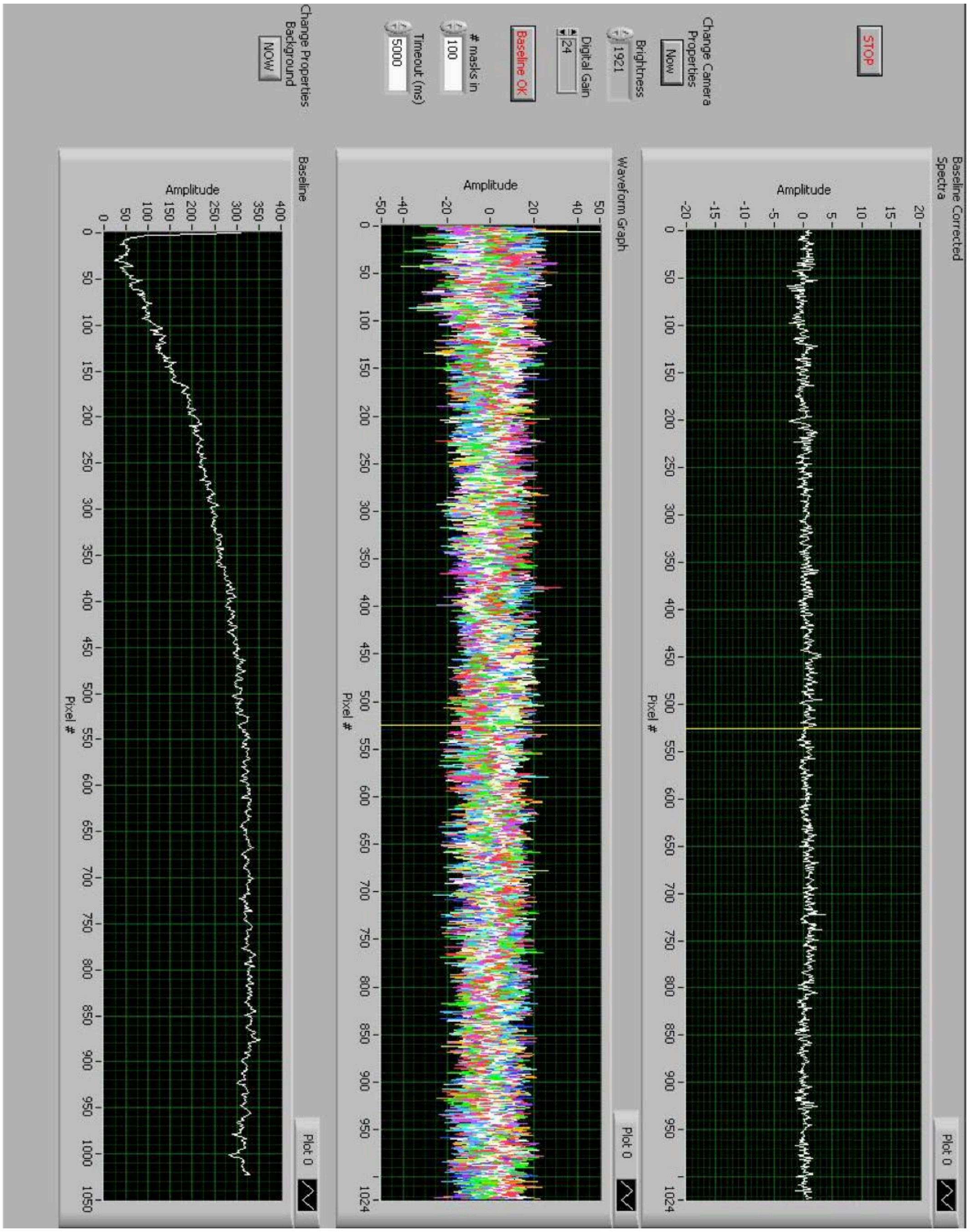

Brightness 1921

Digital Gain 24

masks in 100

Timeout (ms) 5000

The baseline correction popup has 3 xy graphs. The bottom graph shows the uncorrected baseline. When the popup initiates, this is the only graph that is updating. The brightness level can be set to an optimum value while observing the uncorrected baseline. The brightness should be set to a level that raises the baseline over the detection limit for all pixels. However, if the baseline is set too high, dynamic range will be lost. Controls to the left of the graphs can change the brightness and digital gain. The Change Properties Background button must be pressed to update the camera properties.

The displayed baseline is the average of several scans. The # masks control sets the number of averaged scans. After the baseline looks appropriate, press the red Baseline Ok button. This will stop collection of baseline spectra, and display baseline corrected spectra. The middle graph shows every individual scan, and the top graph shows the average of all the scans. Pressing the red STOP button at the top will close the popup.

The next popup in the Array Calibration sequence measures the spectrum of the 800 nm upconversion pulse. The code automatically turns the grating to 800 nm. The 800 nm pulse is very intense, and will likely saturate the array, so a neutral density filter should be inserted in the beam before allowing the 800nm radiation to illuminate the array. Adjust the neutral density to achieve an appropriate signal level on the array. Then, the code will automatically find the peak position of the 800 nm spectrum. Pressing the STOP button at the top will close the popup and automatically save the peak position. Figure B5 shows the Measure Upconversion Position popup.

Figure B5: Measure Upconversion Position Popup

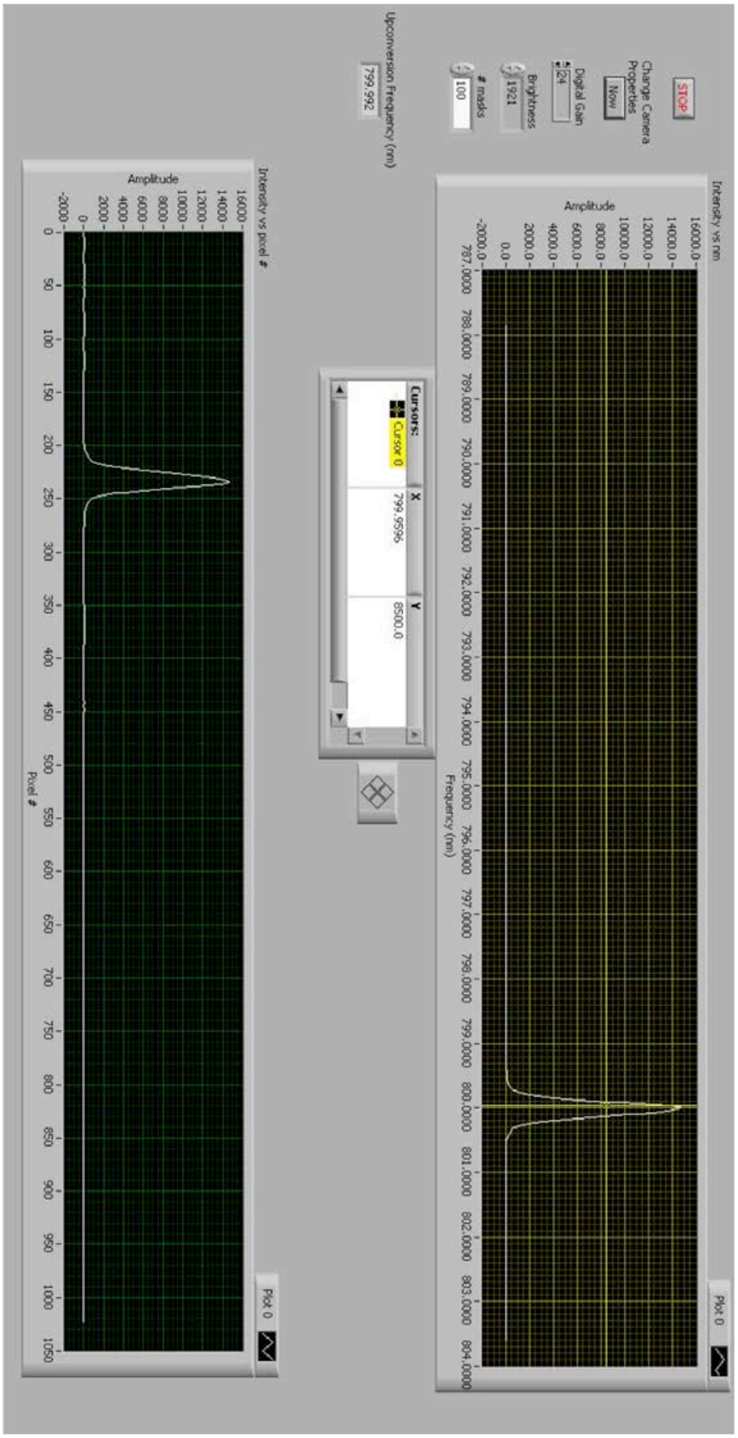

Digital Gain 24

Brightness 1921

masks 100

Upconversion Frequency (nm) 799.992

Cursors:	X	Y
Cursor 0	799.9596	8500.0

The final popup in the Array Calibration sequence is the Calibrate Array popup. This popup allows the user to perform a 3 point calibration of the array at the current grating position. The array calibration changes as the spectrometer rotates the grating. Therefore, each grating position requires its own calibration to ensure accurate data collection. The code has calibrations saved for every grating position that has been used to date, however, it is possible that more calibrations will be needed in the future. The top 6 controls allow the user to input the central frequency of three transitions (measured with the FTIR), and the pixel number at which each transition is found. The top graph displays intensity vs frequency (nm), the middle graph displays intensity vs frequency (cm^{-1}), and the bottom graph displays intensity vs pixel number. The top two graphs use a previously saved calibration to create the frequency axis, so they will only provide approximate peak positions. After the peak positions in pixel number and wavenumber are entered, pressing the Calibrate button at the top will fit the entered parameters to a 2nd order polynomial, and save the fit parameters. The fit parameters can be used to generate the frequency at each pixel. The saved calibration must be manually inserted into the code. Pressing the red STOP button at the top closes the popup. The Array Calibration sequence is normally used to measure the central frequency of the upconversion light, and the final popup is usually ignored. Figure B6 shows the array calibration popup.

Figure B6: Array Calibration Popup

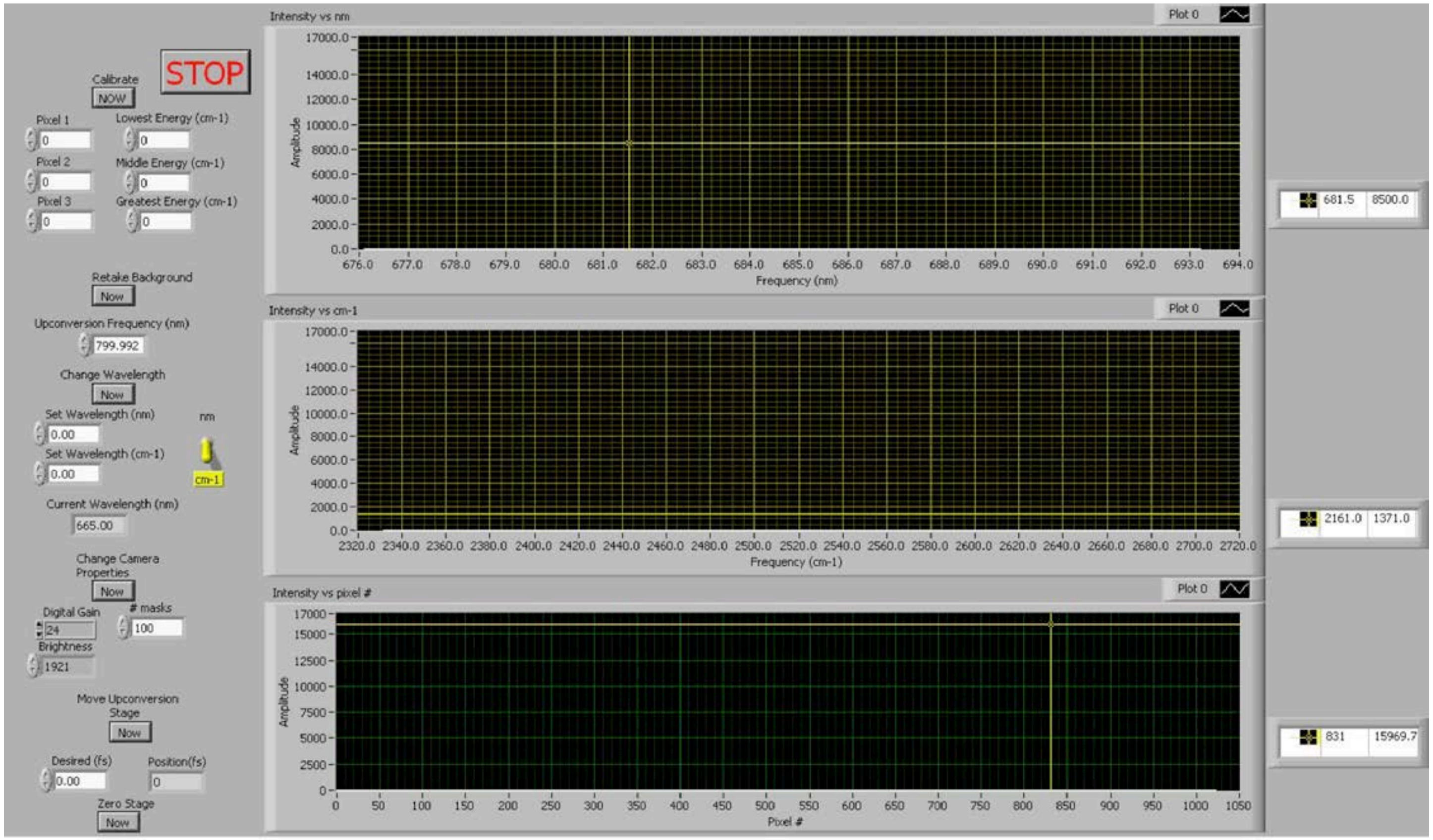

Pixel 1: 0
Pixel 2: 0
Pixel 3: 0
Lowest Energy (cm-1): 0
Middle Energy (cm-1): 0
Greatest Energy (cm-1): 0
Upconversion Frequency (nm): 799.992
Set Wavelength (nm): 0.00
Set Wavelength (cm-1): 0.00
Current Wavelength (nm): 665.00
Digital Gain: 24
masks: 100
Brightness: 1921
Desired (fs): 0.00
Position(fs): 0

The next rectangular button, Scan Stages, initiates the Scan Stages popup. If the AOM is off, this code will create pulse shapes with no phase corrections, and send them to the AOM. If the AOM is on, this popup uses the saved AOM Calibration and Chirp Correction constants to produce a $\tau=0$ pulse shape. This will produce a single pump pulse with all the necessary phase corrections. This is important because phase corrections will cause a shift in the time delay of the pump pulse. The scan stages code allows the user to scan any of the three stages while observing the appropriate detector. In the scan stages popup, the user can measure the autocorrelation of the pump or probe pulses in the interferometric autocorrelator (IAC). The user can also measure the cross correlation between the pump and probe pulses by scanning the pump stage (labeled T), while observing the doubled light created by crossing the beams in a $AgGaS_2$ crystal at the sample position. The controls at the bottom of the code allow the user to move the stages to an arbitrary position, and change the saved time zeros for each stage. There is not currently an appropriate detector to measure the integrated intensity of the upconversion signal installed on the table. Therefore, the upconversion position is usually set in the AOM calibration code while observing the array intensity. Figure B7 shows the Scan Stages popup.

The next rectangular button, Calibrate AOM, initiates the AOM Calibration popup. This popup allows the user to measure comb and hole spectra to create a calibration curve for the AOM as discussed in section 2.14. Figure B8 shows the AOM Calibration popup.

Figure B7: Scan Stages Popup

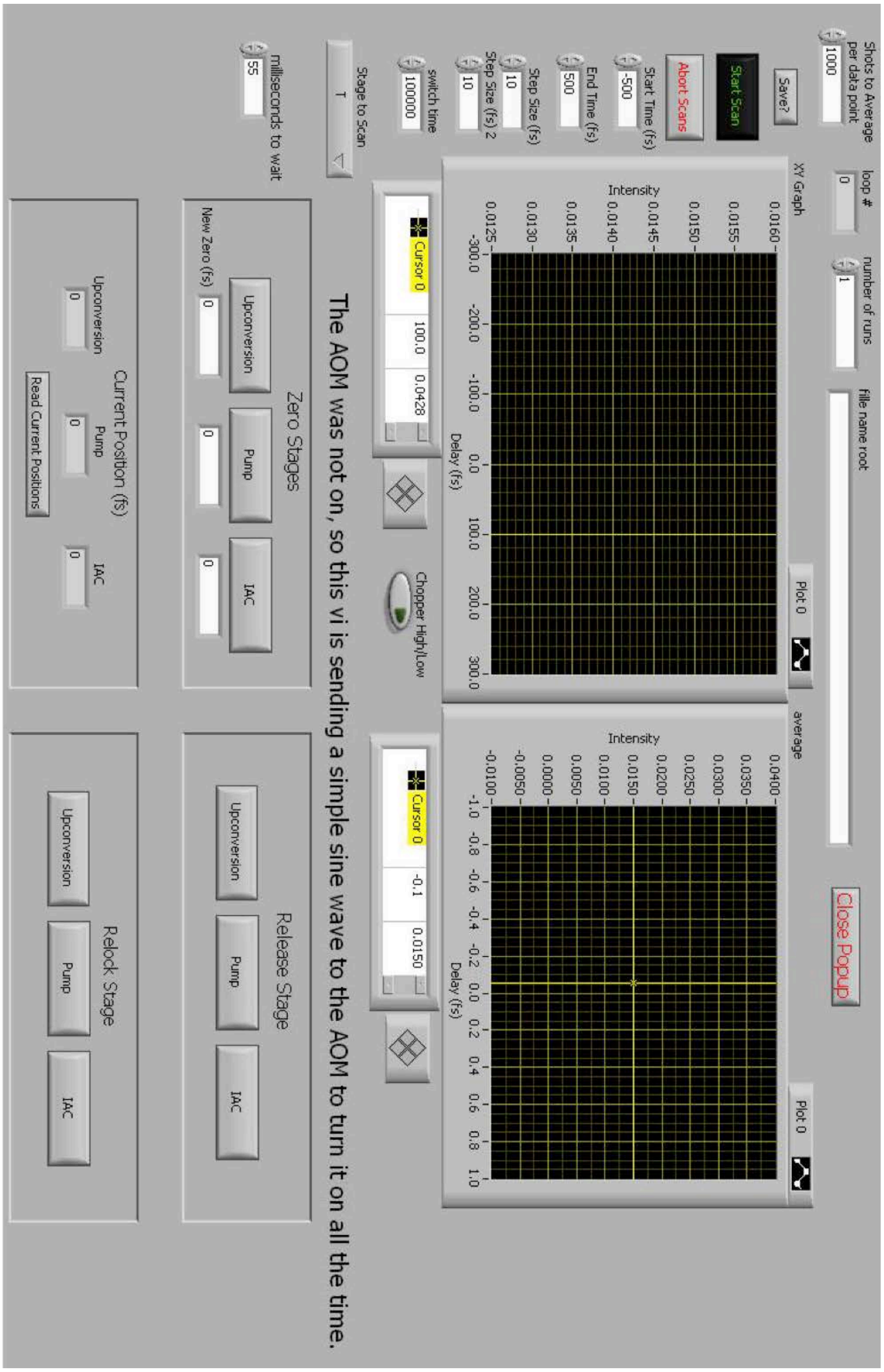

Shots to Average per data point: 1000

loop #: 0

number of runs: 1

file name root:

Start Time (fs): -500

End Time (fs): 500

Step Size (fs): 10

Step Size (fs) 2: 10

switch time: 100000

Stage to Scan: T

milliseconds to wait: 55

Cursor 0: 100.0, 0.0428

Cursor 0: -0.1, 0.0150

The AOM was not on, so this vi is sending a simple sine wave to the AOM to turn it on all the time.

Zero Stages — New Zero (fs): Upconversion 0, Pump 0, IAC 0

Current Position (fs): Upconversion 0, Pump 0, IAC 0

Figure B8: AOM Calibration Popup

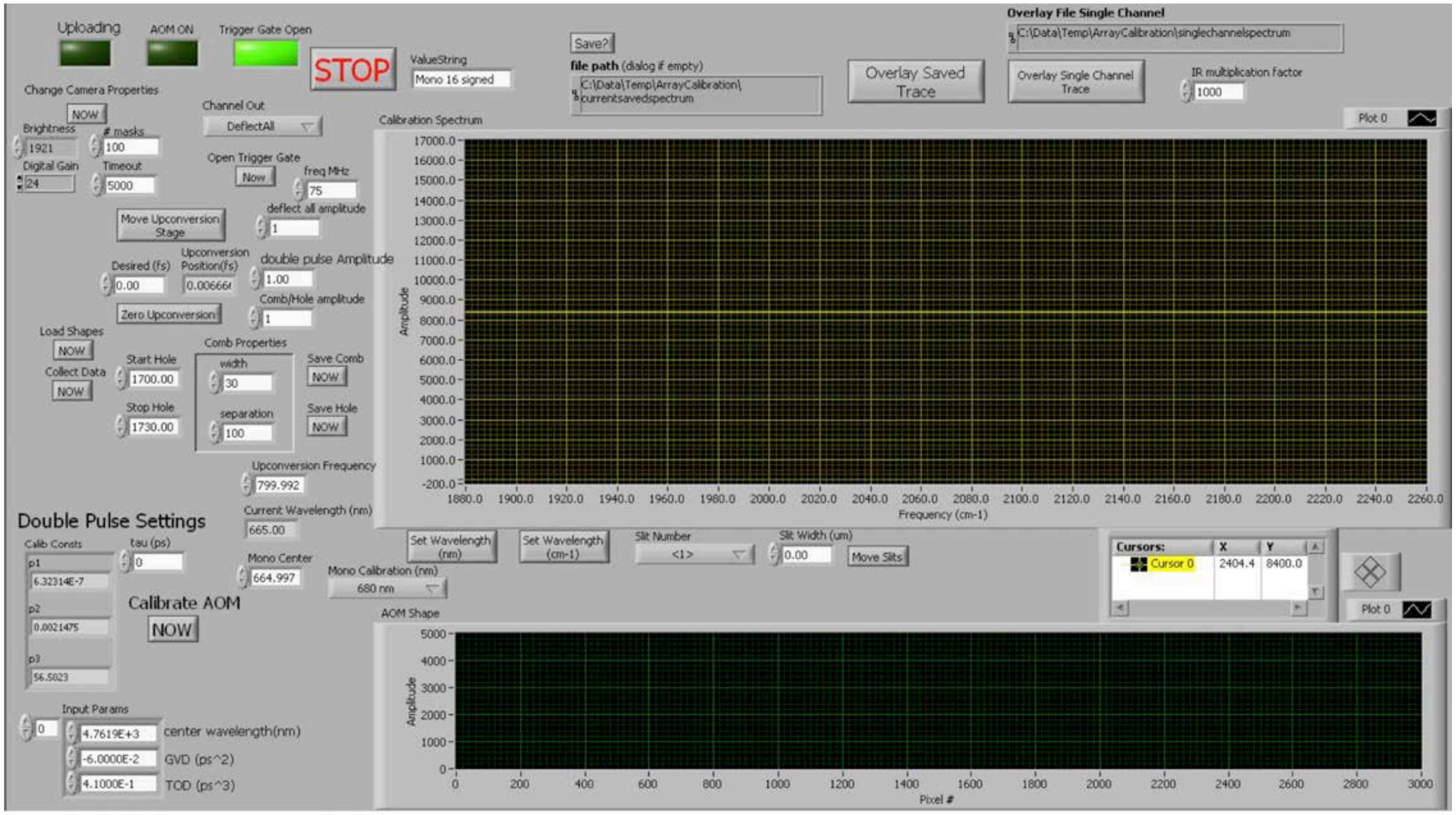

Brightness: 1921
\# masks: 100
Digital Gain: 24
Timeout: 5000
Channel Out: DeflectAll
freq MHz: 75
deflect all amplitude: 1
Desired (fs): 0.00
Upconversion Position(fs): 0.00666
double pulse Amplitude: 1.00
Comb/Hole amplitude: 1
Start Hole: 1700.00
Stop Hole: 1730.00
Comb Properties: width: 30; separation: 100
Upconversion Frequency: 799.992
Current Wavelength (nm): 665.00
Mono Center: 664.997
Mono Calibration (nm): 680 nm
ValueString: Mono 16 signed
file path (dialog if empty): C:\Data\Temp\ArrayCalibration\currentsavedspectrum
Overlay File Single Channel: C:\Data\Temp\ArrayCalibration\singlechannelspectrum
IR multiplication factor: 1000
Slit Number: <1>
Slit Width (um): 0.00

Double Pulse Settings

Calib Consts
p1: 6.32314E-7
p2: 0.0021475
p3: 56.5023
tau (ps): 0

Input Params: 0
center wavelength(nm): 4.7619E+3
GVD (ps^2): -6.0000E-2
TOD (ps^3): 4.1000E-1

Cursors:
	X	Y
Cursor 0	2404.4	8400.0

In the AOM Calibration popup, the user can move the upconversation stage position and observe the resultant spectral intensity. This is usually how the upconversion stage position is set. The user can also observe the comb, hole, and deflect all spectra by changing the selection in the dropdown menu at the top of the popup. This changes the channel from the AWG that is sent to the AOM. To calibrate the AOM, the user needs to save a comb and hole spectrum by pressing the Save Comb, or Save Hole button when the appropriate spectrum is displayed. Pressing the Calibrate button will open the Calibration popup. The Calibration popup will automatically generate the AOM calibration from the saved comb and hole spectra. The graph in the Calibration popup displays the comb spectrum in white, the hole spectrum in red, and creates a green line everywhere it found a peak in the comb spectrum. If the Calibration code finds too many peaks, the threshold can be adjusted in the popup. Figure B9 shows the Calibration popup.

The next rectangular button, Scan Chirp, initiates the Scan Chirp popup. The Scan Chirp popup loads pulse shapes into the AOM buffer with incremented second and third order dispersion values. The popup scans the second and third order dispersion, and displays a contour map of GVD (group velocity dispersion) vs TOD (third-order dispersion) where the contour levels are the measured doubled light intensity. The output of the pump light must be sent to the IAC to measure the double intensity. One of the arms in the IAC should be blocked to avoid intensity variations due to interference. The user should then find the GVD and TOD value that maximizes the doubled light. These values should be input into the GVD and

TOD controls. Then, when the user closes the popup, these values are automatically saved as the current chirp paramters. Figure B10 shows the Scan Chirp popup.

The second rectangular grey button from the bottom, Pump Probe, opens the Pump Probe popup. When the user presses this button, a dialog popup appears that allows the user to select Display or Scan Pump Probe. The Display Pump Probe popup allows the user to optimize the system while monitoring the dispersed pump probe signal. Figure B11 shows the Display Pump Probe popup. The Scan Pump Probe popup allows the user to measure and save dispersed pump probe spectra. Figure B12 shows the Scan Pump Probe popup.

The last popup accessible from the front panel is the Shift Frequency Calculator. The grey button to the right of the Shift Frequency control initiates this popup. This popup calculates the spectral range accessible with a given shift frequency. The shift frequency value is the lower limit of the spectral range, and the calculator displays the upper limit. The entire lineshape of interest should fall within the accessible spectral range. Figure B13 shows the Shift Frequency popup.

Figure B9: Calibration Popup

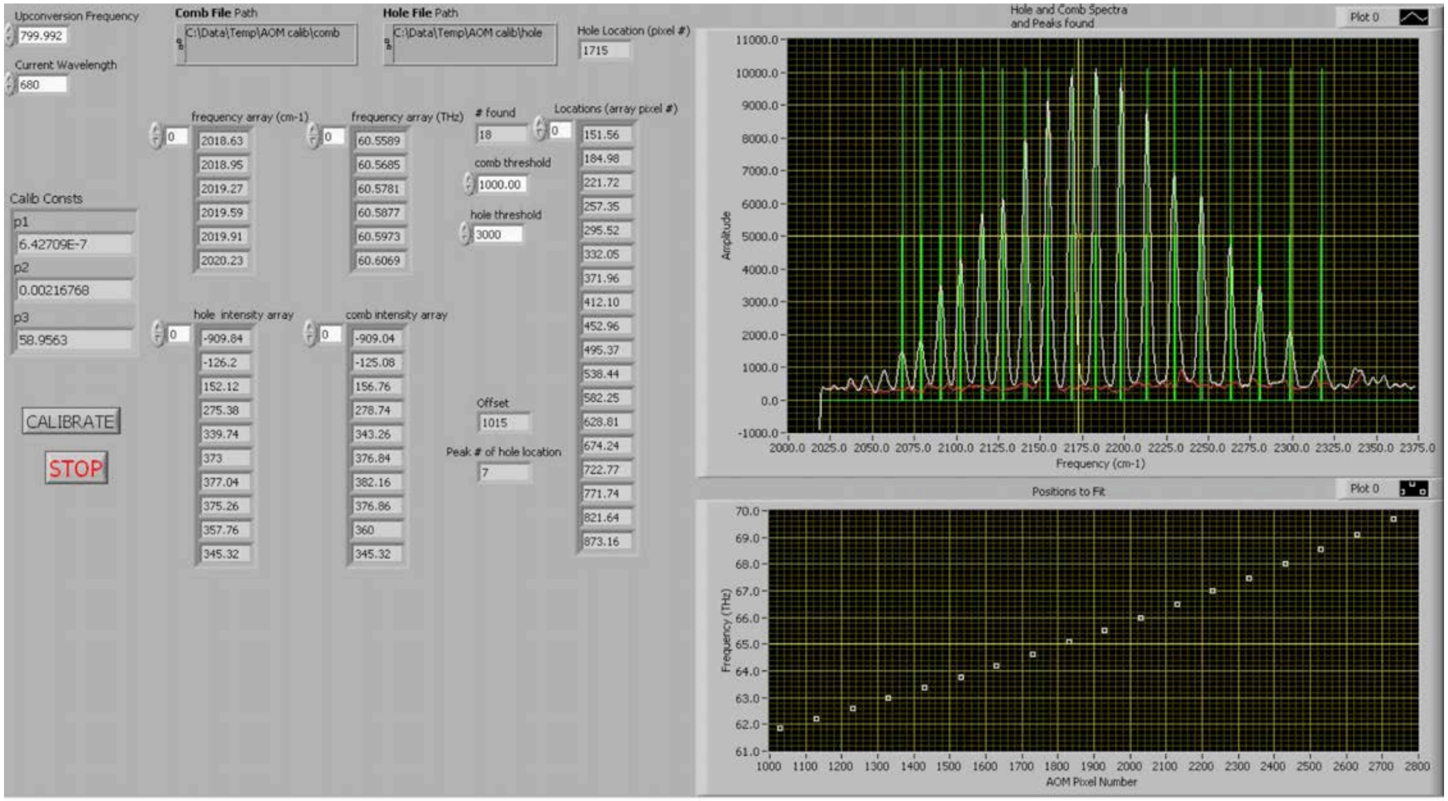

Upconversion Frequency: 799.992

Current Wavelength: 680

Comb File Path: C:\Data\Temp\AOM calib\comb

Hole File Path: C:\Data\Temp\AOM calib\hole

Hole Location (pixel #): 1715

Calib Consts

p1: 6.42709E-7

p2: 0.00216768

p3: 58.9563

found: 18

comb threshold: 1000.00

hole threshold: 3000

Offset: 1015

Peak # of hole location: 7

frequency array (cm-1)	frequency array (THz)	Locations (array pixel #)
2018.63	60.5589	151.56
2018.95	60.5685	184.98
2019.27	60.5781	221.72
2019.59	60.5877	257.35
2019.91	60.5973	295.52
2020.23	60.6069	332.05
		371.96
		412.10
		452.96
		495.37
		538.44
		582.25
		628.81
		674.24
		722.77
		771.74
		821.64
		873.16

hole intensity array	comb intensity array
-909.84	-909.04
-126.2	-125.08
152.12	156.76
275.38	278.74
339.74	343.26
373	376.84
377.04	382.16
375.26	376.86
357.76	360
345.32	345.32

Figure B10: Scan Chirp Popup

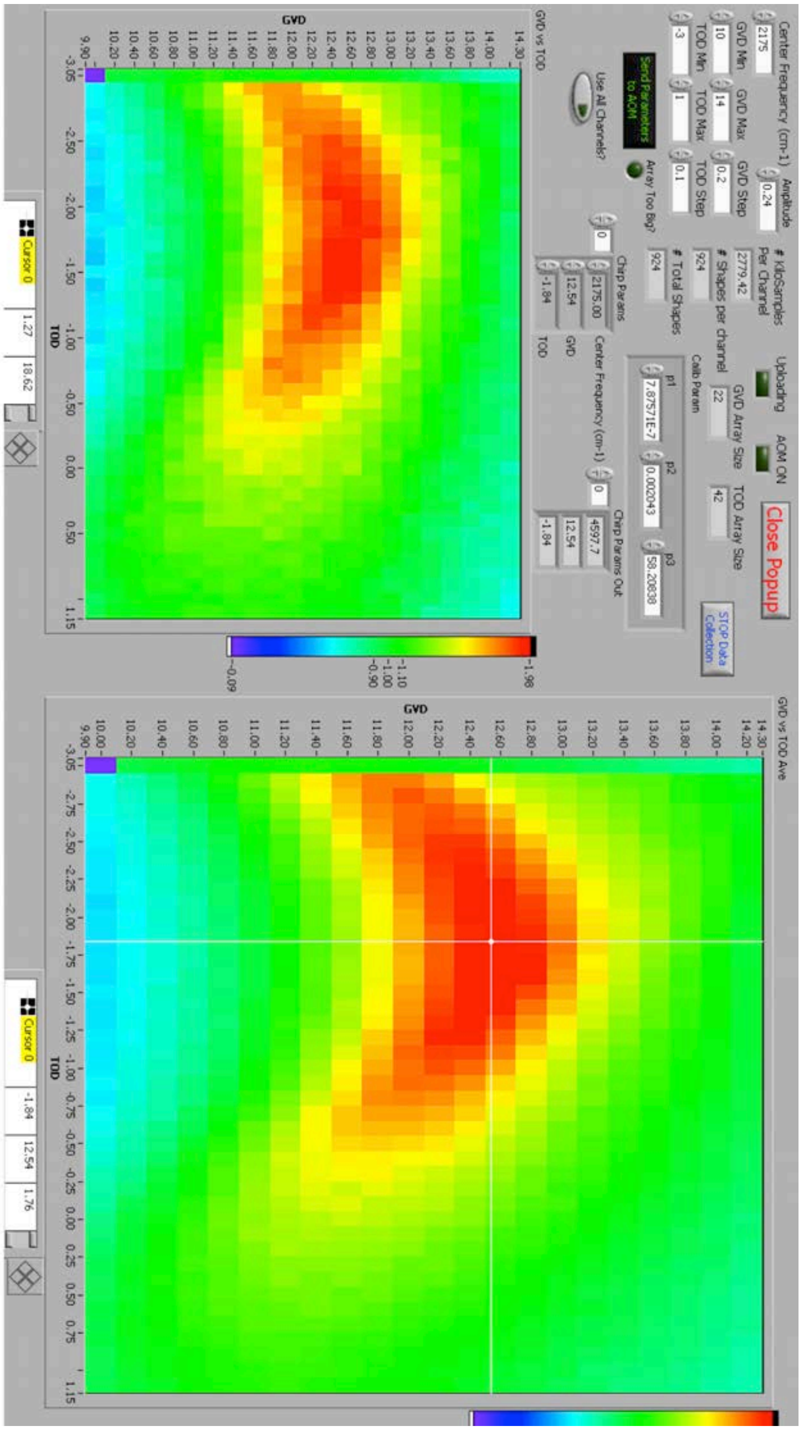

Center Frequency (cm-1) 2175
Amplitude 0.24
GVD Min 10
GVD Max 14
GVD Step 0.2
TOD Min -3
TOD Max 1
TOD Step 0.1
KiloSamples Per Channel 2779.42
Shapes per channel 924
Total Shapes 924
GVD Array Size 22
TOD Array Size 42
Array Too Big?
Use All Channels?
Chirp Params 0
Center Frequency (cm-1) 2175.00
GVD 12.54
TOD -1.84
Chirp Params Out 0
4597.7
12.54
-1.84
Calib Param
p1 7.87571E-7
p2 0.0020043
p3 58.20838

Figure B11: Display Pump Probe Popup

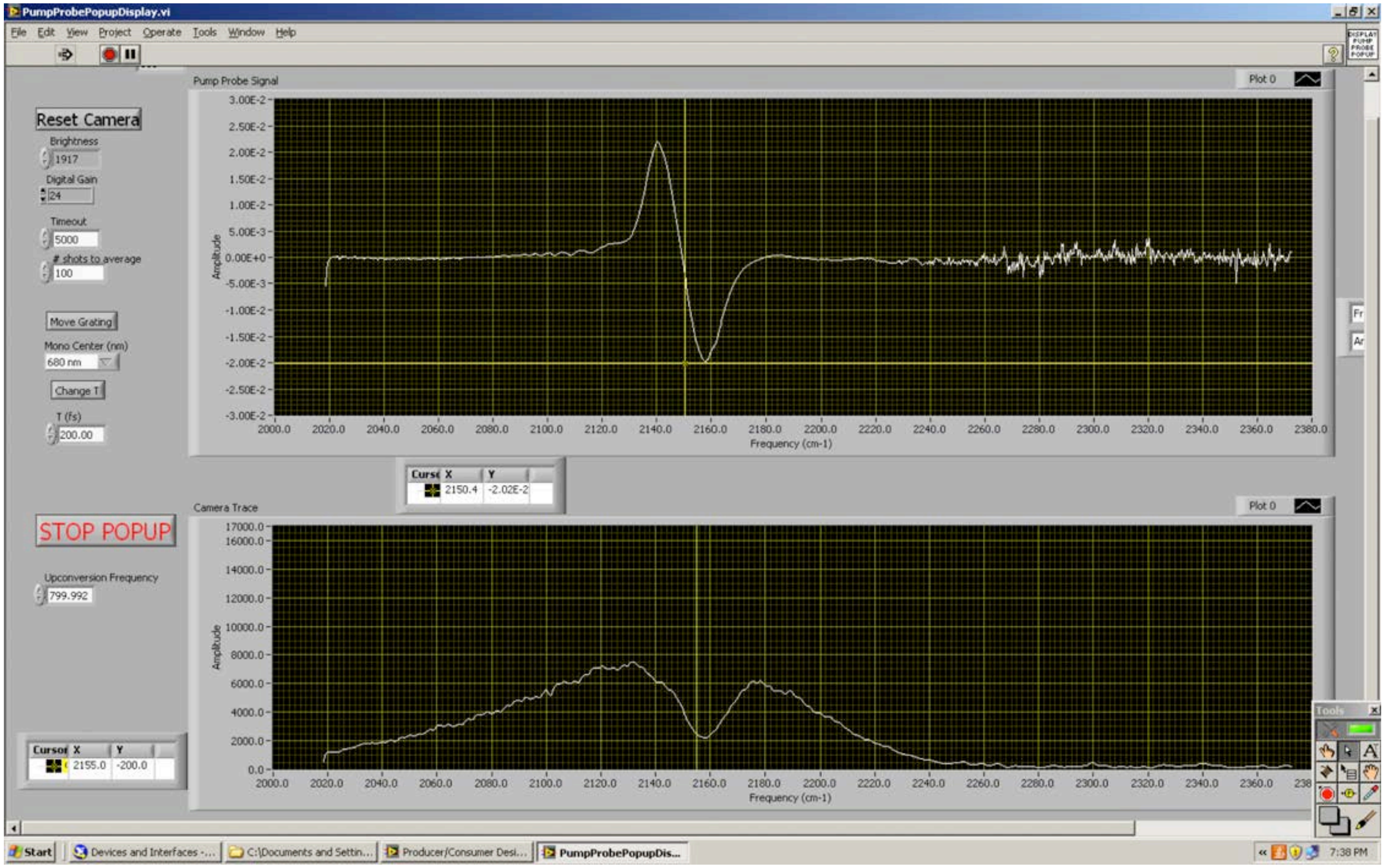

Brightness 1917

Digital Gain 24

Timeout 5000

shots to average 100

Mono Center (nm) 680 nm

T (fs) 200.00

Upconversion Frequency 799.992

Cursor	X	Y
	2150.4	-2.02E-2

Cursor	X	Y
	2155.0	-200.0

Figure B12: Scan Pump Probe Popup

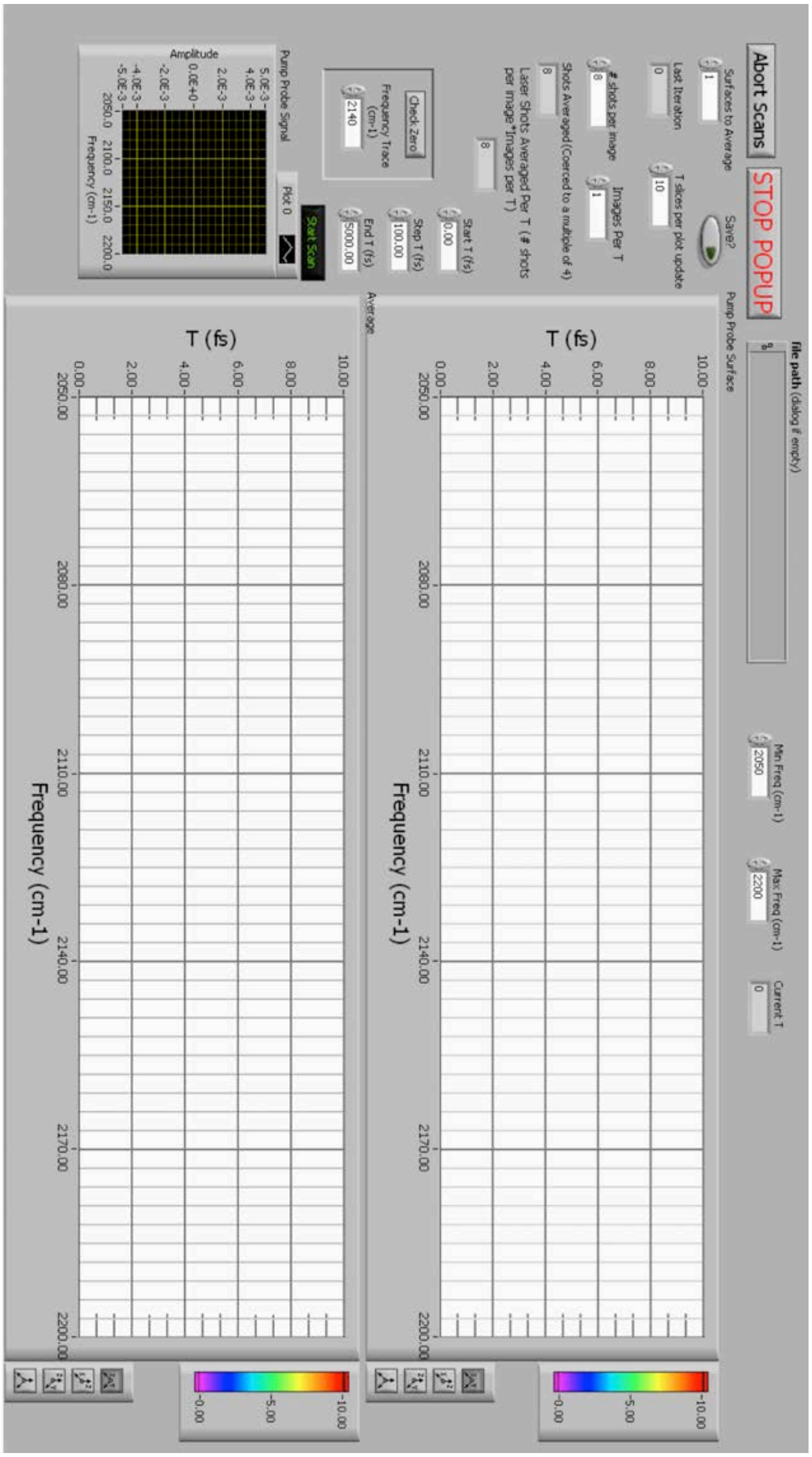

Surfaces to Average: 1
Last Iteration: 0
T slices per plot update: 10
shots per image: 8
Images Per T: 1
Shots Averaged (Coerced to a multiple of 4): 8
Laser Shots Averaged Per T (# shots per image*Images per T): 8
Start T (fs): 0.00
Step T (fs): 100.00
End T (fs): 5000.00
Frequency Trace (cm-1): 2140
Min Freq (cm-1): 2050
Max Freq (cm-1): 2200
Current T: 0

Figure B13: Shift Frequency Calculator

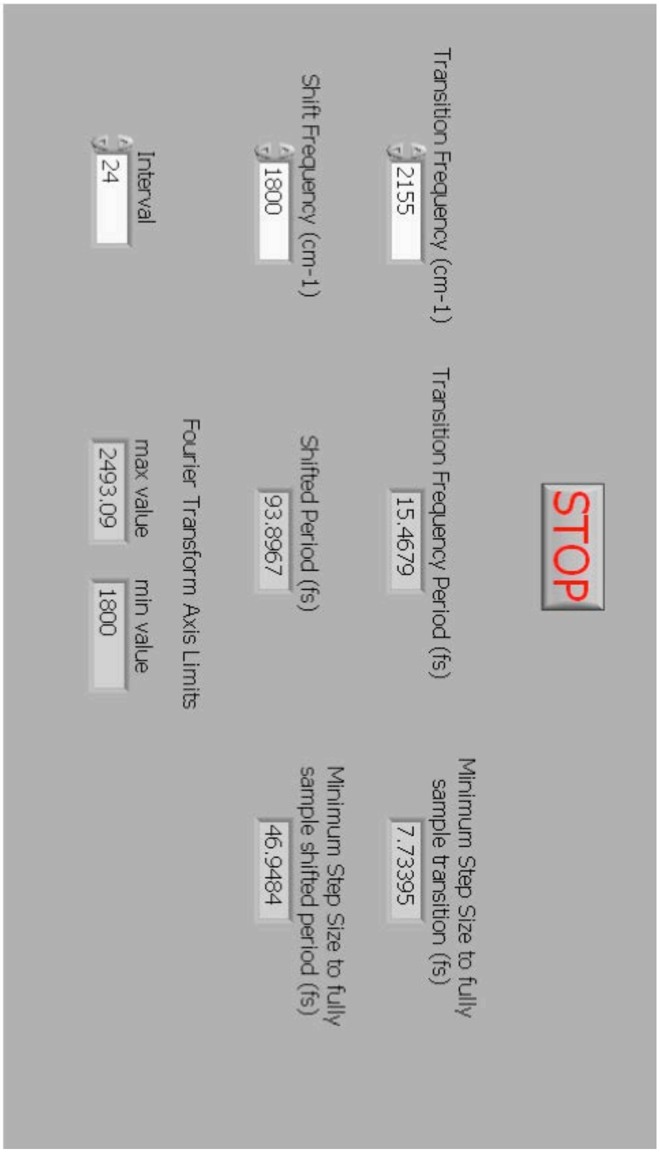

Transition Frequency (cm-1): 2155

Transition Frequency Period (fs): 15.4679

Minimum Step Size to fully sample transition (fs): 7.73395

Shift Frequency (cm-1): 1800

Shifted Period (fs): 93.8967

Minimum Step Size to fully sample shifted period (fs): 46.9484

Interval: 24

Fourier Transform Axis Limits

max value: 2493.09

min value: 1800

REFERENCES

1. N. Demirdoven, C. M. Cheatum, H. S. Chung, M. Khalil, J. Knoester and A. Tokmakoff, J. Am. Chem. Soc. **126** (25), 7981-7990 (2004).

2. A. A. Bakulin, C. Liang, T. la Cour Jansen, D. A. Wiersma, H. J. Bakker and M. S. Pshenichnikov, Acc. Chem. Res. **42** (9), 1229-1238 (2009).

3. J. Zheng, K. Kwak, J. Asbury, X. Chen, I. R. Piletic and M. D. Fayer, Science **309** (5739), 1338-1343 (2005).

4. J. Zheng, K. Kwak, X. Chen, J. B. Asbury and M. D. Fayer, J. Am. Chem. Soc. **128** (9), 2977-2987 (2006).

5. K. Kwac, C. Lee, Y. Jung, J. Han, K. Kwak, J. Zheng, M. D. Fayer and M. Cho, J. Chem. Phys **125** (24), 244508-244516 (2006).

6. S. H. Shim, D. B. Strasfeld, Y. L. Ling and M. T. Zanni, Proc. Natl. Acad. Sci. U.S.A. **104** (36), 14197-14202 (2007).

7. P. Hamm and M. T. Zanni, *Concepts and Methods of 2D Infrared Spectroscopy*. (Cambridge University Press, New York, NY, 2011).

8. P. Hamm, M. H. Lim and R. M. Hochstrasser, J. Phys. Chem. B **102** (31), 6123-6138 (1998).

9. M. Khalil, N. Demirdoven and A. Tokmakoff, J. Phys. Chem. A **107** (27), 5258-5279 (2003).

10. J. B. Asbury, T. Steinel, C. Stromberg, K. J. Gaffney, I. R. Piletic, A. Goun and M. D. Fayer, Phys. Rev. Lett. **91** (23) (2003).

11. S.-H. Shim and M. T. Zanni, Phys. Chem. Chem. Phys. **11** (5), 748-761 (2009).

12. A. M. Weiner, D. E. Leaird, J. S. Patel and J. R. Wullert, Opt. Lett. **15** (6), 326-328 (1990).

13. J. A. Myers, K. L. Lewis, P. F. Tekavec and J. P. Ogilvie, Opt. Express **16** (22), 17420-17428 (2008).

14. M. M. Wefers and K. A. Nelson, Opt. Lett. **18** (23), 2032-2034 (1993).

15. J. C. Vaughan, T. Hornung, K. W. Stone and K. A. Nelson, The Journal of Physical Chemistry A **111** (23), 4873-4883 (2007).

16. M. A. Dugan, J. X. Tull and W. S. Warren, J. Opt. Soc. Am. B **14** (9), 2348-2358 (1997).

17. S. H. Shim, D. B. Strasfeld and M. T. Zanni, Optics Express **14** (26), 13120-13130 (2006).

18. D. B. Strasfeld, S. H. Shim and M. T. Zanni, Phys. Rev. Lett. **99** (3) (2007).

19. S.-H. Shim, The University of Wisconsin-Madison, 2008.

20. A. M. Weiner, Review of Scientific Instruments **71** (5), 1929-1960 (2000).

21. C. W. Hillegas, J. X. Tull, D. Goswami, D. Strickland and W. S. Warren, Opt. Lett. **19** (10), 737-739 (1994).

22. C. Froehly, B. Colombeau and M. Vampouille, in *Progress in Optics*, edited by E. Wolf (Elsevier, 1983), Vol. Volume 20, pp. 63-153.

23. W. A.M, Progress in Quantum Electronics **19** (3), 161-237 (1995).

24. W. P. de Boeij, M. S. Pshenichnikov and D. A. Wiersma, Chem. Phys. Lett. **238** (1–3), 1-8 (1995).

25. D. Keusters, H.-S. Tan and Warren, The Journal of Physical Chemistry A **103** (49), 10369-10380 (1999).

26. P. Tian, D. Keusters, Y. Suzaki and W. S. Warren, Science **300** (5625), 1553-1555 (2003).

27. D. B. Strasfeld, Y. L. Ling, S. H. Shim and M. T. Zanni, J. Am. Chem. Soc. **130** (21), 6698-+ (2008).

28. R. Bloem, S. Garrett-Roe, H. Strzalka, P. Hamm and P. Donaldson, Opt. Express **18** (26), 27067-27078 (2010).

29. L. L. Kristin, A. M. Jeffrey, F. Franklin, F. T. Patrick and P. O. Jennifer, 2010 (unpublished).

30. J. N. Moore, P. A. Hansen and R. M. Hochstrasser, Chem. Phys. Lett. **138** (1), 110-114 (1987).

31. E. J. Heilweil, Opt. Lett. **14** (11), 551-553 (1989).

32. T. P. Dougherty and E. J. Heilweil, Opt. Lett. **19** (2), 129-131 (1994).

33. M. F. DeCamp and A. Tokmakoff, Opt. Lett. **30** (14), 1818-1820 (2005).

34. K. J. Kubarych, M. Joffre, A. Moore, N. Belabas and D. M. Jonas, Opt. Lett. **30** (10), 1228-1230 (2005).

35. M. J. Nee, R. McCanne, K. J. Kubarych and M. Joffre, Opt. Lett. **32** (6), 713-715 (2007).

36. E. M. Grumstrup, S. H. Shim, M. A. Montgomery, N. H. Damrauer and M. T. Zanni, Optics Express **15** (25), 16681-16689 (2007).

37. W. Xiong and M. T. Zanni, Optics Letters **33** (12), 1371-1373 (2008).

38. S. H. Shim, R. Gupta, Y. L. Ling, D. B. Strasfeld, D. P. Raleigh and M. T. Zanni, Proc. Natl. Acad. Sci. U.S.A. **106** (16), 6614-6619 (2009).

39. D. B. Strasfeld, Y. L. Ling, R. Gupta, D. P. Raleigh and M. T. Zanni, J. Phys. Chem. B **113** (47), 15679-15691 (2009).

40. A. M. Woys, Y. S. Lin, A. S. Reddy, W. Xiong, J. J. de Pablo, J. L. Skinner and M. T. Zanni, J. Am. Chem. Soc. **132** (8), 2832-2838 (2010).

41. V. Volkov, R. Schanz and P. Hamm, Opt. Lett. **30** (15), 2010-2012 (2005).

42. J. Helbing and P. Hamm, J. Opt. Soc. Am. B **28** (1), 171-178 (2011).

43. S. T. Roberts, J. J. Loparo, K. Ramasesha and A. Tokmakoff, Optics Communications **284** (4), 1062-1066 (2011).

44. K. Ando and J. T. Hynes, in *Adv. Chem. Phys.* (John Wiley & Sons, Inc., 2007), pp. 381-430.

45. S. Takeuchi and T. Tahara, The Journal of Physical Chemistry A **102** (40), 7740-7753 (1998).

46. M. Rini, B.-Z. Magnes, E. Pines and E. T. J. Nibbering, Science **301** (5631), 349-352 (2003).

47. S. Ameer-Beg, S. M. Ormson, R. G. Brown, P. Matousek, M. Towrie, E. T. J. Nibbering, P. Foggi and F. V. R. Neuwahl, The Journal of Physical Chemistry A **105** (15), 3709-3718 (2001).

48. H. Ishikawa, K. Kwak, J. K. Chung, S. Kim and M. D. Fayer, Proc. Natl. Acad. Sci. U.S.A. **105** (25), 8619-8624 (2008).

49. Y. S. Kim and R. M. Hochstrasser, Proc. Natl. Acad. Sci. U.S.A. **102** (32), 11185-11190 (2005).

50. M. W. Nydegger, S. Dutta and C. M. Cheatum, J. Chem. Phys. **133** (13) (2010).

51. J. S. Lipkin, R. Song, E. E. Fenlon and S. H. Brewer, The Journal of Physical Chemistry Letters **2** (14), 1672-1676 (2011).

52. D. Borgis and J. T. Hynes, Chem. Phys. **170** (3), 315-346 (1993).

53. H. Azzouz and D. Borgis, Journal of Molecular Liquids **61** (1-3), 17-36 (1994).

54. S. Hammes-Schiffer and J. C. Tully, J. Chem. Phys **101** (6), 4657-4667 (1994).

55. D. Antoniou and S. D. Schwartz, J. Chem. Phys. **110** (1), 465-472 (1999).

56. R. P. McRae, G. K. Schenter, B. C. Garrett, Z. Svetlicic and D. G. Truhlar, J. Chem. Phys. **115** (18), 8460-8480 (2001).

57. T. Yamamoto and W. H. Miller, J. Chem. Phys. **122** (4), 044106 (2005).

58. S. Y. Kim and S. Hammes-Schiffer, J. Chem. Phys **119** (8), 4389-4398 (2003).

59. P. Hamm, M. Lim and R. M. Hochstrasser, Phys. Rev. Lett. **81** (24), 5326-5329 (1998).

60. K. Ohta, H. Maekawa, S. Saito and K. Tominaga, J. Phys. Chem. A **107** (30), 5643-5649 (2003).

61. K. Ohta and K. Tominaga, Bulletin of the Chemical Society of Japan **78** (9), 1581-1594 (2005).

62. M. J. Lang, X. J. Jordanides, X. Song and G. R. Fleming, J. Chem. Phys. **110** (12), 5884-5892 (1999).

63. J. N. Bandaria, S. Dutta, S. E. Hill, A. Kohen and C. M. Cheatum, J. Am. Chem. Soc. **130** (1), 22-+ (2008).

64. J. B. Asbury, T. Steinel, K. Kwak, S. A. Corcelli, C. P. Lawrence, J. L. Skinner and M. D. Fayer, J. Chem. Phys. **121** (24), 12431-12446 (2004).

65. S. T. Roberts, J. J. Loparo and A. Tokmakoff, J. Chem. Phys **125** (8), 084502-084508 (2006).

66. J. N. Bandaria, S. Dutta, M. W. Nydegger, W. Rock, A. Kohen and C. M. Cheatum, Proc. Natl. Acad. Sci. U.S.A. **107** (42), 17974-17979 (2010).

67. S. Roy, M. S. Pshenichnikov and T. L. C. Jansen, J. Phys. Chem. B **115** (18), 5431-5440 (2011).

68. K. Kwak, S. Park, I. J. Finkelstein and M. D. Fayer, J. Chem. Phys. **127** (12), 124503 (2007).

69. K. Kwak, D. E. Rosenfeld and M. D. Fayer, J. Chem. Phys. **128** (20), 204505 (2008).

70. K. Kwac, H. Lee and M. H. Cho, J. Chem. Phys. **120** (3), 1477-1490 (2004).

71. J. R. Zheng, K. Kwak, J. Asbury, X. Chen, I. R. Piletic and M. D. Fayer, Science **309** (5739), 1338-1343 (2005).

72. E. Harder, J. D. Eaves, A. Tokmakoff and B. J. Berne, Proc. Natl. Acad. Sci. U.S.A. **102** (33), 11611-11616 (2005).

73. S. Garrett-Roe and P. Hamm, J. Chem. Phys **128** (10), 104507-104513 (2008).

74. S. Garrett-Roe, F. Perakis, F. Rao and P. Hamm, J. Phys. Chem. B **115** (21), 6976-6984 (2011).

75. M. Li, J. Owrutsky, M. Sarisky, J. P. Culver, A. Yodh and R. M. Hochstrasser, J. Chem. Phys **98** (7), 5499-5507 (1993).

76. J. C. Owrutsky, D. Raftery and R. M. Hochstrasser, Ann. Rev. Phys. Chem. **45** (1), 519-555 (1994).

77. P. W. Schultz, G. E. Leroi and A. I. Popov, J. Am. Chem. Soc. **117** (43), 10735-10742 (1995).